TECHNISCHE UNIVERSITÄT MÜNCHEN, PHYSIK DEPARTMENT

MAX-PLANCK-INSTITUT FÜR ASTROPHYSIK

Finding Lensed Quasars with Time Variability in Imaging Surveys

Chun-Yi Chao

Vollständiger Abdruck der von der Fakultät für Physik der Technischen Universität München zur Erlangung des akademischen Grades eines

Doktor der Naturwissenschaften (Dr. rer. nat.)

genehmigten Dissertation.

Vorsitzender:
Prof. Dr. Alejandro Ibarra

Prüfende der Dissertation:
1. Prof. Dr. Sherry Suyu
2. Hon.-Prof. Eiichiro Komatsu, Ph.D.

Die Dissertation wurde am 13.07.2020 bei der Technischen Universität München eingereicht und durch die Fakultät für Physik am 29.07.2020 angenommen.

Chun-Yi Chao
ORCID: 0000-0001-9028-1173

ACKNOWLEDGEMENTS

I am grateful to my supervisor, Sherry Suyu. Thank you for your patience. It is hard to express my gratitude to you in words, as I have gained so much from you. I really appreciate your insightful guidance. I would also like to thank James Chan for the constant help on my PhD project, especially the support during quarantine. Thanks my HSC collaborators, Anupreeta More, Tomoki Morokuma, Masamune Oguri, Edi Rusu, Nao Suzuki, Masaomi Tanaka, and Naoki Yasuda, for all the constructive comments. Thanks Adriano Agnello for the useful suggestions on my PhD project.

I am thankful to my group members, Raoul Canameras, Giulia Chirivì, Sebastian Ertl, Simon Huber, Stefan Schuldt, Stefan Taubenberger, Han Wang, and Akin Yildirim, for the inspiration they share in the weekly group meeting. Thanks Stefan Schuldt, Stefan Taubenberger, and Simon Huber for German abstract of this thesis!

I appreciate the discussion with Stefan Hilbert and Eiichiro Komatsu in the thesis committee meetings. I would like to thank the secretaries at MPA, Maria Depner, Sonja Gründl, Gabriele Kratschmann, and Cornelia Rickl, for making my life as a foreigner in Germany much easier.

Thanks my best friend, Solomon Lin, for all the crimes we have done. Thanks Jacke Molis and Laure d′Utruy for picking me up on the street in Kreuzberg and taking me to the parties in Paul's apartment around Görlitzer Park and secret places in Neukölln, which has become the most precious adventure in my life!

Thanks Ricard Ardevol-Pulpillo, Marc Bernreuther, Vivien Bonvin, Aoife Boyle, Philipp Busch, Tzu-Yu Chou, Simona Ciceri, Marius Eide, Matteo Frigo, Michael Gabler, Martin Glatzle, Haruomi Hosono, Inh Jee, Amy Jones, Eun-Bi Jung, So-Jung Kim, Tyler Mueller, Malin Renneby, Ryuichi Sakamoto, Yukihiro Takahashi, Tom Tang, Wan-Yi Tang, Eugene Tong, Yen-Jhen Tseng, Simona Vegetti, Dijana Vrbanec, and David Yu for being my role models, running mentors, friends, someone unknowingly gave me memorable moments, or just being a little bulb when I come through a long way in my dark cave.

Special thanks to Sherry Wu. If I did not meet you in my fifteen, I would not have completed anything in my life. You always reside in my retina.

Last but not least, thank you to my mother and grandmother for the unconditional love and support. Thanks people around me for bearing my never-transited adolescence.

ZUSAMMENFASSUNG

Der starke Gravitationslinseneffekt ist ein mächtiges Instrument, um das Universum zu studieren. Im Vordergrund liegende, massereiche Objekte, wie zum Beispiel Galaxien, wirken dabei als starke Gravitationslinsen auf Quellen im Hintergrund, welche dadurch mehrfach am Himmel abgebildet werden. Falls die Hintergrundquelle ein Quasar ist, kann das Linsensystem verwendet werden, um die Physik von Schwarzen Löchern zu studieren, die Theorie der Galaxienentstehung zu überprüfen, dunkle Materie und deren Substruktur zu untersuchen und die Hubble-Konstante zu messen. Daher ist es für diese Anwendungen wichtig, einen statistisch signifikanten Satz von Gravitationslinsen-Quasaren zu erstellen. Aufgrund der Tatsache, dass Gravitationslinsen-Quasare sehr selten sind, sind astrophysikalische und kosmologische Studien mit Gravitationslinsen-Quasaren bis heute durch einen kleinen Datensatz limitiert. Es gab mehrere dedizierte Suchprogramme nach Gravitationslinsen-Quasaren, und bisher sind ∼200 solcher Systeme bekannt. Während die meisten dieser Suchprogramme statisch spektroskopische oder photometrische Informationen nutzen, präsentieren wir eine alternative Methode, welche auf der zeitlichen Variabilität basiert, um Gravitationslinsen-Quasare zu finden. Praktisch handelt es sich dabei um einen Suchalgorithmus, der Gravitationslinsen-Quasare durch die Differenzbildung zweier zeitlich getrennter Aufnahmen erkennt. Zu diesem Zweck entwickeln wir zunächst eine Software, die zeitabhängige Linsenbilder simuliert, und dabei die Variabilität des Quasars, seiner Umgebung, die Linsengalaxie im Vordergrund und die Variabilität der Punktspreizfunktion berücksichtigt. Wir erzeugen aus diesen Daten dann Differenzbilder der simulierten Gravitationslinsen-Quasare, wobei wir das Hyper Suprime-Cam (HSC) Beobachtungsprogramm veränderlicher Objekte nachbilden. Wir entwickeln schließlich einen Algorithmus, der veränderliche Objekte auf Basis ihrer räumlichen Ausdehnung in den Differenzbildern als Kandidaten für Gravitationslinsen-Quasare selektiert. Zum Test wenden wir unseren Suchalgorithmus auf einen kombinierten Datensatz aus simulierten Gravitationslinsen-Quasaren und anderen veränderlichen Objekten aus dem HSC-Beobachtungsprogramm an, wobei eine hohe Richtig-Positiv-Rate von 90,1% und eine niedrige Falsch-Positiv-Rate von 2,3% erzielt wird. Wir führen schließlich eine Linsensuche auf Daten des HSC Beobachtungsprogramms veränderlicher Objekte durch, bei der unser Suchalgorithmus den einzig bisher bekannten, vierfach abgebildeten Quasar (Quad) innerhalb des Feldes korrekt

identifiziert. Zusätzlich zu diesem bekannten Gravitationslinsen-Quasar findet der Algorithmus sieben weitere neue Kandidaten. Die in dieser Arbeit durchgeführte Machbarkeitsstudie lässt erwarten, dass die Anwendung, des auf zeitlicher Veränderung basierenden Linsensuchalgorithmus, auf andere Beobachtungsprogramme zur Entdeckung Tausender neuer Gravitationslinsen-Quasare führen könnte.

ABSTRACT

Strong gravitational lensing is a powerful tool to study the Universe. The foreground massive objects, such as galaxies, act as strong gravitational lenses on the background sources, and the background sources are further multiply imaged on the sky. When the background source is a quasar, the lens system can be used to study black hole physics, to examine galaxy evolution theories, to probe dark matter and its substructure, and to measure the Hubble constant. Therefore, constructing a statistical sample of lensed quasars is important for its applications. Given the fact that lensed quasars are rare, further astrophysical or cosmological studies with lensed quasars are still limited by the small sample size of lensed quasars in the present stage. There have been several searches dedicated to find lensed quasars, and currently, ∼200 lensed quasars have been found. While most of lensed quasar searches use static spectroscopic or photometric information, we present an alternative lensed quasar search method that exploits their time variability. Practically, we develop a lens search algorithm detecting lensed quasars with difference imaging. We first build a simulation pipeline generating time-varied lensed images that takes into account the quasar variability, quasar host, foreground lens galaxy, and the point-spread-function variation. We generate difference images of the mock lensed quasars for the Hyper Suprime-Cam (HSC) transient survey, and further develop a lens search algorithm that selects variable objects as lensed quasar candidates based on their spatial extent in the difference images. The test on a sample combining the mock lensed quasars and variable objects from the HSC transient survey shows that our time-variability-based lens search algorithm achieves a high true-positive rate of 90.1% and a low false-positive rate of 2.3%. We conduct a lens search within the HSC transient survey applying the time-variability-based lens search algorithm, and recover the only known four-image (quad) lensed quasar in the survey field. In addition to the known quad, we discover seven new lensed candidates with the time-variability-based lens search algorithm. Based on the feasibility shown in this thesis, it is expected that the adoption of the time-variability-based lens search algorithm to other cadenced imaging surveys can capture thousands of new lensed quasars.

TABLE OF CONTENTS

LIST OF ILLUSTRATIONS

LIST OF TABLES

Chapter 1

INTRODUCTION

As the introductory chapter in this thesis, we begin with a simple summary of lensed quasar history in Section 1.1 and discuss some of their well-known applications in Section 1.2. The outline of this thesis is in Section 1.3.

1.1 Brief history of lensed quasar

When a massive object, such as galaxy or galaxy cluster, is in front of a source object along the line of sight, the light rays from the source object are deflected by the gravitation field of the foreground massive object, and the source object is multiply lensed on the sky. This lensing effect is strong gravitational lensing, which can be well described by General Relativity. Since the light rays travel different paths for each multiply lensed image from the source object to the observer, there are time delays among the multiply lensed images. These gravitational time delays can be measurable when the source object has variable brightness, and as first proposed by Refsdal (1964), they can further be used for the measurement of the Hubble constant H_0, a crucial cosmological parameter related to the expansion rate of the Universe. While Refsdal (1964) considered the brightness-variable sources as supernovae, the first discovery of quasars by Schmidt (1963) provided another possibility of using quasars as the brightness-variable sources, which are usually more distant than supernovae. However, it was not until 1979 that the first lensed quasar, QSO0957+561, was found by Walsh et al. (1979). QSO0957+561 is a two-image (double) lensed quasar as shown in figure 1.1, and was discovered as a pair of quasars with identical spectra at redshift $z = 1.41$. The foreground lensing galaxy of QSO0957+561 was detected soon after at redshift $z = 0.36$, which confirmed that QSO0957+561 is a lensed quasar (Stockton, 1980; Young et al., 1980).

After QSO0957+561, there had been a few more discoveries of lensed quasars by the mid-1990s. Some are found through systematic searches among the brightest quasars in the optical, since the large brightness is probably resulted from the lensing magnification (Sanitt, 1971), such as PG1115+080 (figure 1.2) - the first discovered four-image (quad) lensed quasar (Weymann et al., 1980), UM673 (Surdej et al., 1987), and H1413+117 (Magain et al., 1988). Some other new lensed quasars

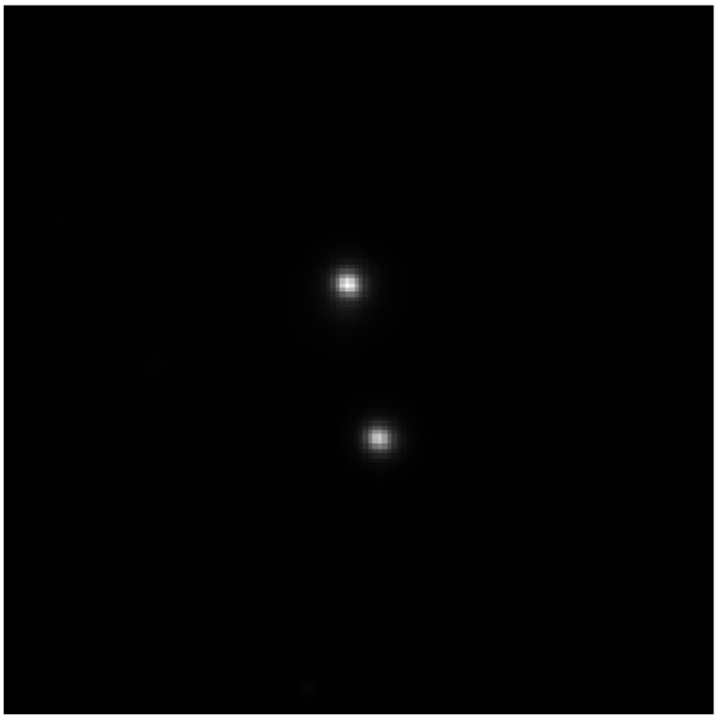

Figure 1.1: The Canada–France–Hawaii Telescope (CFHT) *R*-band image of the first discovered lensed quasar, QSO0957+561. QSO0957+561 is a two-image (double) lensed quasar. Image source: Canadian Astronomy Data Centre.

are discovered through radio searches, such as MG1654+1346 (Langston et al., 1989), PKS1830−211 (Subrahmanyan et al., 1990), and MG0414+0534 (Hewitt et al., 1992). One main challenge of further using lensed quasar for astrophysical and cosmological studies in this time period was obtaining mass distribution for the foreground lensing galaxies/clusters, since the telescope sensitivities and resolutions were not good enough to provide detailed characterization for observed systems, such as the well resolved positions of multiply lensed images, for constraining the mass distribution of the lensing galaxies. Another main challenge was reliably measuring the time delays from lensed quasars, as the angular separations among the multiply lensed images are small, generally one to two arcsec, and quasar brightness variations are usually not so sharp that it is not easy for one to correctly identify the similar patterns of the light curves from the multiply lensed images. For example, different campaigns in the optical and radio wavelengths measuring the time delay from QSO0957+561 yielded significantly different results, as they took into account the impacts on the observed light curves from the effects such as seasonal gaps or

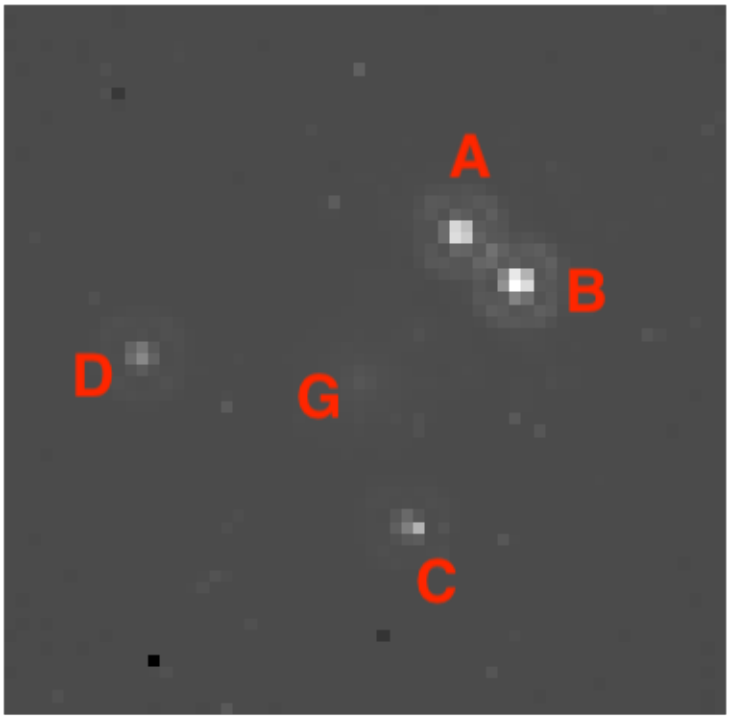

Figure 1.2: The HST image of the first discovered four-image (quad) lensed quasar, PG1115+080. The four lensed images are labeled as A, B, C, and D, and the lensing galaxy is labeled as G. Data source: HST image archive.

microlensing using different methods. For QSO0957+561, Vanderriest et al. (1989) and Schild (1990) derived a time delay of ~415 days from ground-based optical observations, while Roberts et al. (1991) derived a time delay of ~536 days with the radio monitoring results obtained by the Very Large Array (VLA). Fortunately, with the improved optical and radio monitoring observations, the discrepancy of time delays from different measurements has been reconciled (Haarsma et al., 1999; Kundić et al., 1997; Oscoz et al., 1997), making it a step forward to determining the value of H_0.

As the observation technology progresses, it shed some light on conquering the observational limitations of using lensed quasars for further studies. The space observatory, Hubble Space Telescope (HST), provided excellent resolution that one could infer the positions of the foreground lens and the lensed images blow an accuracy of a few tens of milli-arcsec, reaching the requirements for detailed lens modelling (e.g., Lehár et al., 2000). The subpixel-scale HST data is also important

to point spread function characterization. Furthermore, the high angular resolution provided by the HST also made it possible to observe the host galaxies of lensed quasars. The host galaxies of lensed quasars as extended sources provide extra constraints on the mass distribution and could also be used to study the quasar-host galaxy relations, which is important for galaxy evolution (e.g., Keeton et al., 2000). Meanwhile, the ground-based surveys had also been leveraged. The enhancement in imaging processing allowed one to obtain accurate photometric monitoring for the time delays from ground-based telescopes (e.g., Magain et al., 1998; Burud et al., 2002a; Burud et al., 2002b; Hjorth et al., 2002). The deconvolution techniques in ground-based spectroscopy helped one to measure the redshifts of the foreground lenses, which are required for determining the geometry of the lens systems (e.g., lens size) and measuring the value of H_0 (e.g., Lidman et al., 2000). The spectroscopy from ground-based surveys measured the velocity dispersion of the foreground lens and identify objects around the lens environment or along the line of sight, which are important for the accuracy of the foreground lens mass distribution (e.g., Koopmans et al., 2003; Fassnacht et al., 2006a; Fassnacht et al., 2006b). The increasing availability of the multi-band data have also enabled one to correct the dust extinction and probe the properties of lens systems with different spectral energy distributions (e.g., Lidman et al., 1999; Dai and Kochanek, 2005).

The progression with observation encourages the developments in data analysis and theories for various topics related to lensed quasar, such as detailed mass modeling techniques for the foreground lens, source reconstruction (e.g., Dye and Warren, 2005; Brewer and Lewis, 2006; Suyu et al., 2006), temporal sampling techniques for the lensed quasar light curves (e.g., Eigenbrod et al., 2005), and statistical inference for H_0 measurement (e.g., Suyu et al., 2010). Although the observational and the analysis of lensed quasars have been matured through projects like COSMOGRAIL[1] and H0LiCOW[2], each lensed quasar still has its own uniqueness in the dominated uncertainties. For example, in HE2149−2745 it is the uncertainty from the time delay measurement that dominates (Burud et al., 2002a), while in B1608+656 it is the uncertainty from the mass structure along the line of sight that dominates (Suyu et al., 2009). These uncertainties limit the determination of H_0 using the time delay measurement, and one solution to reduce these systematic errors is to observe as

[1] the COSmological MOnitoring of GRAvItational Lenses, https://www.epfl.ch/labs/lastro/scientific-activities/cosmograil/

[2] H_0 Lenses in COSMOGRAIL's Wellspring, https://shsuyu.github.io/H0LiCOW/site/

many lensed quasars as possible and to obtain H_0 statistically (Oguri, 2007). There have been several systematic lensed quasar searches, such as the Cosmic Lens All Sky Survey (CLASS; Myers et al., 2003; Browne et al., 2003) in radio wavelengths and the SDSS[3] Quasar Lens Search (SQLS; Oguri et al., 2006; Inada et al., 2008; Inada et al., 2010; Inada et al., 2012; More et al., 2016b) in the optical.

Comparing to the time around the first discovery in 1979, the field of lensed quasar has grown to a more productive stage. The number of lensed quasars is largely growing, and the discoveries of lensed quasars have been more systematic and expectable. For example, CLASS has discovered ∼20 new lensed quasars, and SQLS has found ∼60 new lensed quasars. The observational and theoretical advances have broadened the use of lensed quasar. While lensed quasar has now become prominent among the measurements of H_0, it also becomes more and more important in other studies, such as dark matter substructure and galaxy evolution. In Section 1.2, we will introduce the application of lensed quasar briefly.

1.2 Lensed quasar application

Here, we give a brief description for some lensed quasar applications in astrophysics and cosmology.

- H_0 *measurement*. Lensed quasars enable a range of astrophysical and cosmological studies, and one prominent usage is to measure the value of H_0. Most of the other H_0 measurements depend on distance ladders that usually lead to systematic effects. For example, the measured distances from Type Ia Supernovae are usually calibrated by Cepheids with Cepheids' Period-Luminosity relation (P-L relation), but P-L relation actually have dependence on the metallicities of the environment they reside (e.g. Tammann et al., 2003; Sandage et al., 2004; Sakai et al., 2004). Some other H_0 measurements like Cosmic Microwave Background (CMB) need the assumptions on cosmology, such as the Universe being flat and dark energy being described by a cosmological constant w(=1) (Bennett et al., 2013; Planck Collaboration et al., 2018), and H_0 would easily change and become less accurate if one relaxes such cosmological assumptions. On the other hand, in principal by measuring the time delays and modelling the mass distribution for the foreground lenses, one

[3]SDSS, Sloan Digital Sky Survey (York et al., 2000)

could use lensed quasars to measure the distances in one step without using any distance ladder. Moreover, by overcoming the difficulties in obtaining reliable time delays through routine monitoring projects (e.g., COSMOGRAIL), exploiting the extra constraints from the lensed quasar host galaxies, taking account the line-of-sight objects by simulations, and employing sophisticated cosmological inference, recent H_0 measurements using lensed quasars could reach a few percent precision (e.g., Suyu et al., 2013; Bonvin et al., 2017; Chen et al., 2019; Wong et al., 2019; Shajib et al., 2020).

- *Magnification on sources*. Since lensing could magnify the brightness of the background sources, the faint quasars in the high-redshift universe originally unable to be detected would possibly exceed the detection threshold after being lensed. This lensing magnification is helpful in finding high-redshift quasars, which are important for topics like reionization and supermassive black holes (e.g., Fan et al., 2019). Furthermore, the magnified version of quasar also allows one to study the black hole physics and quasar structure in detail, such as the spin of the supermassive black hole (e.g., Sluse et al., 2003) and the jets in quasar (e.g., Hartley et al., 2019). As the quasar host galaxies are magnified as well, one could also get benefits from this lensing magnification for studying the properties of quasar host galaxies and the quasar-host galaxy relation, which are important for galaxy evolution (e.g., Peng et al., 2006a; Ding et al., 2017; Stacey et al., 2018).

- *Quasar microlensing*. As stars comprise part of the mass in the foreground galaxy, stars in the foreground galaxy also affect the light rays when light rays from the source quasar pass close to the foreground galaxy. Since the mass distribution of stars in the foreground galaxy is not uniform, but more like graininess, the light rays from the quasar are microlensed differently by the stars in the foreground galaxy. This phenomenon is termed *micorlensing*. Although the fluctuation on the strongly lensed images caused by microlensing effect might be small and sometimes only observable on the total brightness change regarding the lensed image separation (e.g., Irwin et al., 1989), this small fluctuation can last weeks to years in the optical, depending on the relative motions of the quasar, foreground galaxy, and observer, and further pollute the measurements of time delay and flux ratio (e.g., Morgan et al.,

2006; Dobler et al., 2007; Tie and Kochanek, 2018a). On the other hand, as the star fields inducing microlensing effect are small and comparable to the size of quasar accretion disk, microlensing effect provides approaches to study quasar inner structure. Since different regions of quasar have different colors, the microlensing signal is chromatic, as a region of quasar is microlensed and another region is not. Therefore, when a quasar accretion disk is microlensed, one can probe the size of the accretion disk (e.g., Wambsganss et al., 1990; Yonehara et al., 1998; Mineshige and Yonehara, 1999; Blackburne et al., 2011; Tie and Kochanek, 2018b), the inclination angle of the accretion disk (e.g., Morgan et al., 2018), or the black hole mass (e.g., Kochanek, 2004), through multi-wavelength observations of lensed quasars.

Additionally, though not specific to lensed quasar, one can use microlensing to measure the stellar mass distribution, as microlensing effect is sensitive to the local stellar mass surface density (e.g., Wyithe et al., 2000; Bate et al., 2011). We note that there will be no microlensing event if there is no star, but a very large stellar mass fraction will also make the microlensing event less obvious due to the smoother mass distribution (e.g., Jiménez-Vicente et al., 2015). For the detail about microlensing, we refer the reader to Courbin et al. (2002) and *Gravitational Lensing: Strong, Weak and Micro* (2006).

- *Dark matter substructure*. Not specific to lensed quasar, the mass inferred from strong lensing is the total mass in the foreground galaxy, including those can not be seen directly by observations such as dark matter. As the lens mass modeling put constraints on the mass profiles of the foreground galaxy, one could use lensed quasars to study dark matter distribution in the foreground lensing galaxies. While the lensed image positions are well explained by isothermal profiles for the foreground lensing galaxies, the flux ratios of the lensed images can be different from the lens model predictions. These flux ratio anomalies usually imply microlensing events or mass substructure ($\lesssim 10^9$ $M_\odot$). Since microlensing events are unlikely shown in radio wavelengths, the flux ratio anomalies in the radio-loud lensed quasars can be used to probe the dark matter substructure, which is important for testing different cosmological scenarios (e.g., Mao and Schneider, 1998; Metcalf and Madau, 2001; Dalal and Kochanek, 2002; Nierenberg et al., 2014; Gilman et al., 2019).

We note that the examples mentioned in this section do not include *all* the applications of lensed quasar. They are just some well-known usages of lensed quasar. Lensed quasar has unique advantages for many astrophysical and cosmological studies. As lensed quasars are rare objects in nature, the power of using lensed quasars for the above studies is limited by its sample size. Therefore, enlarging the sample size of lensed quasars is important for their applications. Due to the uniqueness and rareness of lensed quasars, developing methods looking for them also become an active field in astrophysics, especially in the time that many large surveys are coming.

1.3 Outline of thesis

We present a lensed quasar search method based on the (time) variability and show the feasibility of this method in this thesis. We exploit difference imaging, which could reveal the brightness change of lensed quasar, to look for lensed quasars.

In chapter 2, we first introduce some basics from lensing theory that characterizes lensed quasar and then give a brief review of lensed quasar searches. This thesis heavily depends on the Hyper Suprime-Cam Subaru Strategic Program (HSC-SSP) survey, especially the HSC transient survey, so we briefly describe the HSC-SSP survey and the HSC transient survey in chapter 3. Chapter 4 consists of two parts: (1) Building a simulation pipeline to generate time-varied images of lensed quasar, (2) Developing a lensed quasar search algorithm based on quasar variability with those simulated images from (1) and testing the searching algorithm on the simulated images. In chapter 5, we apply the lens search method developed in chapter 4 to the real data from the HSC transient survey and present the lens search result within the HSC transient survey. In chapter 6, we discuss the future aspect of a lensed quasar search using neural network trained by the time-varied images from the simulation pipeline developed in this thesis.

Chapter 2

GRAVITATIONAL LENSING: FUNDAMENTALS AND TECHNIQUES

The goal of this thesis is to develop a new lensed quasar search method using time variability, so it is important to understand the theory behind gravitational lensing and to review the techniques exploited in lensed quasar searches. Here, we give a short summary of basic lensing formalism describing lensed quasars in section 2.1 and a brief discussion of some common lensed quasar search techniques in Section 2.2.

2.1 Lensing basics

Here, we outline the lensing basics from the theory characterising lensed quasars. We follow *Gravitational Lensing: Strong, Weak and Micro* (2006) for the gravitational lensing theory.

We show a simple scenario of gravitational lensing in figure 2.1, where $D_{\rm s}$, $D_{\rm d}$, and $D_{\rm ds}$ are the angular diameter distances from the observer to the source, from the observer to the deflector, and from the deflector to the source, respectively. We note that $D_{\rm ds}$ is not necessarily equal to the sum of $D_{\rm s}$ and $D_{\rm d}$, and they are dependent on the cosmology. Three possible paths for the light rays to travel from the source to us are labeled as 1, 2, and 3, where path 2 is the case for no deflection. The image/lens plane and source plane are defined as planes perpendicular to the optical axis, where optical axis is defined as a straight line connecting the observer and some reference in the deflector (e.g., center of mass of the deflector). Any object with gravitational field could work as deflector, such as stars, galaxies, and galaxy clusters. In this thesis, we focus only on galaxies working as deflectors, and also terming "deflector" as foreground lens. We denote the angular coordinates $\vec{\beta} = (\beta_1, \beta_2)$ on the source plane and $\vec{\theta} = (\theta_1, \theta_2)$ on the image plane. The two-dimensional positions relative to the optical axis on the source plane and image/lens plane could be related by $\vec{\eta} = (\eta_1, \eta_2) = D_{\rm s}\vec{\beta}$ and $\vec{\xi} = (\xi_1, \xi_2) = D_{\rm d}\vec{\theta}$, respectively.

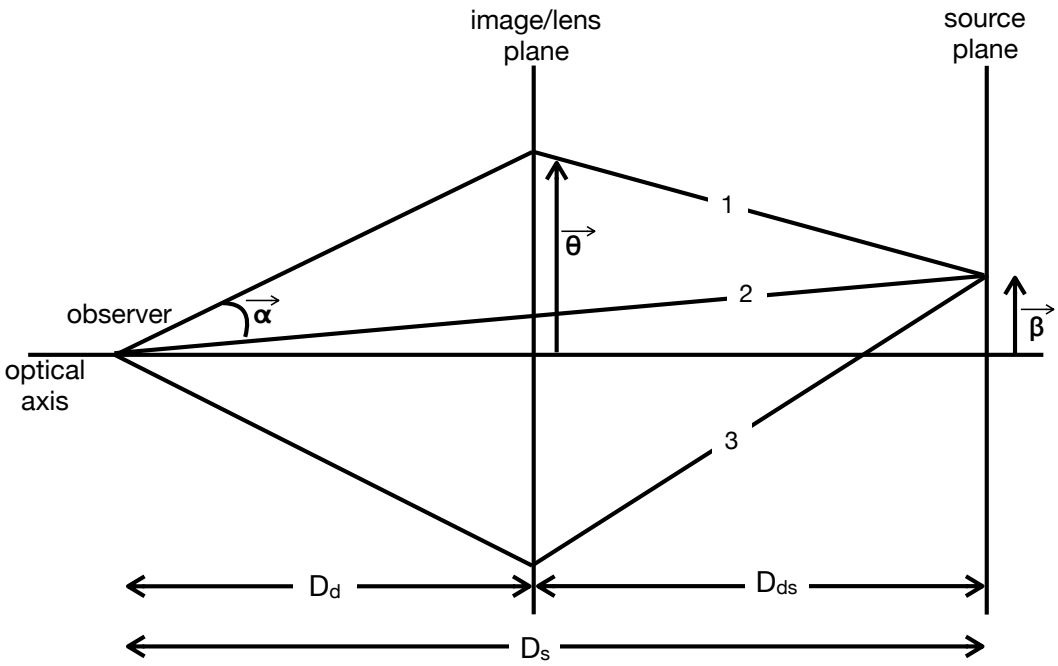

Figure 2.1: Illustration of a lensing scenario. 1, 2, and 3 are three possible paths for the light rays to travel from the source to us, where path 2 corresponds to no deflection. $D_{\rm s}$, $D_{\rm d}$, and $D_{\rm ds}$ are the angular diameter distances. $\vec{\theta}$ and $\vec{\beta}$ are the angular coordinate on the image plane and source plane, respectively. $\vec{\alpha}$ is the deflection angle.

The deflection is ruled by the lens equation,

$$\vec{\beta} = \vec{\theta} - \vec{\alpha}(\vec{\theta}), \tag{2.1}$$

where $\vec{\alpha}(\theta)$ is defined as the scaled deflection angle. The scenario of gravitational lensing is that the observer views the source at the angle $\vec{\theta}$ on the image/lens plane, which is actually at the angle $\vec{\beta}$ on the source plane, due to the deflection of light with the angle $\vec{\alpha}$ caused by the foreground lens. Equation (2.1) implicitly describes how the (angular) source position, $\vec{\beta}$, is connected to the (angular) image position, $\vec{\theta}$. The cosmology and the mass distribution of the foreground lens are encoded in $\vec{\alpha}$.

When the mass distribution of the foreground lens is simple, the deflection angle $\vec{\alpha}$ can be calculated analytically. For example, the deflection angle for the lens with a point mass M is

$$\vec{\alpha} = \frac{4GMD_{\rm ds}}{c^2 D_{\rm d} D_{\rm s}} \frac{\vec{\theta}}{|\vec{\theta}|^2}, \tag{2.2}$$

where G is the gravitational constant and c is the speed of light. If the source, the point-mass lens, and observer perfectly lie along the same optical axis, the observer

will view the lensed image as a ring with an angular radius $\theta_{\rm Ein} = (\frac{4GM}{c^2}\frac{D_{\rm ds}}{D_{\rm d}D_{\rm s}})^{1/2}$. This ring is called *Einstein ring*, and $\theta_{\rm Ein}$ is the *Einstein radius*.

Since the field equations of General Relativity can be linearised within weak-gravitation regime, the deflection angle caused by an ensemble of point-mass lens is the sum of the deflection angles resulted from the individual point-mass lenses. Under the assumption of geometrically thin lens[1], one can express $\vec{\alpha}(\vec{\theta})$ as

$$\vec{\alpha}(\vec{\theta}) = \frac{1}{\pi}\int_{\Re^2} d^2\theta' \frac{\Sigma(D_{\rm d}\vec{\theta}')}{\Sigma_{\rm cr}} \frac{\vec{\theta}-\vec{\theta}'}{|\vec{\theta}-\vec{\theta}'|^2}, \tag{2.3}$$

where $\Sigma(D_{\rm d}\vec{\theta}')$ is the projected mass density onto the image/lens plane (surface mass density) at $D_{\rm d}\vec{\theta}'$, and $\Sigma_{\rm cr}$ is the critical surface mass density,

$$\Sigma_{\rm cr} = \frac{c^2 D_{\rm s}}{4\pi G D_{\rm d} D_{\rm ds}}, \tag{2.4}$$

We can rewrite equation 2.3 as

$$\vec{\alpha}(\vec{\theta}) = \frac{1}{\pi}\int_{\Re^2} d^2\theta' \kappa(\vec{\theta}') \frac{\vec{\theta}-\vec{\theta}'}{|\vec{\theta}-\vec{\theta}'|^2} \quad \text{with} \quad \kappa(\vec{\theta}') = \frac{\Sigma(D_{\rm d}\vec{\theta}')}{\Sigma_{\rm cr}}, \tag{2.5}$$

where $\kappa(\vec{\theta}')$ is termed as the dimensionless surface mass density. The sufficient condition for strong lensing or for possible multiple lensed images to occur is $\Sigma(\vec{\xi}) > \Sigma_{\rm cr}$ at position $\vec{\xi}$ in the image/lens plane.

Now we come back to the lens equation (2.1). First, the scaled deflection angle $\vec{\alpha}(\theta)$ is the gradient of a scalar field $\psi(\vec{\theta})$,

$$\vec{\alpha}(\theta) = \vec{\nabla}\psi(\vec{\theta}), \tag{2.6}$$

and in terms of the dimensionless surface density, $\kappa(\vec{\theta}')$, this scalar field is

$$\psi(\vec{\theta}) = \frac{1}{\pi}\int_{\Re^2} d^2\theta' \kappa(\vec{\theta}') \ln|\vec{\theta}-\vec{\theta}'|. \tag{2.7}$$

$\psi(\vec{\theta})$ is called the lens potential. We note that $\nabla^2\psi(\vec{\theta}) = 2k$ is the two-dimension Poisson equation, which is similar to the three-dimension one relating gravitational field ($\phi_{\rm N}$) with mass density (ρ). If we define a scalar function

$$\tau(\vec{\theta},\vec{\beta}) = \frac{1}{2}(\vec{\theta}-\vec{\beta})^2 - \psi(\vec{\theta}), \tag{2.8}$$

[1]The foreground lens is much thinner than the source-lens-observer distance, and the deflection angle actually is small.

$\vec{\nabla}_{\vec{\theta}}\tau(\vec{\theta},\vec{\beta}) = 0$ would be equivalent to the lens equation (2.1). Schneider (1985) has shown that with a proper affine transformation, the function $\tau(\vec{\theta},\vec{\beta})$ is the time for a light ray to travel from a given position $\vec{\beta}$ in the source plane, traversing the lens plane at position $\vec{\theta}$, to the observer. Therefore, the equivalence between equation (2.1) and equation (2.8) actually comes from Fermat's principle, which states that the light traveling time is stationary with respect to the variations of light traveling path. $\tau(\vec{\theta},\vec{\beta})$ is thus called the Fermat potential or time delay function. In terms of $\tau(\vec{\theta},\vec{\beta})$, the lens equation (2.1) interprets that the lensed images positions $\vec{\theta}$ in the image plane are where the time delay surface has extrema, which is useful in classifying the multiple images and lens configuration.[2] One can further express the time delay among lensed images with the Fermat potential (Schneider, 1985). For example, in figure 2.1, the time delay for the lensed image at path 3 relative to the lensed image at path 1 is

$$\Delta t_{31} = \frac{D_{\rm d} D_{\rm s}}{c D_{\rm ds}}(1+z_{\rm d})\left[\tau(\vec{\theta}^{(3)},\vec{\beta}) - \tau(\vec{\theta}^{(1)},\vec{\beta})\right], \tag{2.9}$$

where $\vec{\theta}^{(3)}$ and $\vec{\theta}^{(1)}$ are their image positions at the lens/image plane, respectively.

By assuming a flat Λ-CDM universe, the angular diameter distance between redshifts z_1 and z_2 is expressed as

$$D(z_1,z_2) = \frac{c}{H_0}\frac{1}{1+z_2}\left[\int_{z_1}^{z_2}\frac{dz'}{\sqrt{\Omega_m(1+z')^3+(1-\Omega_m)}}\right], \tag{2.10}$$

where H_0 is the Hubble constant and Ω_m $(1-\Omega_m)$ is the ratio of the matter (dark energy) density to the present critical density. If we write $D_{\rm d}$, $D_{\rm s}$, and $D_{\rm ds}$ in terms of the redshifts with equation (2.10), the constant coefficient in equation (2.9) would be inversely proportional to the Hubble constant H_0. As shown in equation (2.8), we can obtain the Fermat potential $\tau(\vec{\theta},\vec{\beta})$ if we know the image position $\vec{\theta}$, the source position $\vec{\beta}$, and the lens potential $\psi(\vec{\theta})$. Generally, we can obtain the lens potential $\psi(\vec{\theta})$ by modeling the mass distribution for the foreground lens, and further derive the source position $\vec{\beta}$ by solving the lens equation with the mass model of the foreground lens. Therefore, combing with the model of lens mass distribution, one can infer the value of H_0 through measuring the time delays.

[2] We note that the equivalence between equation (2.1) and euqtion (2.8) is no longer valid if the surface mass density is not smooth. If a extremum of the time delay surface is at a singular point of the surface mass density, the lensed image might occur.(Kochanek et al., 2006b)

A well-known phenomenon in lensing is the image magnification that makes the sources brighter than expected or enables the faint sources below the detection limit to be detectable. It is important that the surface brightness is conserved in gravitational lensing. The lensing magnification is actually the increase in the flux. The magnification of lensed images is described by the Jacobian matrix

$$\mathbf{A}(\vec{\theta}) = \frac{\partial \vec{\beta}}{\partial \vec{\theta}}. \tag{2.11}$$

Using equations (2.1 and 2.5), one can get

$$\mathbf{A}(\vec{\theta}) = \begin{bmatrix} 1 - \psi_{11}(\vec{\theta}) & -\psi_{12}(\vec{\theta}) \\ -\psi_{12}(\vec{\theta}) & 1 - \psi_{22}(\vec{\theta}) \end{bmatrix}, \tag{2.12}$$

where the subscript 1 (2) represents the partial derivative with respect to θ_1 (θ_2). The inverse of this Jacobian matrix is called the magnification matrix, $\mathbf{M}(\vec{\theta}) = \mathbf{A}^{-1}(\vec{\theta})$, and the magnification factor at image position $\vec{\theta}$ is

$$\mu(\vec{\theta}) = \det \mathbf{M}(\vec{\theta}) = \frac{1}{\det \mathbf{A}(\vec{\theta})}. \tag{2.13}$$

If $\det \mathbf{A}(\vec{\theta}) = 0$, the magnification at $\mu(\vec{\theta})$ would diverge. The curves collecting points on the image plane that yield divergent magnification factor ($\det \mathbf{A}(\vec{\theta}) = 0$) are defined as the critical curves. The curves on the source plane mapped from the critical curves by the lens equation (2.1) are the caustic curves. The caustic curves separate regions with different number of lensed images, and the lensed image positions are decided by the position of the source relative to the caustic curves.

The foreground lens with axisymmetric mass distribution always generates two lensed images (and a possible central image that is demagnified) of the source, while the lens with asymmetric elliptical mass distribution (or axisymmetric-mass-distribution lens with external perturbation) generates four lensed images (and also a possible central image that is demagnified) for some source positions. The caustic curves mentioned above separate these two regions, region with two lensed images and region with four lensed images. Actually, Burke (1981) proved that foreground lens with smooth surface mass density always produces an odd number of lensed images. However, one of the lensed images lies right behind the foreground lens as a central image and is strongly demagnified. Therefore, in observation, lens systems have only two or four multiple images. In this thesis, we focus more on the lensed quasars with four multiple images (quad).

2.2 Lensed quasar search techniques

We give a recap of lensed quasar search techniques before we start presenting the development of our time-variability-based lens search algorithm. Besides the lensed quasars that were serendipitously discovered, the attempts of systematic lensed quasar searches can be traced back in the early eighties, though around that time the further usages of lensed quasars, such as time delay measurement, were challenging due to the observational limitation. We are not going to review all the lensed quasar search techniques from 1980 to 2020 here. We will describe only some common techniques used in lensed quasar searches. The categorization here might have some ambiguity; certain techniques mentioned here are more general and can be applied across different surveys with adaptation, while certain techniques are more survey-based due to the exploitation of the specifics of certain surveys.

In section 2.2.1, we introduce a lensed quasar search method using the time variability of lensed quasar. This variability-based method has not yet been largely or systematically used in practical and is more like a concept with successful demonstrations. Building a practical lens search algorithm based on this variability-based method is the motivation behind this thesis.

- *Exploiting lensing magnification.* One intuitive and straightforward concept of searching for lensed quasars is to use the advantage of lensing magnification (equation (2.13)). Since the high-luminosity quasars might be the magnified/lensed version of quasars with usual luminosity (e.g., Sanitt, 1971), there are systematic searches that looks into the brightest quasars for lensed quasars. In addition to the early lensed quasar discoveries through the lensing magnification from ground-based surveys (e.g., Weymann et al., 1980; Surdej et al., 1987; Magain et al., 1988), part of the HST snapshot survey observed around 500 the known brightest quasars above redshift $z = 1$ with the aim to discover such magnified/lensed version of quasars (Bahcall et al., 1992; Maoz et al., 1992; Maoz et al., 1993a; Maoz et al., 1993b), though they did not find any new lensed quasar. More recently, McGreer et al. (2013) used the HST imaging to observe spectroscopic confirmed quasars above redshift $z = 5$, as the detectability of those distant quasars might result from the lensing magnification, and they found at least one candidate of lensed quasar.

- *Observing with radio wavelengths*. At radio wavelengths, the dust obscuration in the foreground galaxies does not contaminate the radio sources, and the radio sources are also not affected by the microlensing events induced by the stars in the foreground galaxies, due to the fact that radio emitting regions of quasars are larger than the Einstein radius of stars. Furthermore, radio observations are less sensitive to environmental conditions (e.g., atmosphere and weather), leading to uniform sensitivity and resolution over the entire survey. As a result, though only ~10% of all quasars are radio-loud, the first successful systematic lensed quasar search[3] has been carried out by the Cosmic Lens All Sky Survey (CLASS; Myers et al., 2003; Browne et al., 2003) in radio wavelengths. CLASS used high-quality (0.2″) 8.46 GHz images from the VLA for 13783 radio sources with compact flat-spectrum, and inspecting for the sources with resolved multiple components. A flat-spectrum radio source has intrinsic structure dominated by a "radio core" ~1 mas, so it is naturally a lens candidate if it has multiple compact components in a ~200-mas resolution radio observation. Moreover, a flat-spectrum radio source is usually time-variable, so it will be more likely a lensed quasar if it is multiply-imaged. For the compact flat-spectrum radio sources with resolved multiple components, CLASS further used Multi-Element Radio-Linked Interferometer Network (MERLIN) and the Very Long Baseline Array (VLBA) for higher-resolution follow-ups. There are ~20 new lensed quasars found by CLASS.

- *SQLS/BQLS*. In the optical, the SDSS[4] Quasar Lens Search (SQLS; Oguri et al., 2006; Inada et al., 2008; Inada et al., 2010; Inada et al., 2012) is the first prominent systematic lensed quasar search. SDSS images 10^4 deg^2 of the sky and conducts spectroscopy of galaxies, quasars, and stars from the imaging data in *u*-, *g*-, *r*-, *i*-, and *z*-bands. Mainly due to *u*-band imaging, the spectroscopic confirmation of quasars is reliable. Starting from the reliable SDSS spectroscopically selected quasars, which means that the lensed quasar search only needs to look for lensed feature among these SDSS spectroscopically selected quasars without the need to confirm the variable nature, SQLS first constructed a statistical subsample of quasars with redshifts $0.6 \leq z \leq 2.2$, *i*-magnitude $15.0 \leq i \leq 19.1$, and SDSS imaging parameter `PSF_WIDTH` > 1.8″. SQLS further used two selections with the SDSS imaging parameters

[3]The first statistical sample of lensed quasars
[4]SDSS, Sloan Digital Sky Survey (York et al., 2000)

to inspect for lensed features and pick out lensed quasar candidates from the statistical subsample (of quasars). One is the morphological selection, which aims to find small separation lensed quasars ($\theta \lesssim 2.5''$) with main requirement of poorly fitted Point-Spread-Function (PSF). The other is the colour selection, mainly requiring the multiple components to have similar colours. After visual inspection and follow-ups, SQLS in total found 62 lensed quasars, including 13 previously known lensed quasars. More et al. (2016b) applied similar techniques to BOSS[5] and discovered 13 new two-image (double) lensed quasars .

- *Detecting through lensed image specifics*. Since the patterns of lensed images are ruled by the lens equation and the caustic curves (section 2.1), the image configuration of a lens system is actually specific. Therefore, examining the image patterns of confirmed/possible quasars is a way to find lensed quasars. For example, CHITAH (Chan et al., 2015) examines images by modelling the lens mass, as the image configuration of a lens system should be explained by a lens model. Since machine learning is powerful in image recognition, the machine learning techniques, such as gradient boosting could also be applied in identifying the lensing pattern (e.g., Agnello et al., 2015a). Although not specific to lensed quasar, citizen science - using the advantage of many pairs of eyes, is also useful for lensed quasar searches (Marshall et al., 2016; More et al., 2016a; Sonnenfeld et al., 2020).

- *Exploring color and magnitude spaces*. In color and magnitude spaces, lensed quasars are no longer like the unlensed quasars, and they are also not like galaxies. Therefore, exploiting this uniqueness in color magnitude spaces with various color and magnitude cuts is also a technique looking for lensed quasars. For example, one can search for lensed quasars by looking into the outliers which will be discarded if applying normal cuts for (unlensed) quasars and galaxies in optical and mid-infrared magnitude spaces Agnello (2017).

  Machine learning can also be used in finding the color and magnitude cuts for lensed quasars. Agnello et al. (2015b) used Artificial Neural Network (ANN)

[5]BOSS, the Baryon Oscillation Spectroscopic Survey (Dawson et al., 2013), part of the SDSS but with more higher redshift objects

trained with DES[6] magnitudes and morphology information to look for lensed quasars and found two doubles. Ostrovski et al. (2017) used Gausian Mixed Models with DES, VHS[7], and WISE[8] magnitudes to find lensed quasar and found one double.

- *Using Gaia detection*. With the exceptional resolution (FWHM ~0.1″), *Gaia* (Gaia Collaboration et al., 2016) provides alternative approaches to lensed quasar searches through its multiple detection, multiplets, as they might be the detection of individual lensed images. From a preselected quasar catalog like SQLS/BQLS, one can look for *Gaia* multiplets around each quasar candidates as a way to find lensed quasar; even there is no multiplet, one can also search for lensed quasars by comparing the flux and position offsets between *Gaia* and other lower-resolution surveys, as the flux and position would shift among well-resolved and deblended images. Lemon et al. (2017), Lemon et al. (2018), Ostrovski et al. (2018), and Rusu et al. (2018) have conducted lensed quasar searches using *Gaia* multiplets or flux and position comparison with SDSS, Pan-STARRS[9], and they found ~100 lensed quasars.

2.2.1 Variability-based method

Lensed quasars are not only lens systems, but also variable sources[10]. Kochanek et al. (2006a) first suggested to use image subtraction methods - the difference images, which display the time variabilities of variable objects, to identify lensed quasars through their variabilities. In a cadenced survey, in which the telescope repeatedly visits a same field, the non-variable contaminations like galaxies are eliminated by the difference imaging, and only variable sources appear in the difference images. While almost the other variable sources are point-like objects, lensed quasars have multiple components in each system; in principal one can recognize a lensed quasar as a multi-component (or extended if not deblended) source in the difference images from a cadenced survey.

[6]DES, Dark Energy Survey (Sánchez and Des Collaboration, 2010)

[7]VHS, VISTA Hemisphere Survey (McMahon et al., 2013)

[8]WISE, Wide-field Infrared Survey Explorer (Wright et al., 2010)

[9]Pan-STARRS, Panoramic Survey Telescope and Rapid Response System (Chambers et al., 2016)

[10]In this thesis, the variable sources are brightness-variable sources.

Kochanek et al. (2006a) further demonstrated this variability-based idea on four known lensed quasars, QJ0158−4325 (Morgan et al., 1999), SDSS0924+0219 (Inada et al., 2003), RXJ1131−1231 (Sluse et al., 2003), and Q2231+0305 (Huchra et al., 1985). They monitored these four lensed quasars with the SMARTS[11] 1.3-meter telescope in *R*-band, and using the difference imaging package from Alard (2000) to perform the image subtraction. In their difference images of those four lensed quasars, everything other than the lensed quasars vanishes, and the four lensed quasars are easily seen as multi-component or extended sources. Lacki et al. (2009) also tested this variability-based concept on the lensed candidates from SQLS and one serendipitously discovered lensed quasar in the SDSS Supernova Survey region, and recovering the one known lensed quasar with a low false-positive rate of order ∼1/4000.

The successful demonstrations encourages the attempts to systematically exploit the time variability for lensed quasar searches. Being inspired by Kochanek et al. (2006a), we aim to establish a technique using difference imaging to find lensed quasars. It is important that this to-be-developed lensed quasar search technique is realistic and practicable. Therefore, we take the advantage of the ongoing cadenced survey, Hyper Suprime-Cam transient survey which will be introduced in chapter 3, to develop and test the variability-based lens search algorithm.

[11] Small and Moderate Aperture Research Telescope System (Subasavage et al., 2010)

Chapter 3

OBSERVATION

For an astronomical method that is expected to be applied to observational data, it is essential that the method itself is realistic and had better been tested on real datasets from observations. For our time-variability-based lensed quasar search algorithm, we are fortunate that there is Hyper Suprime-Cam transient survey for us to simulate (chapter 4), to test (chapter 4), and even to apply (chapter 5). As this thesis heavily depends on the Hyper Suprime-Cam Subaru Strategic Program survey and their cadenced survey, Hyper Suprime-Cam transient survey, we briefly summarize the former in section 3.1, and give a short introduction for the later in section 3.2.

3.1 Hyper Suprime-Cam Subaru Strategic Program (HSC-SSP) survey

The Hyper Suprime-Cam Subaru Strategic Program (HSC-SSP) survey (Aihara et al., 2018) is a deep and wide-field imaging survey using the Hyper Suprime-Cam (HSC) (Miyazaki et al., 2018; Komiyama et al., 2018; Kawanomoto et al., 2018; Furusawa et al., 2018), which is a giant digital camera on the 8.2-meter Subaru telescope. Figure 3.1 is the illustration of the HSC. The HSC-SSP survey images 1400 deg^2 of sky with five broad bands (g-, r-, i-, z-, y-) and four narrow bands (NB387, NB816, NB921, NB101). Figure 3.2 shows the bandpasses of the five broad bands and four narrow bands. With the combination of the Subaru's large aperture, the HSC's large field of view (1.5 degree diameter), and the superb image quality of the site, the main science goal of the HSC-SSP survey is to tackle the fundamental questions in cosmology and astrophysics, such as the physical nature of dark matter and dark energy, galaxy formation and evolution, and the reionization in high redshift universe. Throughout this thesis, the two terms, the HSC survey and the HSC-SSP survey, are mutually used.

The focal plane of the HSC consists of 116 CCD chips (CCDs), and each CCD has 2048×4096 pixels ($5.73'' \times 11.47''$). Figure 3.3 shows the 116 CCDs of the HSC. Among the 116 CCDs, 104 chips are used for science, four chips are used for auto-guiding, and eight chips are used for focus-monitoring. The 104 science chips cover a 1.5 degree diameter field of view with a pixel size of 0.168 arcsec. The

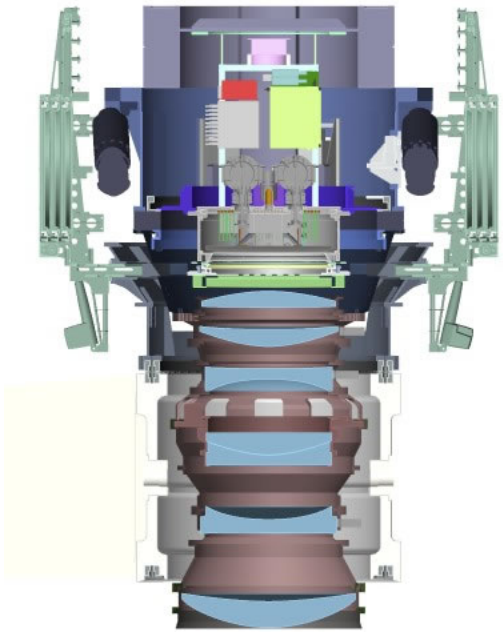

Figure 3.1: The illustration of the three-meter tall and three-ton heavy giant digital camera of HSC. Image credit: The Hyper Suprime-Cam Subaru Strategic Program (HSC-SSP) and National Astronomical Observatory of Japan (NAOJ).

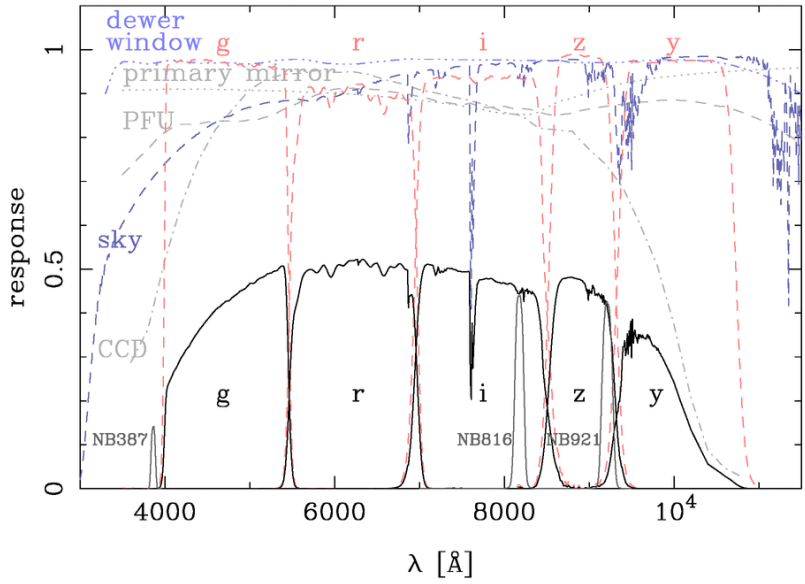

Figure 3.2: The bandpasses of the HSC. Image credit: HSC-SSP and NAOJ.

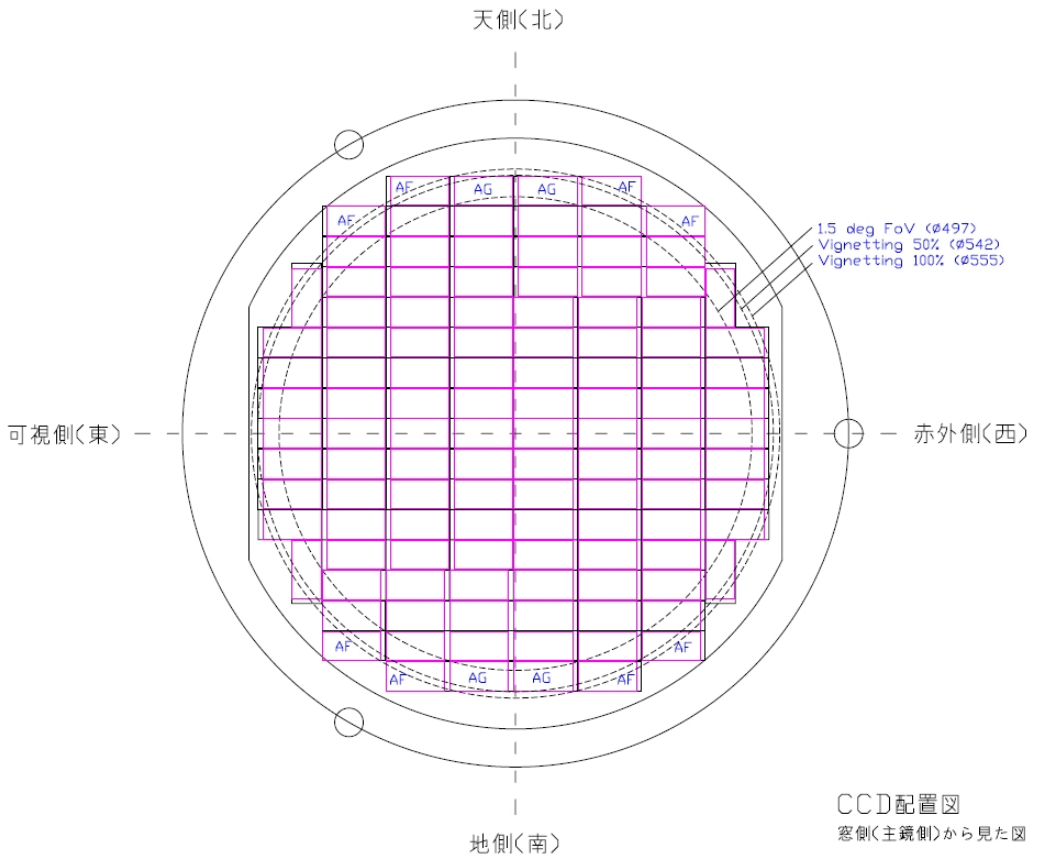

Figure 3.3: The arrangement of 116 CCDs in the HSC. The magenta rectangles are the illustrations of 116 CCDs. Each CCD has 2048×4096 pixels on the focal plane. The gaps between CCDs are $\sim 12''$ (vertical in this figure) and $\sim 53''$ (horizontal in this figure). The 104 chips used for science are in blue, four chips used for auto-guiding are labeled as "AG", and eight chips used for monitoring the focus are labeled as "AF". Image credit: HSC-SSP and NAOJ.

image quality is excellent across the field of view with a median seeing of 0.6 arcsec in *i*-band.

The HSC survey observes three layers at different depths, Wide, Deep, and UltraDeep. Figure 3.4 illustrates the HSC-observed fields at different layers. Their covering areas and depths are summarised in table 3.1, and the covered fields are listed in table 3.2. The key science in the Wide layer is the cosmology with weak lensing observables, while in the Deep and UltraDeep layers, the main science drivers are the study of galaxy and AGN evolution over cosmic time, and the survey of using high-redshift supernovae as a cosmological probe. The HSC survey is conducted for 300 nights starting in 2014, and it is designed that 2/3 of the observing

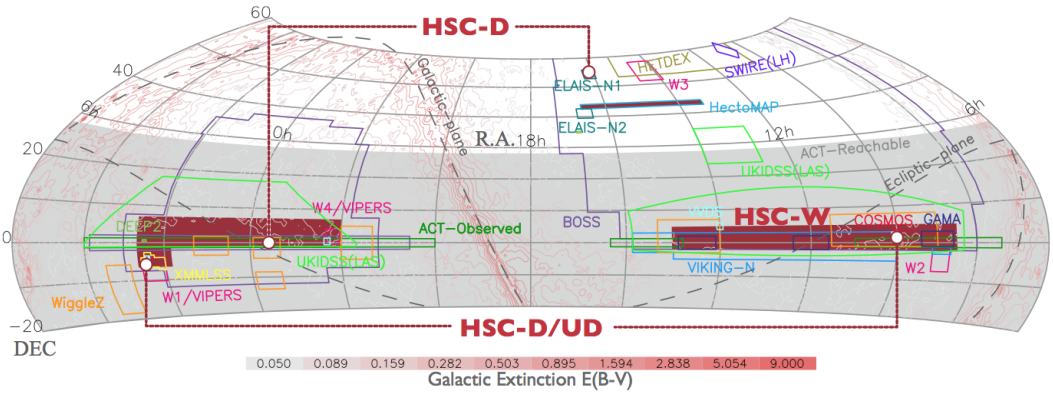

Figure 3.4: The fields of Wide (HSC-W), Deep (HSC-D), and UltraDeep (HSC-UD) layers. Image credit: HSC-SSP and NAOJ.

Layer	Area [deg^2]	Depth
Wide	1400	*i*-band ∼26 mag
Deep	26	*i*-band ∼27 mag
UltraDeep	3.5	*i*-band ∼28 mag

Table 3.1: The covering areas and depths of the three layers in the HSC survey (Wide, Deep, and UltraDeep).

time is dedicated to the Wide layer, and 1/3 of the observing time is dedicated to the Deep and UltraDeep layers.

The data products from the HSC survey are processed by a software package, `hscPipe` (Bosch et al., 2018), with the aim that the science studies could be conducted directly with the measured quantities from `hscPipe` without the need of re-analysing the images. For image processing, the sky is divided into `Tracts`, a predefined grid covering 1.7×1.7 square degree of sky. Each `Tract` is further divided into 9×9 subareas called `Patches`. Each `Patch` is a square with ∼12 arcminutes on the side. Each exposure from the CCD is called `visit`. After the `visits` are corrected for various effects (bad pixels, chip non-linearity, and etc.), bias-subtracted, and flat-fielded, `hscPipe` performs multi-visit processing to generate coadded images of multiple exposures. Objects are detected through the coadded images and further used to measure the photometric and astrometric properties.

Layer	Field name	(RA, DEC)
Wide	North field	13:20 ≤ RA ≤ 16:40 & 42° ≤ DEC ≤ 44.5°(≃ 90deg^2)
	Spring equatorial field	08:30 ≤ RA ≤ 15:00 & −2° ≤ DEC ≤ 5°(≃ 680deg^2)
	Fall equatorial field	22:00 ≤ RA ≤ 02:40 & −1° ≤ DEC ≤ 7°(≃ 630deg^2)
Deep	XMM-LSS	(02:23:15.33, −05:18:30.67)
		(02:22:22.43, −04:03:44.48)
		(02:27:19.86, −04:27:47.42)
	E-COSMOS	(09:57:28.60, +02:57:21.00)
		(10:03:28.60, +02:57:21.00)
		(09:57:28.60, +01:27:21.00)
		(10:03:28.60, +01:27:21.00)
	ELAIS-N1	(16:11:00.81, +53:56:30.71)
		(16:15:46.66, +54:59:17.74)
		(16:10:54.07, +56:02:49.65)
		(16:06:16.19, +54:59:16.91)
	DEEP2-3	(23:32:08.46, +00:16:49.43)
		(23:27:02.16, +00:16:49.41)
		(23:29:26.53, −00:50:38.94)
		(23:24:12.60, −00:49:46.61)
UltraDeep	COSMOS	(10:00:28.60, +02:12:21.00)
	SXDS	(02:18:15.60, −04:51:00.00)

Table 3.2: The details of the fields covered by the HSC survey.

3.2 The HSC transient survey

The HSC transient survey (Yasuda et al., 2019) carries out cadenced observation as part of the HSC-SSP survey. Comparing to other present cadenced surveys, the HSC transient survey is unique in its depth and volume. Furthermore, the HSC transient survey has excellent image quality as a ground-based cadenced survey. The cadenced observation of the HSC transient survey is conducted in the UltraDeep fields, COSMOS and SXDS (table 3.2). So far, the cadenced observation has been done in the COSMOS field, covering 1.77 deg^2 of the UltraDeep layer. The strategy for cadence is to observe in two epochs separated by 7-10 days with all the broad bands (*g*-, *r*-, *i*-, *z*, *y*-) during each monthly observation run in the UltraDeep layer. Ideally, there would be 12 epochs for all the five broad bands over six months.

The data of the HSC transient survey is processed at a night-by-night basis. For one night, the coadded images are first created from the `visits` (exposures) by `hscPipe` as described in section 3.1, and the HSC transient survey further uses the Alard & Lupton method (Alard and Lupton, 1998; Alard, 2000) to generate the difference images. The Alard & Lupton method takes subtraction of two images with different seeings with more efficient CPU cost comparing to other image subtraction meth-

ods, while also taking into account the point-spread-function (PSF) variations and differential background variation.

The HSC transient survey uses the data taken from March 2014 to April 2016 to create the reference deep coadded images for the difference imaging, and only the data with seeing better than 0.7 arcsec are used. The difference imaging by the HSC transient survey performs the image subtraction for each warped images (corrected visits) with the reference deep coadded images, and these warped difference images (corrected visits subtracted by the reference image) are further coadded to become deep difference images. It is the deep difference images that are used to detect and measure sources.

When we start to build the time-variability-based lensed quasar search algorithm in chapter 4, we will mention more details about the HSC transient survey related to the development of the time-variability-based lensed quasar search algorithm in section 4.2.

Chapter 4

A TIME-VARIABILITY-BASED LENS SEARCH ALGORITHM

Like what we have mentioned in section 2.2.1, a cadenced survey reveals the time variabilities of variable objects with difference imaging, which is a powerful tool to remove the contamination from the non-variable objects. Kochanek et al. (2006a) first proposed the method using difference imaging to find lensed quasars: since almost all the non-lensed variable objects are point sources, the extended variable objects appearing in the difference images would be potential lenses.

As a cadenced survey, the upcoming Rubin Observatory Legacy Survey of Space and Time (LSST)[1] will provide not only a huge pool of new lensed quasars, but also a great opportunity to apply the time variability for lens search. The LSST is expected to detect thousands of lensed quasars (Oguri and Marshall, 2010, hereafter OM10), and one could use the difference imaging as an efficient method to find lensed quasars through their variability. Inspired by Kochanek et al. (2006a), we develop a lens search algorithm for lensed quasars based on their time variability. The HSC transient survey we introduce in chapter 3 provides a great opportunity to simulate the difference images that could be used for the development of the lens search algorithm and to test the lens search performance. The HSC transient survey has similar image quality that is expected for the LSST.

In this chapter, we build a simulation pipeline for producing time-varied images of lensed quasars, and apply the simulation pipeline to the HSC transient survey to generate HSC-like difference images of mock lensed quasars. With the HSC-like difference images of lensed quasars, we develop a lens search algorithm that picks out variable objects with large spatial extent in the difference images and classifies them as lensed quasar candidates. We further test the performance of our lens search algorithm in the HSC transient survey.[2] Most of the material in this chapter

[1] LSST (Ivezić et al., 2019)

[2] Although the simulation and the search algorithm could also be applied to lenses with two-image configurations (double), we focus on lenses with four-image configuration (quad). In spite of the higher number of doubles than quads, quads provide more constraints on the lens potential distribution and stellar mass fraction. Furthermore, the configuration of quads is so unique that it is

is published in Chao et al. (2020).

The organization of this chapter is as follows. In section 4.1, we present a new simulation pipeline of time-varied lensed images, and apply the new simulation pipeline to the HSC transient survey in section 4.2. The lens search algorithm is detailed in section 4.3. The lens search performance is shown in section 4.4 before a summary in section 4.5. For extra examinations of the lens search performance, we refer the reader to Appendix A.

4.1 Simulation of time-varying lensed quasars images

We present a simulation pipeline for creating realistic images of mock lensed quasars in a series of time. The mock images produced by this pipeline are useful for developing the time-variability-based lens search algorithm. We use the mock configuration from the catalog created by OM10 to generate the simulated lensed quasars. In order to have realistic simulations, we simulate not only the light from the variable object - the lensed quasar in this work - but also the light from the (lensed) host galaxy and lens galaxy. This also takes into account possible residuals on the difference image due to potential imperfection of the difference imaging method. The flowchart of this simulation pipeline is shown in figure 4.1.

4.1.1 Mock lenses from OM10

OM10 have predicted the distribution of lensed quasars, and produced a mock catalog of lensed quasars. For each lens system, OM10 provides the source position (η_1, η_2), the source redshift z_s, the unlensed i-band magnitude m_s of the quasar, the lens redshift z_d, the velocity dispersion σ, the ellipticity e, and the position angle (PA) θ_e of the lens galaxy. OM10 also provides the lensed image positions, the magnifications, and the time delays calculated by GLAFIC (Oguri, 2010), with the assumption of a singular isothermal ellipsoid (SIE) model (Kormann et al., 1994) for the lens and an external shear accounting for the effect of the lens environment (e.g. Kochanek, 1991; Keeton et al., 1997; Witt and Mao, 1997). The convergence

unlikely to be mistakenly identified, while many objects such as quasar binaries are easily mistaken as doubles.

κ from the SIE model of the lens is given by

$$\kappa(\theta_1, \theta_2) = \frac{\theta_{\rm Ein}\sqrt{1-e}}{2} \frac{\lambda(e)}{\sqrt{\theta_1^2 + (1-e)^2\theta_2^2}}, \tag{4.1}$$

where (θ_1, θ_2) is the coordinate of the lens, $\theta_{\rm Ein}$ is the Einstein radius in arcsec, e is the ellipticity, and $\lambda(e)$ is the dynamical normalization defined in Oguri et al. (2012). The lens potential of the external shear ϕ is given by

$$\phi(\theta_1, \theta_2) = \frac{\gamma}{2}(\theta_1^2 - \theta_2^2)\cos 2\theta_\gamma + \gamma\theta_1\theta_2 \sin 2\theta_\gamma, \tag{4.2}$$

where γ is the magnitude of the external shear and θ_γ is the orientation of the external shear.

4.1.2 Quasar

For the point sources, i.e. the lensed quasars without the (lensed) host galaxies, we use the source redshift $z_{\rm s}$, the unlensed i-band magnitude $m_{\rm s}$, the lensed image positions, the magnifications, and the time delays provided by OM10, to generate the simulated image for each lensed quasar.

We generate the source light curve of quasars using CARMA_PACK (Kelly et al., 2009; Kelly et al., 2014) based on $z_{\rm s}$ and $m_{\rm s}$ from OM10. CARMA_PACK is developed to quantify stochastic variability, especially for quasar variability, and the quasar light curves are generated with the damped-random-walk model based on magnitude m and the fitting relation on redshifts z in Kelly et al. (2009). We then shift (in time) and magnify the generated source light curve according to the time delay and the magnification of each lensed image.[3]

Figure 4.2 is an illustration of the procedure to generate light curves for lensed quasars without the (lensed) host galaxies. In the left panel, we show the positions of the four multiple images of a symmetry quad lensed by a galaxy at $z_{\rm d} = 0.23$ from OM10 with source redshift $z_{\rm s} = 3.26$. The four multiple image positions, A, B, C, and D in the left panel, are relative to the lens galaxy, which is at the center for each lens system in OM10, $(x, y) = (0, 0)$ (black cross in the left panel). Their magnifications, $|\mu_{\rm A}|$, $|\mu_{\rm B}|$, $|\mu_{\rm C}|$, and $|\mu_{\rm D}|$, and the time delays relative to Image B, $\Delta t_{\rm AB}$, $\Delta t_{\rm CB}$,

[3]We do not explicitly include microlensing variability. The lensed quasar variability is changed but not canceled out by microlensing variability, so lensed quasars will still appear as multiple-point like variable objects in the difference images even when there is microlensing effect.

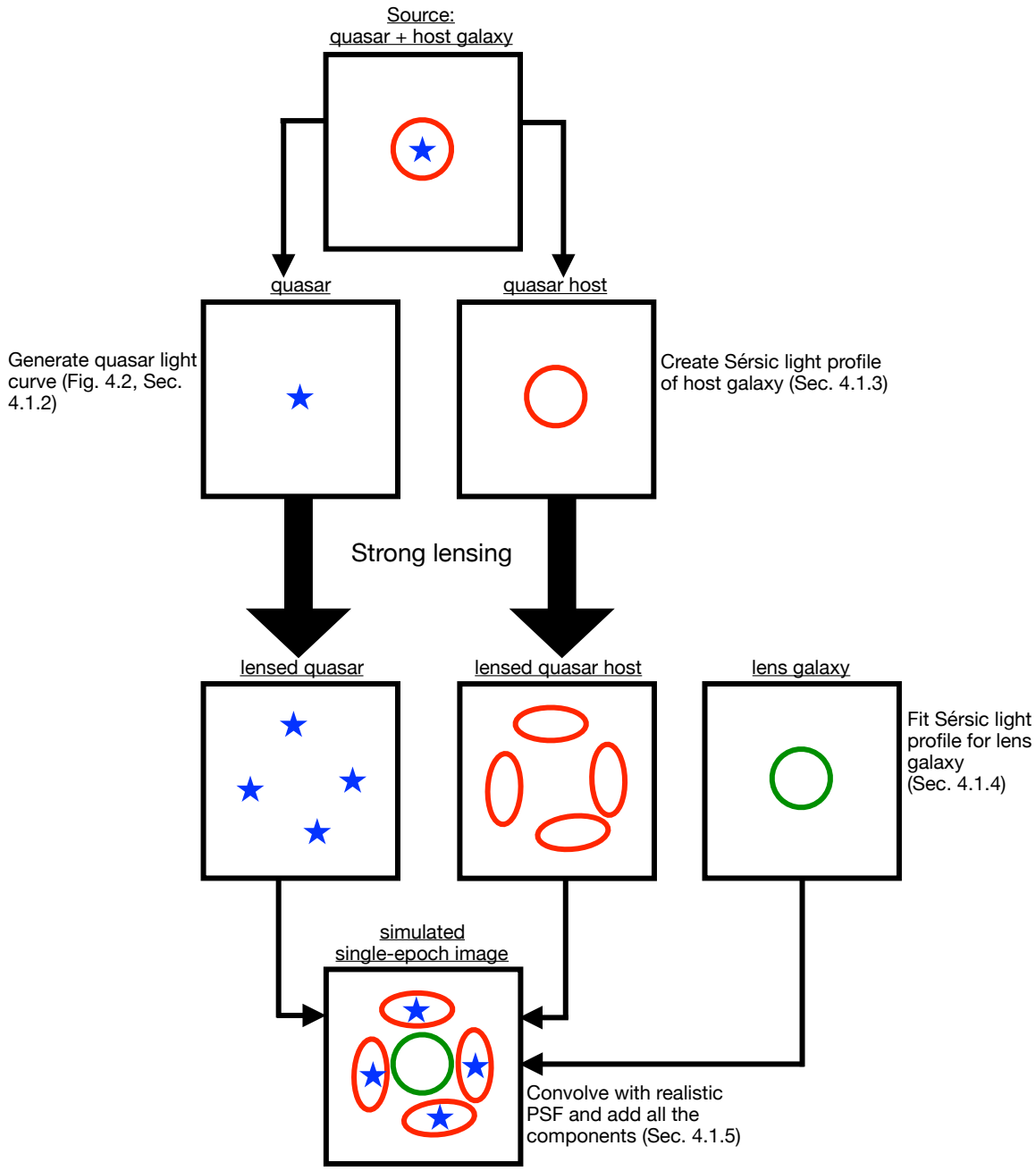

Figure 4.1: Flowchart illustrating the simulation of time-varying lensed quasars images. For quasars, we generate mock quasar light curves based on their source redshifts z_s, shifting in time and magnifying the mock quasar light curves on the image plane (see figure 4.2). For quasar hosts, we create their Sérsic light profiles on the source plane, and produce their lensed images on the image plane assuming a SIE model. For lens galaxies, we pick galaxies from a real survey based on their lens redshifts z_d and velocity dispersions σ, fitting the selected galaxies with Sérsic light profiles, and using the fitted Sérsic light profiles to produce their images on the image plane. Once we have all the components for one lens system (image of lensed quasar, image of lensed quasar host, and image of lens galaxy), we convolve them with a realistic PSF and add them to obtain one complete image.

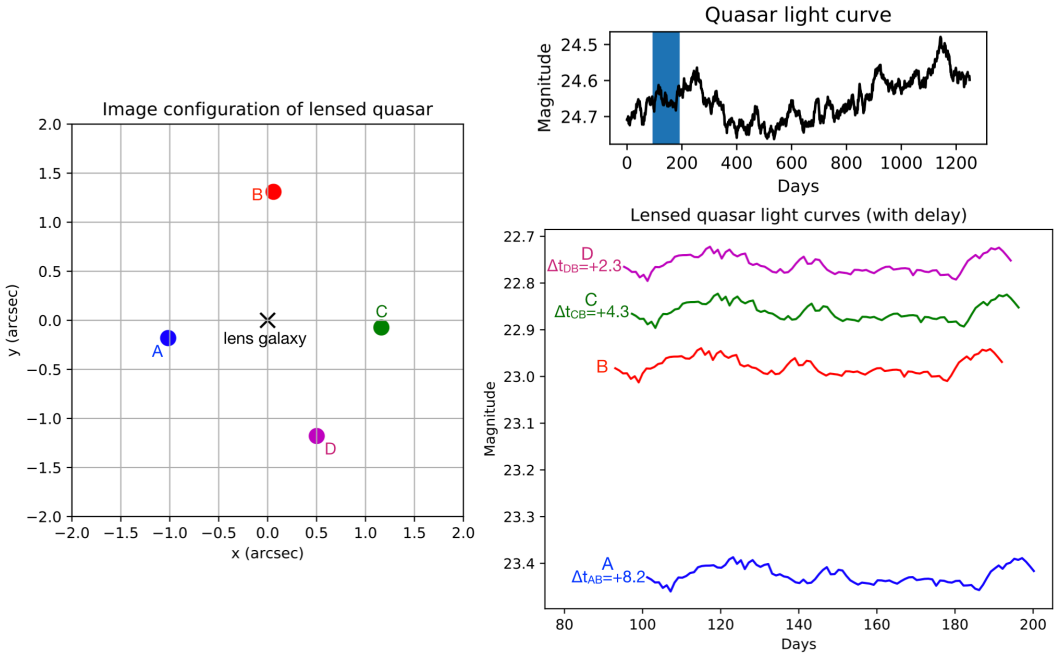

Figure 4.2: Illustration of generating light curves for a lensed quasar without its (lensed) host galaxy. Left: positions of the four multiple images (A, B, C, and D) and the lens galaxy (cross). Top-right: mock quasar light curve. Bottom-right: the lensed light curves of the four multiple images in the left panel, for the period marked by the blue band in the top-right panel.

Image	Magnification ($\|\mu\|$)	Time Delay (Δt) (in days relative to Image B)
A	3.1	+8.2
B	4.7	0
C	5.2	+4.3
D	5.7	+2.3

Table 4.1: Magnifications and time delays of the lensed quasar in figure 4.2.

and $\Delta t_{\rm DB}$, are listed in table 4.1 (where $\Delta t_{\rm XB} = t_{\rm X} - t_{\rm B}$). The source light curve that we generate with CARMA_PACK based on the source redshift $z_{\rm s} = 3.26$ is shown in the top-right panel of figure 4.2. The bottom-right panel of figure 4.2 shows the light curves of the four multiple images (A, B, C, and D in the left panel), which are produced by shifting and magnifying part of the source light curve in the top-right panel (blue band) with the corresponding time delays and magnifications in table 4.1.

Property	Min.	Max.
$\log L_{\rm host}$ ($L_\odot$)	9	13
e	0	0.8
θ_e (deg)	0	180
$r_{\rm e}$ (kpc)	1	10
n	1	5

Table 4.2: Ranges of the quasar host galaxy properties - luminosity $L_{\rm host}$, ellipticity e, PA θ_e, effective radius $r_{\rm e}$, and Sérsic index n.

4.1.3 Quasar host galaxy

Since OM10 provides only the configuration of point sources and there is no definite morphological relation between quasar and the host galaxy with little scatter, we randomly draw the morphological properties based on the Sérsic profile for the host galaxy of quasar and use GLAFIC (Oguri, 2010) to generate the lensed image of host galaxy. We conservatively adopt broad ranges for the parameters in the Sérsic profile of the host galaxy (based on, e.g., Blanton and Moustakas, 2009; Peng et al., 2006b; Park et al., 2015; Bennert et al., 2010). The thresholds of the host galaxy properties used in generating the lensed images are listed in table 4.2.

We put the host galaxy with its random Sérsic profile at the same source position as the (unlensed) quasar provided by OM10, and we adopt the same SIE model, external shear, and cosmology from OM10 for GLAFIC to generate the lensed image of the host galaxy. Therefore, the lensed host galaxy image positions will be consistent with the lensed quasar image positions.

4.1.4 Lens galaxy

For the lens galaxies, we assign the light profile to the lens galaxy for each lens system with fitted profile of galaxy from a real survey, as only the mass model of lens galaxy is given by OM10. We denote such a real survey "$S_{\rm imag}$", and $S_{\rm imag}$ could be any survey where one is interested in finding lens systems, such as the Sloan Digital Sky Survey (SDSS) or the HSC survey.

We begin with a catalogue created by cross-matching the galaxies from $S_{\rm imag}$ with another survey "$S_{\rm spec}$", which provides spectroscopic redshift $z_{\rm spec}$ and velocity dispersion $\sigma_{\rm spec}$. We note that if $S_{\rm imag}$ itself has information about spectroscopic

redshift and velocity dispersion, one does not have to cross-match $S_{\rm imag}$ with another survey. From the cross-matched catalogue, we select "matched galaxies" for each lens galaxy with the closest values to the lens redshift $z_{\rm d,OM10}$ and the velocity dispersion $\sigma_{\rm OM10}$ from the mass model provided by OM10. We first select the galaxies with

$$|d_z| < 0.01 \tag{4.3}$$

and

$$|d_\sigma| < \Delta\sigma, \tag{4.4}$$

where $d_z = z_{\rm spec} - z_{\rm d,OM10}$, $d_\sigma = \sigma_{\rm spec} - \sigma_{\rm OM10}$, and $\Delta\sigma$ is the error in $\sigma_{\rm spec}$ from $S_{\rm spec}$. We then get the matched galaxies from the selected galaxies with the smallest values of $d_{z,\sigma}$, where $d_{z,\sigma}$ is defined as

$$d_{z,\sigma} = \sqrt{d_z^2 + d_\sigma^2}. \tag{4.5}$$

Ideally, for one lens galaxy in OM10, we could have ten galaxies with the smallest $d_{z,\sigma}$ from the cross-matched catalogue as matched galaxies for the lens light. However, for some lens systems in OM10, the number of selected galaxies from equtaions (4.3) and (4.4) is not enough to have ten matched galaxies. For such cases, we take all the available galaxies passing the selection criteria (equations (4.3) and (4.4)) as matched galaxies. In this work, we use the data from the Sloan Digital Sky Survey Data Release 14 (SDSS DR14, Abolfathi et al. (2018)) as $S_{\rm spec}$.

The velocity dispersion $\sigma_{\rm SDSS}$ is limited in the cross-matched catalogue when $z_{\rm SDSS} > 1.04$, so we apply only equation (4.3) to select matched galaxies for the lens galaxy with $1.04 < z_{\rm d,OM10} < 1.57$; we select up to ten galaxies as the matched galaxies with the smallest values of d_z. Due to the lack of object with $z_{\rm SDSS} > 1.57$ in the cross-matched catalogue, we do not simulate lens system with $z_{\rm d,OM10} > 1.57$.

We then obtain the image for each matched galaxy from $S_{\rm imag}$, and fit the light distribution of the matched galaxy with the Sérsic profile. For the fitting, we define

$$\chi^2 = \sum_i^{N_{\rm p}} \frac{(I_{i,\rm fit} - I_{i,\rm data})^2}{\sigma_{i,\rm data}^2}, \tag{4.6}$$

and the reduced χ^2 as

$$\chi^2_{\rm reduced} = \frac{\chi^2}{N_{\rm p}}, \tag{4.7}$$

where $N_{\rm p}$ is the number of pixels used in fitting, $I_{i,\rm fit}$ is the fitted intensity of light, $I_{i,\rm data}$ is the observed intensity of light from $S_{\rm imag}$, and $\sigma_{i,\rm data}$ is the noise from $S_{\rm imag}$. We rank the matched galaxies by $\chi^2_{\rm reduced}$. The smaller $\chi^2_{\rm reduced}$ is, the higher the rank is.

After we have the fitted light profile for each matched galaxy, we compare the ellipticity from the fitted light profile, $e_{\rm fit}$, and the ellipticity from the mass model given by OM10, $e_{\rm OM10}$, according to the ranking order. For one matched galaxy, if $|e_{\rm fit} - e_{\rm OM10}| < 0.2$, we will pick the matched galaxy as the lens galaxy; otherwise, we check $e_{\rm fit}$ of the matched galaxy in the next lower rank. For the lens galaxy that has no matched galaxy with the satisfied value of $e_{\rm fit}$, we pick the matched galaxy with the smallest value of $\chi^2_{\rm reduced}$. In total, we simulate 2,033 quads with lens redshift $z_{\rm d,OM10} < 1.57$ from OM10.[4]

4.1.5 Simulated image with all components

Once we have the individual simulated parts of a whole lens system (the lensed quasar, the lensed host galaxy, and the lens galaxy), we will convolve them with the point-spread-functions (PSFs) in $S_{\rm imag}$ for each epoch and add the parts to become one complete image. The complete image in an epoch t is expressed as

$$I_t(x, y) = \big(I_{{\rm q},t}(x, y) + I_{\rm h}(x, y) + I_{\rm d}(x, y)\big) \otimes {\rm PSF}_t(x, y), \tag{4.8}$$

where $I_t(x, y)$ is the light distribution at position (x, y) of the complete image, $I_{{\rm q},t}(x, y)$ is the light distribution of lensed quasar, $I_{\rm h}(x, y)$ is the light distribution of (lensed) host galaxy, $I_{\rm d}(x, y)$ is the light distribution of lens galaxy, ${\rm PSF}_t(x, y)$ is the PSF from $S_{\rm imag}$, and $\otimes$ represents the convolution. After we generate complete images for all the epochs in $S_{\rm imag}$, we will have the images of the mock lensed quasar in the time series of $S_{\rm imag}$.

4.2 Application to the Hyper Suprime-Cam Survey

In this section, we demonstrate our simulation in the HSC transient survey, and describe how we generate realistic difference images that will be used to develop the search algorithm through the pipeline of the HSC transient survey.

[4]The properties of the quasar and the lens galaxy used in this chapter is available at https://github.com/danichao/OM10-quads-Z_d-1.57-

Observation date	Seeing (arcsec)
2016-11-25	0.83
2016-11-29	1.16
2016-12-25	1.25
2017-01-02	0.68
2017-01-23	0.70
2017-01-30	0.76
2017-02-02	0.48
2017-02-25	0.72
2017-03-04	0.69
2017-03-23	0.66
2017-03-30	0.98
2017-04-26	1.24
2017-04-27	0.58

Table 4.3: The HSC transient survey observation dates and seeing in *i*-band.

4.2.1 The HSC transient survey

Since OM10 has only *i*-band magnitude, we simulate lenses only in *i*-band. The HSC transient survey has 13 epochs (nights of observations) over six months for *i*-band (table 4.3).

To obtain the difference image for each epoch, we need the reference image to subtract from the single-epoch image. In the HSC transient survey, the reference images are the deep reference images produced by coadding multiple exposures from multiple epochs during March 2014 to April 2016 (table 4.4). Only the exposures with seeing better than $0.7''$ have been used in creating the deep reference images.

The HSC transient survey uses the method in Alard and Lupton (1998) and Alard (2000) for the difference imaging. The single-epoch image is created by coadding several warped images, and each warped image corresponds to a distortion-corrected image of the sky from a single exposure. For each epoch, the difference imaging has been performed on every warped images by subtracting the deep reference image to produce the warped difference images, and all the warped difference images are then coadded to create the deep difference image. The HSC transient survey convolves the exposures used in creating the deep reference image (table 4.4) with a kernel to match the PSF of each warped image when performing the difference imaging process.

To generate realistic deep difference image of the mock lenses, we select the locations that have no object within 5 arcsec, which we call "empty regions", and we inject our mock lenses into these empty regions with the HSC pipeline (Bosch et al., 2018) version 4.0.5, for both the warped images in each epoch and the deep reference image. Once the injection is done, we use the difference imaging method mentioned above to create the deep difference image of the mock lenses. Practically, we select 75 empty regions in the "patch" of sky identified with the HSC `Tract` = 9813, `Patch` = (3, 4), to inject the mock lenses. In this patch, 44 warped images from five epochs are used to create the deep reference image (table 4.4), and 175 warped images are used to create the deep difference images for all the 13 epochs in *i*-band.

4.2.2 Convolution with the HSC PSFs and lens injection

In order to obtain realistic deep difference image, we inject the mock lens into both the warped image and the deep reference image. For the warped images, the difference imaging method is sensitive to every warped images used to create the deep difference image for each epoch, so accounting for the variations in the PSFs of the warped images is crucial. Meanwhile, the deep reference image used for the subtraction is coadded, so weighting the variability from the dates in table 4.4 plays a more important role. We detail the injection methods for the warped image and the deep reference image below.

For the lens injection into the warped images of one epoch, we first simulate the images for the whole lens system as mentioned in section 4.1 accounting for the quasar variability in the epoch, and then we create the complete image by convolving with the PSFs of the empty region where the lens system is injected into the warped images. Since one epoch is composed of several warped images, the PSF of the same empty region changes across multiple warped images. Therefore, for one lens system in one epoch, the complete images are generated by convolving with different PSFs for different warped images, and we further inject the complete images into the corresponding warped images.

For the lens injection into the deep reference image, we first weight the images

Observation date	MJD	Number of exposures
2014-03-28	56744.4687	9
	56744.4723	
	56744.4759	
	56744.4874	
	56744.4911	
	56744.4950	
	56744.4987	
	56744.5024	
	56744.5061	
2015-01-21	57043.5571	16
	57043.5609	
	57043.5648	
	57043.5738	
	57043.5780	
	57043.5859	
	57043.5898	
	57043.5937	
	57043.6011	
	57043.6047	
	57043.6118	
	57043.6157	
	57043.6195	
	57043.6269	
	57043.6306	
	57043.6455	
2015-03-20	57101.3403	5
	57101.3489	
	57101.3562	
	57101.3854	
	57101.3925	
2015-05-21	57163.2518	12
	57163.2556	
	57163.2595	
	57163.2633	
	57163.2672	
	57163.2710	
	57163.2749	
	57163.2787	
	57163.2826	
	57163.2864	
	57163.2903	
	57163.2941	
2016-03-04	57451.4246	2
	57451.4645	

Table 4.4: The exposures used to create the deep reference image for the HSC patch ID, `Tract` = 9813, `Patch` = (3, 4), in *i*-band.

of the mock lens on an epoch basis by the number of the warped images used in one epoch, and unlike the lens injection into the warped images, we convolve the weighted image with the PSF from the deep reference image and further inject the mock lens directly into the deep reference image. In the deep reference image, the total light distribution at position (x, y), $I_{\rm ref}(x, y)$, could be described as

$$I_{\rm ref}(x, y) = \Big(\sum_t \frac{I_{{\rm q},t}(x, y) \cdot N_t}{N_{\rm total}} + I_{\rm h}(x, y) + I_{\rm d}(x, y) \Big) \otimes {\rm PSF}_{\rm ref}(x, y), \tag{4.9}$$

where t = 2014-03-28, ..., 2016-03-04 (table 4.4), $I_{{\rm q},t}(x, y)$ is the light distribution of lensed quasar in t, N_t is the number of warped images used in t, $N_{\rm total}$ is the total number of warped images ($N_{\rm total}$ = 44 in our work), $I_{\rm h}(x, y)$ is the light distribution of (lensed) quasar host galaxy, $I_{\rm d}(x, y)$ is the light distribution of lens galaxy, ${\rm PSF}_{\rm ref}(x, y)$ is the PSF from the deep reference image, and $\otimes$ represents the convolution. Injecting mock lenses into the deep reference image via this method takes into account the variability of lensed quasar across the multiple epochs used in the deep reference image.

We simulate the complete image for 2,033 quads ($z_{\rm d,OM10} < 1.57$) from OM10, and the size of each complete image is $10'' \times 10''$ with the lens at the center (top row in figure 4.3). The quads are injected into the empty region randomly, and the empty regions are used repeatedly for different quads. For simplicity, we do not add Poisson noise associated with the mock lens systems when injecting the quads into the empty region, given the small impact of the Poisson noise: We find that the sky background noise generally dominates over Poisson noise in single-epoch images, although the addition of Poisson noise would slightly affect the pixel counts for some bright or wide-separation lens systems (see section 4.4.1). We defer the inclusion of Poisson noise, and the propagation of noise from the single-epoch images into the difference images to future work. After the injection of the complete images, we apply the deep difference imaging method to obtain the deep difference image for the mock quads (bottom row in figure 4.3). As mentioned in section 4.2.1, we first get the warped difference images of injected lenses as intermediate products, and the deep difference images are created by coadding the warped difference images. The top row in figure 4.3 are examples of the single-epoch images we obtain after the lens injection processed by the pipeline of the HSC transient survey, and we could see the light from both the lensed quasar and the lens galaxy in each panel, which appear like "bright spots". The bottom row in figure 4.3 are the corresponding deep

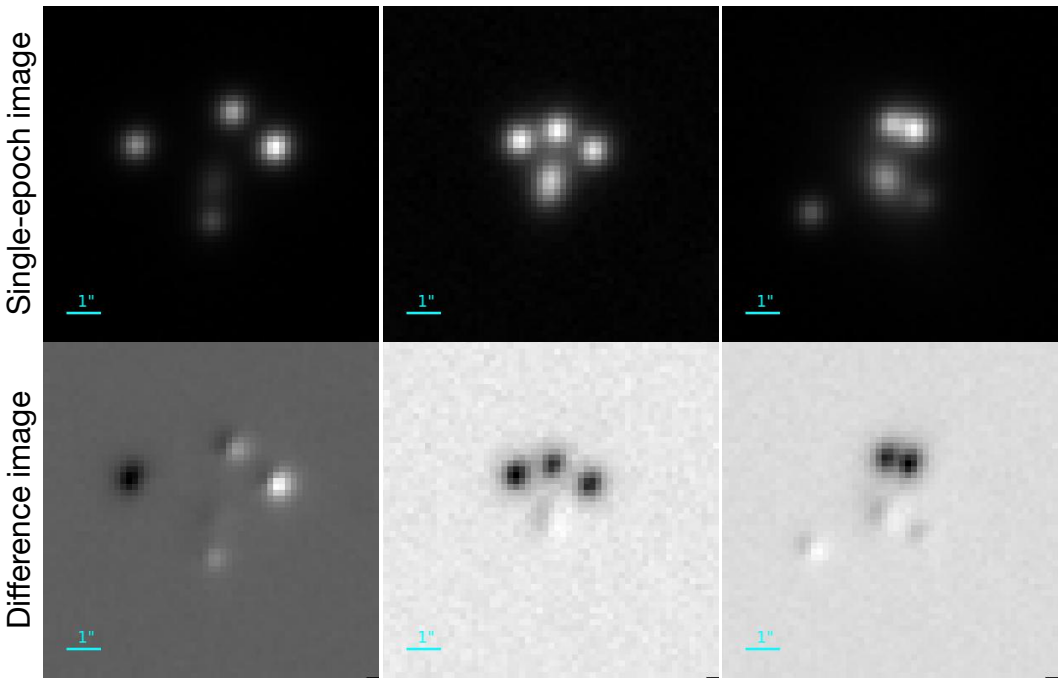

Figure 4.3: Examples of lenses injected into the HSC transient survey. Top: the single-epoch images coadded by the pipeline of the HSC transient survey. Bottom: the corresponding difference images of the top row produced by the image subtraction in the pipeline of the HSC transient survey. The size of each image cutout is $10'' \times 10''$.

difference images of the top row, and the "dark spots" (bright spots) are the spots that become fainter (brighter) than they were in the reference image. In contrast to the single-epoch images where we could only see bright spots and thus brightness changes are not obvious, brightness changes are clearly visible in the deep difference images through the dark spots (decreasing brightness) and the bright spots (increasing brightness). There are some residuals at the locations of the lens galaxies in the bottom panels of figure 4.3, which confirm that, simulating the light from all the components (quasar, host galaxy, and lens galaxy) instead of from only variable object (quasar) is important for realistic mock images, as the pipeline might not perform perfect subtraction for all the non-variable components.

4.3 Search method: spatial extent in difference image

With the multiple-image feature and the variable brightness, strongly lensed quasars are expected to exhibit multiple point-like image residuals in the difference image shown in figure 4.3. However, lensed quasars are often not deblended by the survey

pipelines, and most of them will show extended morphology. Since most astrophysical variable sources are isolated and point-like (e.g., variable stars, unlensed quasars, unlensed supernovae), targeting spatially extended or multiple-point-like variable sources in the difference image is an effective approach to find lensed quasars, as previously noted by Kochanek et al. (2006). We develop a lens search algorithm for lensed quasar via a method that (1) quantifies the extendedness of an object in the difference image and (2) selects objects that are large in spatial extent as lens candidates. We present the method that is based on the extendedness in section 4.3.1, and an enhancement of the method with a secondary criterion in section 4.3.2.

4.3.1 Quantification of the extendedness

The lens search algorithm starts from "HSC variables" in the HSC transient survey. In this work, we define a "HSC variable" as an object properly detected on the deep difference images at least twice in the HSC transient survey - the detections could be from two different epochs or two different bands. For each HSC variable, we first collect its deep difference images from all the 13 epochs (table 4.3), and create the "3σ-mask" for each epoch by picking out the pixels with value larger than 3σ or smaller than -3σ. The pixel values in the 3σ-mask, $I_{\rm mask}(i, j)$, are defined as

$$I_{\rm mask}(i,j) = \begin{cases} 1, & \text{if } |I(i,j)| > 3\sigma(i,j) \\ 0, & \text{otherwise} \end{cases} \tag{4.10}$$

where $i = 1, ..., N_x$ and $j = 1, ..., N_y$ are the pixel indices in both the deep difference image and the 3σ-mask of dimensions $N_x \times N_y$ ($N_x = N_y = 59$ in this work), $I(i, j)$ are the pixel values in the deep difference image, and $\sigma(i, j)$ are the estimated 1-σ uncertainties in the difference image from the HSC transient survey. Figures 4.4a and 4.4b are examples of the deep difference image and the 3σ-mask from a HSC variable in an epoch, respectively. As indicated in figure 4.4b, 3σ-mask has several noise peaks in the outskirts that are not related to the HSC variable. Those noise peaks should not be counted in the extendedness of the HSC variable, so we further define the "effective region" by

$$I_{\rm eff}(i,j) = \begin{cases} 1, & \text{if } \sum_{i'=i-1}^{i+1} \sum_{j'=j-1}^{j+1} I_{\rm mask}(i',j') > 2 \\ 0, & \text{otherwise} \end{cases} \tag{4.11}$$

where $I_{\rm eff}(i, j)$ is the pixel value of (i, j) in the effective region. Figure 4c shows the effective region of the HSC variable in figure 4a. Once we have the effective region,

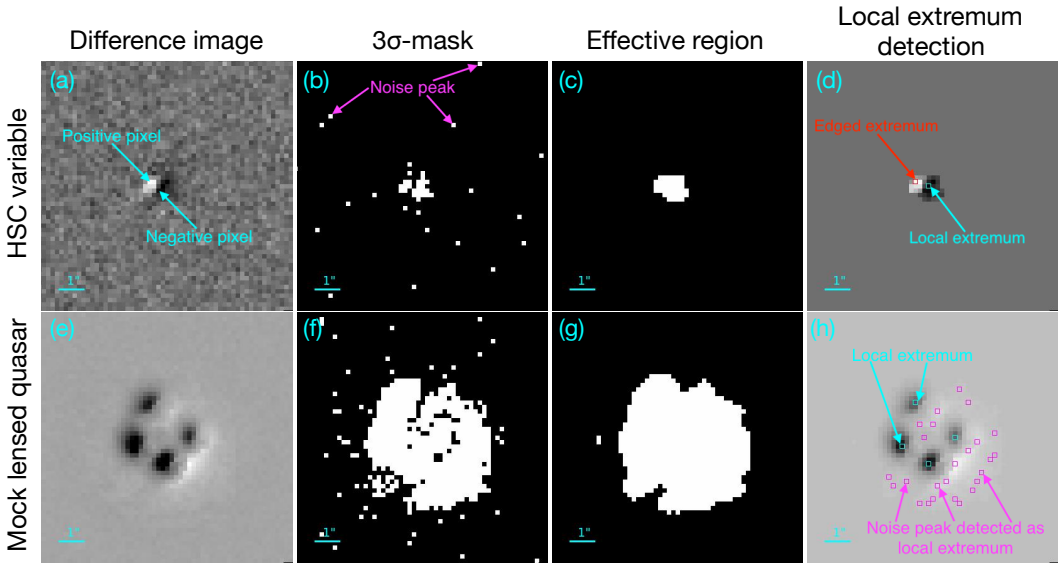

Figure 4.4: Examples of a HSC variable (top row) and an injected lensed quasar (bottom row). From left to right: difference image, the corresponding 3σ-mask, the corresponding effective region, and the corresponding local extremum detection. In 3σ-masks, the white pixels represent the pixels with values larger than 3σ or smaller than -3σ in the difference images. The effective regions marked by the white pixels show the spatial extent of the objects, after removing noise peaks in the 3σ-masks. In the local extremum detection, we pick out the pixels with values larger than all the neighbouring pixels or smaller than all the neighbouring pixels in the difference images within the effective regions; the local extrema indicated in cyan correspond to the "blobs" (See Section 4.3.2 for details) of the HSC variable/mock lensed quasar, the local extrema indicated in magenta are the noise peaks, and the pixel indicated as "Edged extremum" in red is a blob that should be picked out as local extremum but is missed because it is located at the edge of the effective region. The size of each image cutout is $10'' \times 10''$.

we determine the area of the effective region, $A_{\rm eff}$, by the sum of the pixel values in the effective region

$$A_{\rm eff} = \sum_{i=1}^{N_x} \sum_{j=1}^{N_y} I_{\rm eff}(i, j), \tag{4.12}$$

where i runs from 1 to N_x, and j runs from 1 to N_y. This area is equivalent to the number of pixels in the effective region where $I_{\rm eff} = 1$. As a result, we evaluate the extendedness of a HSC variable in the deep difference image for a given epoch by the area of this effective region. Doing so, we could discard the effect from the noise peaks in the outskirts and quantify the extendedness of HSC variable in the difference image.

We search for lensed quasars with all the 13 epochs. Assuming we have M HSC variables, we denote $A^m_{\mathrm{eff},t}$ as the area of the effective region for a HSC variable in epoch t (table 4.3), where $m = 1, ..., M$. For each epoch t, we compute the percentile $p\%$ for the area of the effective region from all the HSC variables, $A_{\mathrm{eff},t}(p)$:

$$p\% \text{ of } M \text{ HSC variables with } A^m_{\mathrm{eff},t} < A_{\mathrm{eff},t}(p). \tag{4.13}$$

We note that, the computation of $A_{\mathrm{eff},t}(p)$ is based only on the HSC variables, independent of the mock lensed quasars. For each HSC variable m, we then count the number of epochs with the area of the effective region larger than $A_{\mathrm{eff},t}(p)$, $N^m_{\mathrm{epoch}}(p)$. For example, if a HSC variable has $A^{m'}_{\mathrm{eff},t} > A_{\mathrm{eff},t}(p_{\mathrm{thrs}})$ at a threshold of percentile $p_{\mathrm{thrs}}\%$, for $t = t_1, t_2,$ and t_3, we will say $N^{m'}_{\mathrm{epoch}}(p_{\mathrm{thrs}}) = 3$. Given a threshold of percentile $p_{\mathrm{thrs}}\%$, we set another threshold, N_{thrs}, and a HSC variable will be classified as a candidate for lensed quasar if $N^{m'}_{\mathrm{epoch}}(p_{\mathrm{thrs}}) > N_{\mathrm{thrs}}$.

We also perform the calculation in equations (4.10)-(4.12) for each injected mock lensed quasar. Figure 4.4e shows an example of injected mock lensed quasar in the same epoch as figure 4.4a. Figures 4.4f and 4.4g are respectively the 3σ-mask and the effective region of the mock lensed quasar in figure 4.4e. As shown in figures 4c and 4g, the injected mock lensed quasar has a much larger area of the effective region.

4.3.2 Preselection by “number of blobs”

In addition to the extendedness, we could also apply the "blob-feature" as a secondary criterion to improve the search method. The image residuals of variable sources in the difference image have either positive pixel values or negative pixel values, depending on the brightness change, and the pixel values elsewhere should be zero, up to the noise level. The residuals with positive pixel values are like "white blobs", and the residuals with negative pixel values are like "black blobs", as shown in figures 4a and 4e. In the difference image, these blobs are like "local extrema" in the "zero-background". Due to the multiple point-like image residuals, lensed quasars tend to have a larger number of "local extrema", compared to unlensed variable sources. Therefore, we enhance the lens search method in section 4.3.1 with a preselection of HSC variables based on a criterion on the number of "local extrema".

We first define "local extremum" for the difference image. A pixel (i, j) is a "local

extremum", if

$$I_{\rm mask}(i,j) = 1 \tag{4.14}$$

and

$$I_{\rm eff}(i,j) = 1, \tag{4.15}$$

with its neighbouring pixels (i', j') satisfying

$$I_{\rm eff}(i',j') = 1 \tag{4.16}$$

and

$$I(i,j) > I(i',j') \text{ or } I(i,j) < I(i',j'), \tag{4.17}$$

for $i' = i-1, i, i+1$ and $j' = j-1, j, j+1$, except $(i', j') = (i, j)$. The local extrema are marked by cyan in figures 4d and 4h. Figures 4d and 4h keep the pixel values only for the pixels satisfying equation (4.15), and filter out the other pixels. We note that, with the definition in equations (4.14)-(4.17), the local extrema do not completely correspond to the blobs. As shown in figure 4d, we lose the white blob in the left as a local extremum because the pixel that is supposed to be the local extremum, indicated as "edged extremum" in red, is located at the edge of the region that is effectively related to the HSC variable and thus fails the condition in equation (4.16). Furthermore, the local extrema could also come from noise peaks, as marked by magenta in figure 4h. Despite that the local extrema and the blobs are not in one-to-one correspondence, their numbers are still highly correlated.

Before we compute the percentile $A_{{\rm eff},t}(p)$ at $p\%$ in equation (4.13), we count the number of the local extrema, $N^m_{\rm extrm}$, for each HSC variable m (where $m = 1, ..., M$) in an epoch of choice. Depending on the imaging survey, this epoch could be for example the best-seeing epoch, or median-seeing epoch. In the HSC transient survey, the best-seeing epoch with a remarkable value of 0.42 arcsec is so good that the sharp images actually lead to significant artifacts in the deep difference image that affects the number of extrema. We therefore use the median-seeing epoch (with seeing of 0.72 arcsec) in the HSC transient survey for detecting the local extrema, as this is the regime where the difference imaging pipeline runs well. Given a criterion, $N_{\rm crit}$, a HSC variable will be discarded from the lens classification if $N^{m'}_{\rm extrm} \leq N_{\rm crit}$, and a HSC variable will be kept in the lens classification if $N^{m'}_{\rm extrm} > N_{\rm crit}$.

Assuming we have M' HSC variables with their number of the local extrema larger than $N_{\rm crit}$ after the preselection (where $M' \leq M$), we compute their area of the

effective region for each epoch t ($A^{m'}_{\mathrm{eff},t}$, $m' = 1, ..., M'$), and further calculate the percentile p% for the area of the effective region from these M' HSC variables, $A'_{\mathrm{eff},t}(p)$, in each epoch t, which is similar to equation (4.13). We notice that, at a same percentile p%, $A'_{\mathrm{eff},t}(p)$ is generally larger than $A_{\mathrm{eff},t}(p)$, the percentile p% from all the HSC variables before the preselection. The reason is that the HSC variables with fewer local extrema are also the HSC variables with fewer spatially extended blobs counting for the extendedness, so when we reject the HSC variables with small number of the local extrema, we also reject the HSC variables that are small in the area of the effective region. Raising $A_{\mathrm{eff},t}(p)$, the percentile p% for the area of the effective region, with the preselection by the number of blobs makes the further lens classification more efficient and helps us to avoid large number of false candidates for lensed quasar, though we would lose a few candidates, particularly narrowly separated lensed quasars (section 4.4.2). We illustrate our lensed quasar candidate selection procedure (section 4.3.1 and section 4.3.2) in figure 4.5.

4.4 Performance test

In this section, we examine the performance of our lens search algorithm. To test the performance of the lens search algorithm, we need not only the deep difference images of lensed quasars, but also the deep difference images of the non-lensed objects. We exploit 12,910 HSC variables from the HSC transient survey as the non-lensed objects to test our lens search algorithm. Based on the estimation of lensed quasar population in OM10, we expect that at most 1-2 quad(s) lie in the HSC transient survey according to the survey depth and the covering area. The 12,910 HSC variables we use to test our lens search algorithm come from a ∼0.64 deg^2 sub-sky-area in the HSC transient survey (1.77 deg^2), so all of them are likely to be false positives. Like the 2,033 injected mock lensed quasars, we take the deep difference images from all the 13 epochs for each HSC variable.

4.4.1 Classification based only on spatial extent

The lens search algorithm performance is measured by the true-positive rate (TPR) and the false-positive rate (FPR), which are defined as

$$\mathrm{TPR} = \frac{N_{\mathrm{TP}}}{N_{\mathrm{P}}} \tag{4.18}$$

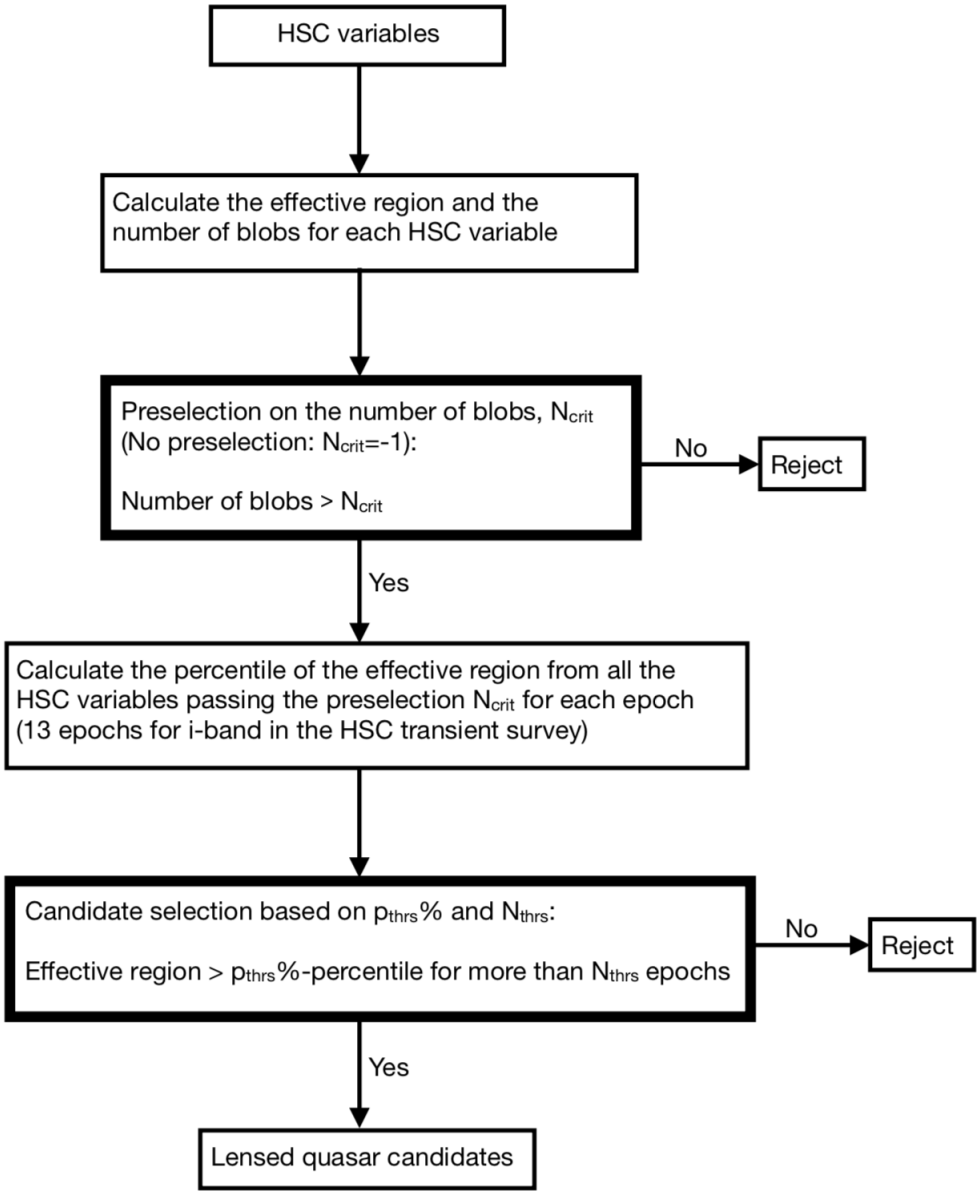

Figure 4.5: Flowchart illustrating the lensed quasar candidate selection procedure. We first calculate the effective region (equations (4.10)-(4.12)) and the number of blobs (equations (4.14)-(4.17)) for each variable object from the HSC transient survey (HSC variable). We preselect the HSC variables with the number of blobs larger than $N_{\rm crit}$. We then calculate the percentile of the effective region for each epoch from all the HSC variables that are remained after the preselection on the number of blobs. Finally, we set two thresholds, $p_{\rm thrs}$% and $N_{\rm thrs}$, and selecting the HSC variables that have effective region larger than $p_{\rm thrs}$%-percentile for more than $N_{\rm thrs}$ epochs, as lensed quasar candidates.

and

$$\mathrm{FPR} = \frac{N_{\mathrm{FP}}}{N_{\mathrm{N}}}, \tag{4.19}$$

where N_{TP} is the number of correctly identified positive cases, N_{P} is the number of total positive cases, N_{FP} is the number of falsely identified negative cases, and N_{N} is the number of total negative cases. Here, the positive cases are the quasar lenses, and the negative cases are the non-lensed objects, which are the HSC variables from the HSC transient survey.

We split the injected mock lensed quasars into four subgroups according to their brightness and quasar-image separation, and test the performance of the lens search algorithm individually for each subgroup. In this work, a lensed quasar is bright if the magnitude of the third brightest image $m_{3\mathrm{rd}} < 22.0$ mag, otherwise this lensed quasar is faint ($22.0\ \mathrm{mag} \leq m_{3\mathrm{rd}} < 24.0\ \mathrm{mag}$); a lensed quasar has wide separation if the largest separation among the pairs of the lensed images $\theta_{\mathrm{LP}} > 1.5''$, otherwise this lensed quasar has narrow separation ($0.5'' < \theta_{\mathrm{LP}} \leq 1.5''$). Therefore, the four subgroups are bright lensed quasars with wide separation, bright lensed quasars with narrow separation, faint lensed quasars with wide separation, and faint lensed quasars with narrow separation.

For each subgroup, N_{P} is the total number of lensed quasars in the subgroup, and N_{TP} is the number of lensed quasars in the subgroup that are classified as lens candidates by the lens search algorithm. For example, in the "bright-wide" group, N_{P} is the total number of bright lensed quasars with wide separation, and N_{TP} is the number of the bright lensed quasars with wide separation that are classified as lens candidates by the lens search algorithm. For all the four subgroups, N_{N} is the total number of the HSC variables that we use to test the lens search algorithm ($N_{\mathrm{N}} = 12910$ in this paper), and N_{FP} is the number of the HSC variables that are falsely classified as the lens candidates by the lens search algorithm. N_{N} and N_{FP} only comprise of the HSC variables and they do not correspond to any specific subgroup.

Figure 4.6 shows the receiver operating characteristic (ROC) curves, TPR against FPR, for the four subgroups. The ROC curves quantitatively shows the lens search performance, and the best lens search performance would give points in the top-left corner, indicating high TPRs and low FPRs. We could further quantify the lens search performance using the minimum distance between the top-left corner

	Bright-wide		Bright-narrow		Faint-wide		Faint-narrow	
$p_{\rm thrs}$	TPR	FPR	TPR	FPR	TPR	FPR	TPR	FPR
90%	0.990	0.060	0.949	0.060	0.741	0.060	0.608	0.060
95%	0.901	0.023	0.840	0.023	0.563	0.023	0.335	0.023
97.5%	0.632	0.012	0.510	0.012	0.288	0.012	0.165	0.012
d	0.053		0.078		0.170		0.182	

Table 4.5: TPRs, FPRs, and d (the minimum distance between the ROC curves and the top-left corner) of our lens search algorithm at $N_{\rm thrs} = 9$.

Observation date	$A_{\rm eff}(p_{\rm thrs})$		
	$p_{\rm thrs} = 90\%$	$p_{\rm thrs} = 95\%$	$p_{\rm thrs} = 97.5\%$
2016-11-25	78	119	178
2016-11-29	94	163	270
2016-12-25	140	314	708
2017-01-02	114	170	306
2017-01-23	113	163	247
2017-01-30	84	124	179
2017-02-02	105	152	203
2017-02-25	71	104	142
2017-03-04	123	170	241
2017-03-23	71	102	142
2017-03-30	123	194	398
2017-04-26	136	276	679
2017-04-27	77	106	142

Table 4.6: Numbers of pixels for $A_{\rm eff}(p_{\rm thrs})$ at $p_{\rm thrs}\% = 90\%, 95\%$, and 97.5% among the 12910 HSC variables we use to test the lens search algorithm.

((TPR, FPR) = (100%, 0%)) and the ROC curve, d. The smaller the value of d is, the better the performance of the lens search algorithm is. The result in figure 4.6 is from the method in section 4.3.1, by varying $p_{\rm thrs}\%$ at $N_{\rm thrs} = 9$.[5] Increasing the value of $p_{\rm thrs}\%$ from 5% to 99.5% gives points along the ROC curves from the top-middle to the bottom-left corner. Diamonds, triangles, and circles in figure 4.6 mark TPRs and FPRs respectively at $p_{\rm thrs}\% = 90\%, 95\%,$ and 97.5%, for each subgroup of the injected mock lensed quasars. We list the values of TPRs, FPRs and d in Table 4.5, and the numbers of pixels for $A_{\rm eff}(p_{\rm thrs})$ at $p_{\rm thrs}\% = 90\%, 95\%,$ and 97.5% in table 4.6.

We further explore the performance of our lens search algorithm in each subgroup

[5] We have tested our lens search algorithm for $N_{\rm thrs} = 0, 1, 2, ..., 12$, and we have the optimal ROC curve when $N_{\rm thrs} = 9$ (i.e., smallest value of d).

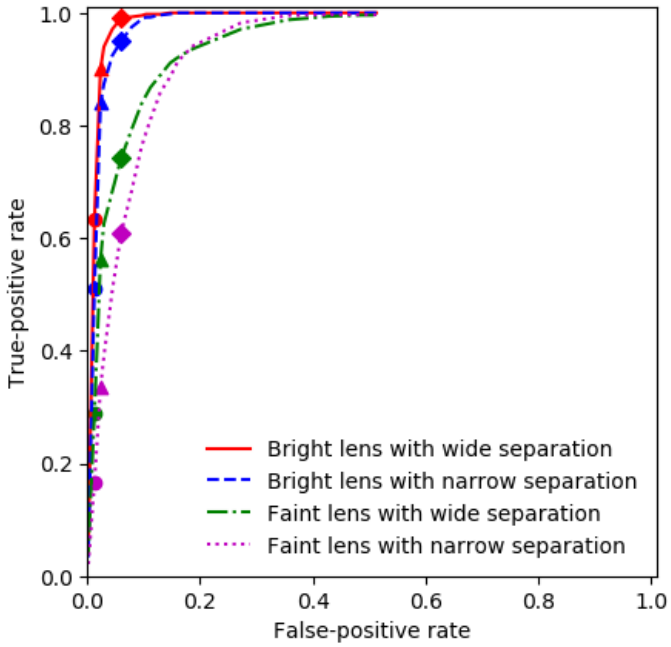

Figure 4.6: ROC curves of the lens search method based only on spatial extent. A lens is considered to be *bright* if its third brightest image has $m_{3\mathrm{rd}} < 22.0$ mag, and *faint* if $22.0\ \mathrm{mag} \leq m_{3\mathrm{rd}} < 24.0$ mag; a lens is considered to have wide separation if the largest separation among the pairs $\theta_{\mathrm{LP}} > 1.5''$, and narrow separation if $0.5'' < \theta_{\mathrm{LP}} \leq 1.5''$. The ROC curves are plotted by varying $p_{\mathrm{thrs}}\%$ from 5% to 99.5% at $N_{\mathrm{thrs}} = 9$ (see Section 4.4.1 for details). The diamonds, triangles, and circles are the points on the ROC curves when $p_{\mathrm{thrs}}\% = 90\%, 95\%$, and 97.5%, respectively. For the bright lensed quasars with wide separation, our lens search algorithm could detect them with $(\mathrm{TPR}, \mathrm{FPR}) = (90.1\%, 2.3\%)$. The lens search performance for the bright lensed quasars with narrow separation is similar to the bright lensed quasars with wide separation.

when $N_{\mathrm{thrs}} = 9$. For the bright lensed quasars with wide separation, our lens search algorithm could identify them with a TPR = 90.1% and a FPR = 2.3%, at $p_{\mathrm{thrs}}\% = 95\%$. Although the ROC curve for the bright lensed quasars with narrow separation is slightly lower, our lens search algorithm could still capture these lensed quasars with a TPR = 84.0% at the same FPR (= 2.3%), when $p_{\mathrm{thrs}}\% = 95\%$. This indicates that our lens search algorithm with the method in section 4.3.1 is sensitive to the bright lensed quasars regardless of the separation. Given the much lower ROC curves, the faint lensed quasars are mainly more difficult to detect by our lens search algorithm. For the faint lensed quasars with wide separation, the TPR hugely drops to 56.3% at $p_{\mathrm{thrs}}\% = 95\%$, while the nearest point to the top-left corner on the ROC curve is $(\mathrm{TPR}, \mathrm{FPR}) = (89.0\%, 13.0\%)$ at $p_{\mathrm{thrs}}\% = 82\%$. The false positives

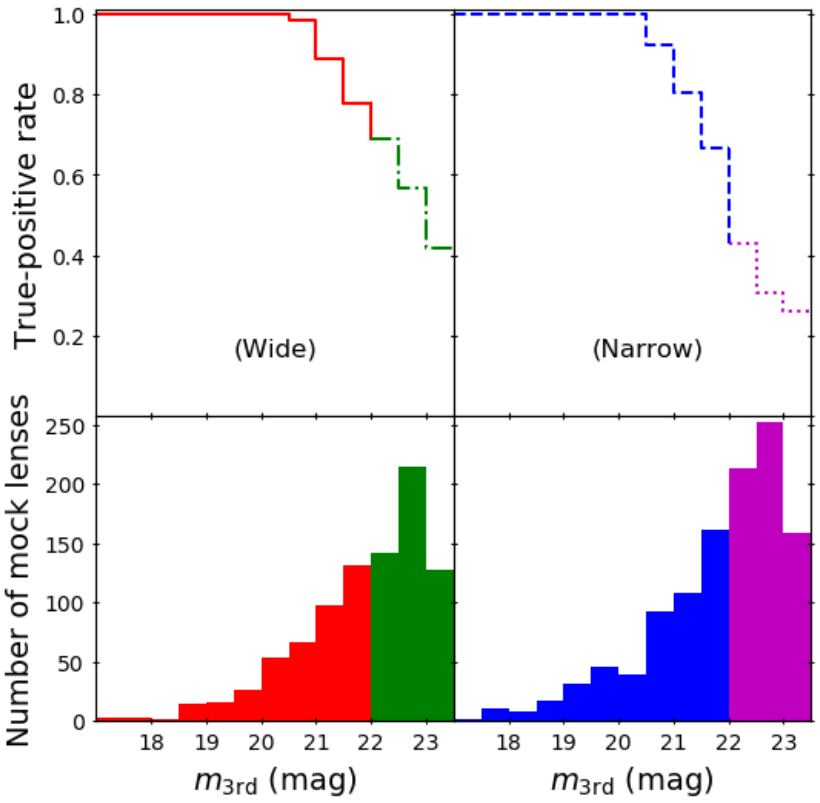

Figure 4.7: Sensitivity to the quasar image brightness m_{3rd} of the lens search method based only on spatial extent. Wide: the group of lensed quasars with the largest separation among the pairs $\theta_{LP} > 1.5''$. Narrow: the group of lensed quasars with $0.5'' < \theta_{LP} \leq 1.5''$. The top panels show the TPRs of each m_{3rd} bin, when $p_{thrs}\% = 95\%$ and $N_{thrs} = 9$. The bottom panels show the number of mock lenses in each m_{3rd} bin. Our lens search algorithm could identify more than 90% of the lensed quasars with $m_{3rd} < 21.0$ mag.

that our lens search method will possibly detect are very bright objects, such as very bright galaxy or very bright variable star. Those objects are so bright that the transient data pipeline might not be able to perform the image subtraction properly, and their difference images might not represent the correct brightness change.

We examine our lens search algorithm's sensitivity to m_{3rd} with $p_{thrs}\% = 95\%$ and $N_{thrs} = 9$ in figure 4.7. The top panels in figure 4.7 show the TPRs, and the bottom panels show the number of mock lenses in each m_{3rd} bin. Our lens search algorithm could detect all the lensed quasars with the third brightest image brighter than 20.5 mag ($m_{3rd} < 20.5$ mag), and the TPRs for the lensed quasars with $m_{3rd} < 21.0$ mag are larger than or equal to 90%. We show again that our lens search algorithm with

the method from section 4.3.1 has similar sensitivity to the bright lensed quasars with both wide and narrow separation; the reason is that, most of the HSC variables are unlensed sources and have small areas of the effective region, resulting in small values for the percentile of $p_{\rm thrs}$%, so a bright lensed quasar typically has an area of the effective region larger than the percentile of $p_{\rm thrs}$% and would be identified as a lens candidate regardless of its separation. The TPRs gradually drop when $m_{\rm 3rd} \geq 21.0$ mag. The reason our lens search algorithm has poorer performance on the faint lensed quasars is that, the difference images of the faint lensed quasars have fewer pixels with values larger than 3σ (equation (4.10)), as the brightness change of quasar is generally small, so the area of the effective region in each epoch, $A^m_{{\rm eff},t}$ (equations (4.12) and (4.13), see section 4.3.1 for more detail), is also small even for the lenses with wide separation, which makes the faint lensed quasars unable to pass the given thresholds, $p_{\rm thrs}$% and $N_{\rm thrs}$.

4.4.2 Classification using both spatial extent and number of blobs

Now we explore the lens search performance with the preselection based on the number of blobs. We test how the ROC curves change with the criterion number of local extrema, $N_{\rm crit}$ (see section 4.3.2 for details). In figure 4.8, we plot the ROC curves by varying $p_{\rm thrs}$% for $N_{\rm crit} = 2$. As shown in figure 4.8, after the preselection is applied ($N_{\rm crit} = 2$), our lens search algorithm could capture the bright lensed quasars with wide separation at (TPR, FPR) = (97.6%, 2.6%) with thresholds, $p_{\rm thrs}$% = 55% and $N_{\rm thrs} = 4$.[6] Comparing to the lens search performance without the preselection by the number of blobs ($N_{\rm crit} = 0$), the lens search algorithm applying the preselection ($N_{\rm crit} > 0$) could have similar performance with much looser constraints on $p_{\rm thrs}$% and $N_{\rm thrs}$. Crosses, triangles, and circles in figure 4.8 represent TPRs and FPRs at $p_{\rm thrs}$% = 0%, 55%, and 75%, respectively. With the preselection by number of blobs, the ROC curves start from a much lower FPR, compared to the ROC curves without the preselection ($N_{\rm crit} = 0$). Actually, the crosses in figure 4.8 indicate that when $N_{\rm crit} = 2$, we have a much lower FPR (∼5%) at $N_{\rm thrs} = 4$, even when there is no constraint from $p_{\rm thrs}$%. We list the values of TPRs, FPRs, and d (the minimum distance between the ROC curves and the top-left corner) from the lens search performance with the preselection by the number of blobs in table 4.7. The numbers of pixels for $A_{\rm eff}(p_{\rm thrs})$ at $p_{\rm thrs}$% = 55% and 75% after the preselection are

[6] When the preselection $N_{\rm crit} = 2$ is applied, we have the optimization of the ROC curves at $N_{\rm thrs} = 4$.

listed in table 4.8.

We further look into each subgroup of lensed quasars for the comparison of the performance between the two conditions, with and without the preselection by number of blobs ($N_{\rm crit} > 0$ and $N_{\rm crit} = 0$). At small values of $p_{\rm thrs}$%, the TPRs are ∼100% for all the four subgroups when $N_{\rm crit} = 0$, while the TPRs for the four subgroups all drop when $N_{\rm crit} = 2$. This indicates that, although the preselection based on number of blobs hugely decreases the FPRs, the preselection also discards a part of the candidates for lensed quasars. The TPR decreases by ∼2.2% for the bright lensed quasars with wide separation, by ∼25.1% for the bright lensed quasars with narrow separation, and by ∼13.9% for the faint lensed quasars with wide separation. We notice that, unlike figure 4.6, where the ROC curve of the bright lensed quasars with narrow separation is higher than the ROC curve of the faint lensed quasars with wide separation, when $N_{\rm crit} = 2$, the ROC curve of the faint lensed quasars with wide separation becomes higher than the ROC curve of the bright lensed quasars with narrow separation (at FPR $\gtrsim$0.02), which implies the blob-based preselection has a more significant impact on the lensed quasars with narrow separation.

To investigate the influence of the preselection, we examine the sensitivity to $\theta_{\rm LP}$ of the lens search algorithm setting $p_{\rm thrs}$% = 0%, at $N_{\rm thrs} = 4$, with a preselection $N_{\rm crit} = 2$. By setting $p_{\rm thrs}$% = 0%, we could study the impact from the preselection more clearly. Figure 4.9 shows that, when there is no constraint from $p_{\rm thrs}$, our lens search algorithm with the preselection by number of blobs could detect the lensed quasars with $\theta_{\rm LP} > 1.5''$ at relatively stable TPRs (> 80%), and there is a great drop in TPRs when $\theta_{\rm LP}$ becomes smaller than $1.0''$. The lensed quasars with narrow separation become even harder to capture when the preselection is applied, and the reason is that, as lensed images with narrow separation are blended together, the number of blobs decreases, making the lensed quasars with narrow separation difficult to meet the given criterion, $N_{\rm crit}$. We show the ROC curves for the bright lensed quasars with wide separation at different values of $N_{\rm crit}$ (when $N_{\rm thrs} = 4$) in figure 4.10, zoomed-in with the x-axis spanning from 0 to 0.05. Crosses and triangles in figure 4.10 represent $p_{\rm thrs}$% = 0% and 55% respectively. As $N_{\rm crit}$ increases, the ROC curve drops and slightly shifts to the left. Both the TPRs and the FPRs decrease when we raise $N_{\rm crit}$. However, FPR decreases faster than TPR at low values of $N_{\rm crit}$. In particular, we could decrease the FPR by a factor ∼2 and have a more

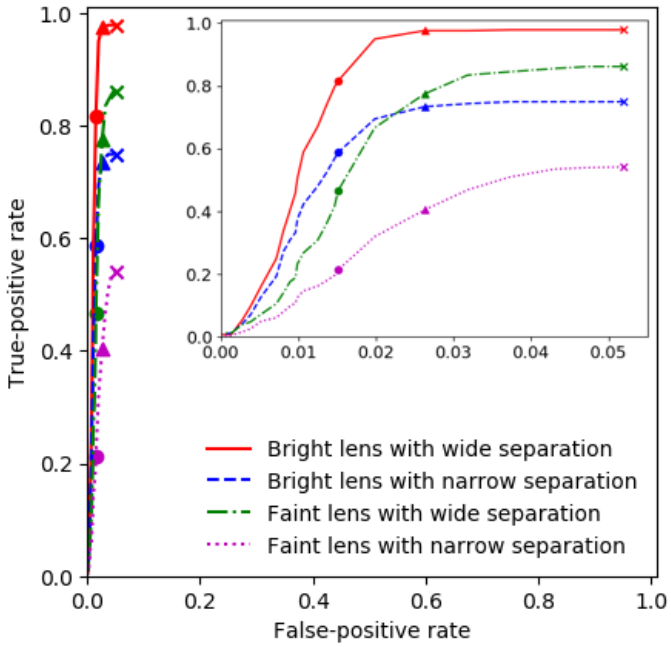

Figure 4.8: ROC curves of the lens search method using both spatial extent and the number of blobs. The subgroups of lensed quasars are the same as the subgroups in figure 4.6. The ROC curves are plotted by varying $p_{\rm thrs}$% from 0% to 99.5% at $N_{\rm thrs}$ = 4 with the preselection on the number of blobs $N_{\rm crit}$ = 2. The crosses, triangles, and circles are the points on the ROC curves when $p_{\rm thrs}$% = 0%, 55%, and 75%, respectively. With the preselection $N_{\rm crit}$ = 2, our lens search algorithm could identify the bright lensed quasars with wide separation at (TPR, FPR) = (97.6%, 2.6%), which is similar to the lens search performance when no preselection is performed. The ROC curves also start from a much lower FPR (crosses) with the preselection $N_{\rm crit}$ = 2. The ROC curves are zoomed-in with the FPR (x-axis) spanning from 0 to 0.05 in the small panel.

efficient lens search when we raise $N_{\rm crit}$ from 2 to 3, at the expense of lowering TPR by only ~5%. Raising $N_{\rm crit}$ beyond 3 would start to lead to more decrease in TPR compared to FPR, and not as advantageous.

4.4.3 Classification based on one single epoch

It is ideal and the most efficient to detect lensed quasars through only one epoch (in addition to the reference image). If the lens search algorithm is able to identify the candidates for lensed quasars in a single epoch of an ongoing cadenced survey, possible spectroscopic follow-up could be conducted immediately for the confirmation and the lens model, and a further monitoring observation for measuring the time delays could start right away. Here, we study the performance of our lens search

	Bright-wide		Bright-narrow		Faint-wide		Faint-narrow	
$p_{\rm thrs}$%	TPR	FPR	TPR	FPR	TPR	FPR	TPR	FPR
0%	0.978	0.052	0.749	0.052	0.861	0.052	0.541	0.052
55%	0.976	0.026	0.733	0.026	0.774	0.026	0.404	0.026
75%	0.816	0.015	0.588	0.015	0.466	0.015	0.213	0.015
d	0.036		0.254		0.147		0.462	

Table 4.7: The values of TPRs, FPRs, and d (the minimum distance between the ROC curves and the top-left corner) at $N_{\rm thrs} = 4$, when the preselection based on the number of blobs, $N_{\rm crit} = 2$, is applied.

Observation date	$A_{\rm eff}(p_{\rm thrs})$	
	$p_{\rm thrs} = 55\%$	$p_{\rm thrs} = 75\%$
2016-11-25	113	223
2016-11-29	132	292
2016-12-25	167	553
2017-01-02	154	303
2017-01-23	160	283
2017-01-30	120	208
2017-02-02	127	184
2017-02-25	124	208
2017-03-04	157	282
2017-03-23	97	153
2017-03-30	156	400
2017-04-26	151	568
2017-04-27	99	161

Table 4.8: Numbers of pixels for $A_{\rm eff}(p_{\rm thrs})$ at $p_{\rm thrs}\% = 55\%$, and 75% after applying the preselection on the number of blobs, $N_{\rm crit} = 2$.

algorithm to capture lensed quasars in one single epoch.

If only one epoch is available, our lens search algorithm will employ only $p_{\rm thrs}$. Since the seeing of a single epoch might not be suitable for counting the local extrema, we do not apply the preselection using number of blobs. For one single epoch t', our lens search algorithm will classify a HSC variable m' as a candidate for lensed quasar if

$$A^{m'}_{{\rm eff},t'} > A_{{\rm eff},t'}(p_{\rm thrs}), \tag{4.20}$$

where $A^{m'}_{{\rm eff},t'}$ is the area of the effective region in epoch t' for the HSC variable m', and $A_{{\rm eff},t'}(p_{\rm thrs})$ is the percentile $p_{\rm thrs}$% for the area of the effective region from all the HSC variables in epoch t'. We test the lens search performance in each epoch

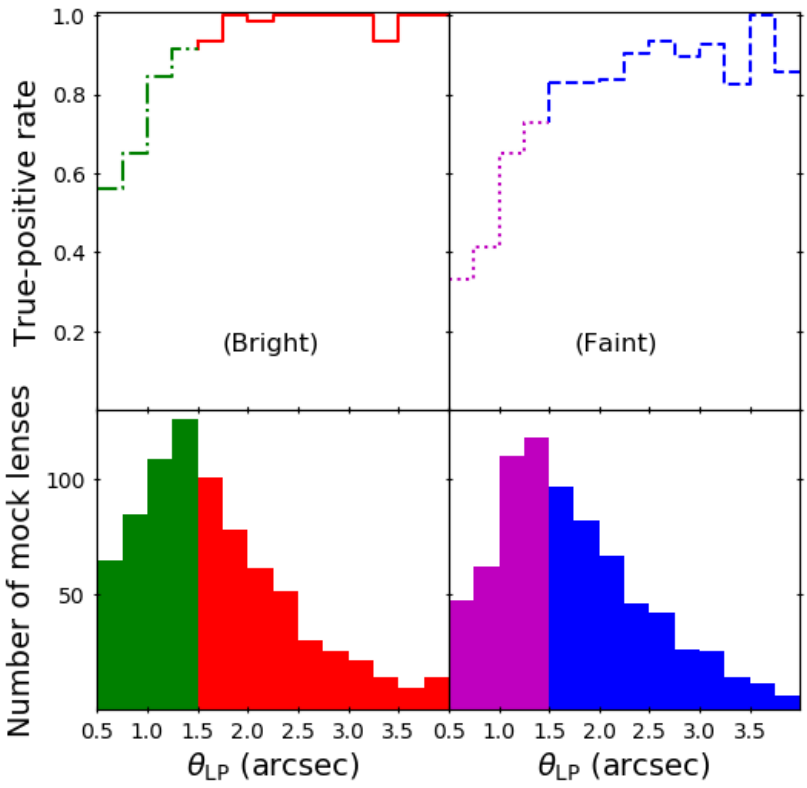

Figure 4.9: Sensitivity to the quasar image separation $\theta_{\rm LP}$ of the lens search method using both spatial extent and the number of blobs. Bright: the group of lensed quasars with the third brightest image brightness $m_{\rm 3rd} < 22.0$ mag. Faint: the group of lensed quasars with 22.0 mag $\leq m_{\rm 3rd} < 24.0$ mag. The top panels show the TPRs of each $\theta_{\rm LP}$ bin, when $p_{\rm thrs}\% = 0\%$ and $N_{\rm thrs} = 4$, with the preselection by the number of blobs $N_{\rm crit} = 2$. The bottom panels show the number of mock lenses in each $\theta_{\rm LP}$ bin.

from the HSC transient survey, and show the ROC curves with varied values of $p_{\rm thrs}\%$ from three epochs with different seeings in figure 4.11. The result in the left panel of figure 4.11 is from the epoch with the best lens search performance among the 13 epochs, where the nearest point to the top-left corner on the ROC curve for the bright lensed quasars with wide separation is $(\mathrm{TPR}, \mathrm{FPR}) = (97.6\%, 2.4\%)$ at $p_{\rm thrs}\% = 97.5\%$, which is similar to the performance when all the 13 epochs is used. The middle panel of figure 4.11 shows the average case of the lens search performance we have in one single epoch, with the nearest point to the top-left corner on the ROC curves, $(\mathrm{TPR}, \mathrm{FPR}) = (94.2\%, 5.0\%)$ at $p_{\rm thrs}\% = 95.0\%$. In the right panel of figure 4.11 is the worst performance we have among the 13 epochs.

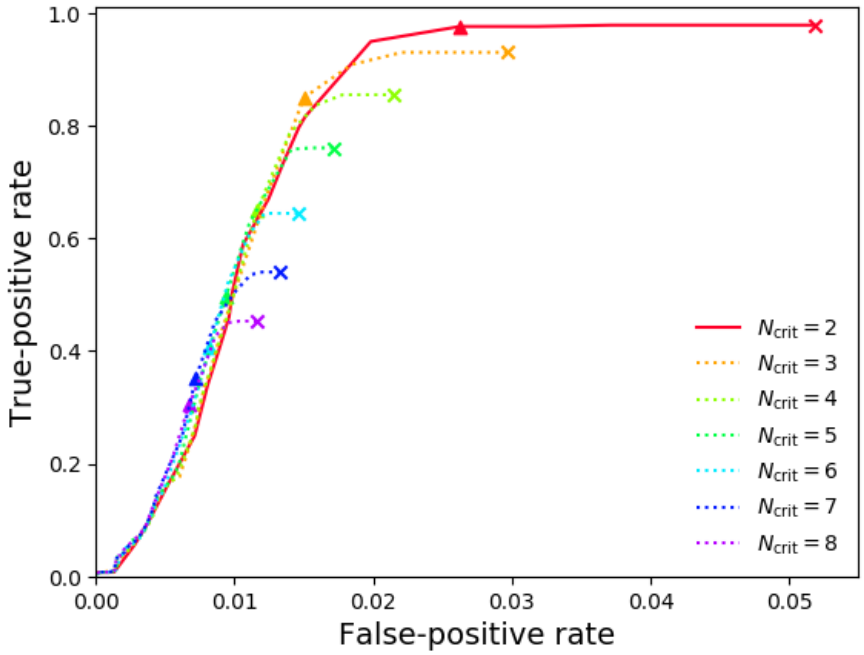

Figure 4.10: ROC curves for the bright lensed quasars ($m_{3rd} < 22.0$ mag) with wide separation ($\theta_{LP} > 1.5''$) of the lens search method with the preselection on the number of blobs at different N_{crit} values.

We further investigate the relation between the lens search performance and the seeing in one single epoch. For each epoch t, we define the distance d_t as the distance between (TPR, FPR) = (100%, 0%) and the nearest point on the ROC curve of the bright lensed quasars with wide separation. The smaller d_t is, the better the lens search performance is. We plot d_t against the seeing for each epoch t in figure 4.12. d_t becomes small when seeing is around 0.7 arcsec, indicating that our lens search algorithm would have good performance when the single epoch has seeing around 0.7 arcsec. In figure 4.12, we also see that d_t suddenly increases when seeing is better than 0.5 arcsec, which verifies that when the seeing is too good, our lens search performance will be heavily affected by the significant artifacts from the sharp images.

4.5 Summary

In this chapter, we present a comprehensive simulation pipeline of time-varied lensed images and develop a new algorithm for searching lensed quasars through their time variability. The simulation pipeline constructed in section 4.1 is useful not only for lensed quasar search, but also for other studies, such as studying lensed

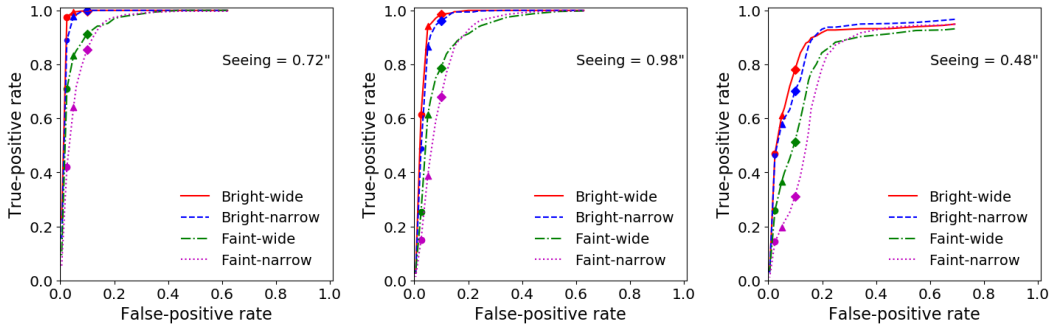

Figure 4.11: Lens search performance based on a single epoch. We test our lens search algorithm using difference images from only one single epoch for all the 13 epochs in the HSC transient survey, and show the ROC curves of the epochs with the best performance (left), the average performance (middle), and the worst performance (right). For lens search algorithm based on a single epoch, we only use $p_{\rm thrs}$ as constraint. In each panel, the ROC curves are plotted by varying $p_{\rm thrs}$%, and the diamonds, triangles, and circles are the points on the ROC curves at $p_{\rm thrs}\% = 90\%, 95\%,$ and 97.5%. The seeing of each epoch is also indicated in each panel. Our lens search algorithm has the best performance in the single epoch with a seeing of $0.72''$, capturing the bright lensed quasars with wide separation at $(\mathrm{TPR}, \mathrm{FPR}) = (97.6\%, 2.4\%)$ when $p_{\rm thrs}\% = 97.5\%$. In a single epoch with average seeing ($\sim 0.98''$), our lens search algorithm could detect the bright lensed quasars with wide separation at $(\mathrm{TPR}, \mathrm{FPR}) = (94.2\%, 5.0\%)$ when $p_{\rm thrs}\% = 95.0\%$. The worst lens search performance happens in the epoch with an exceptional seeing value of $0.48''$ due to artifacts appearing in the difference image pipeline when the seeing is "too" good.

supernovae and testing lens mass modelling. Our lens search method builds upon the one first proposed by Kochanek et al. (2006a), and provides a practical way of selecting lensed quasar candidates through their difference images. We summarize the main results as follows:

– Our simulation pipeline generates images of lensed quasar accounting for the quasar variability, quasar host, lens galaxy, and the PSF variation. The application of the simulation pipeline to the HSC transient survey yields HSC-like difference images of the mock lensed quasars.

– The lens search algorithm we develop in this work quantifies spatial extent of the variable objects in difference images, and further selects the variable objects with large spatial extent as lensed quasar candidates. The test on a sample containing mock lensed quasars and HSC variables shows that our lens search algorithm could identify the bright lensed quasars with wide separation

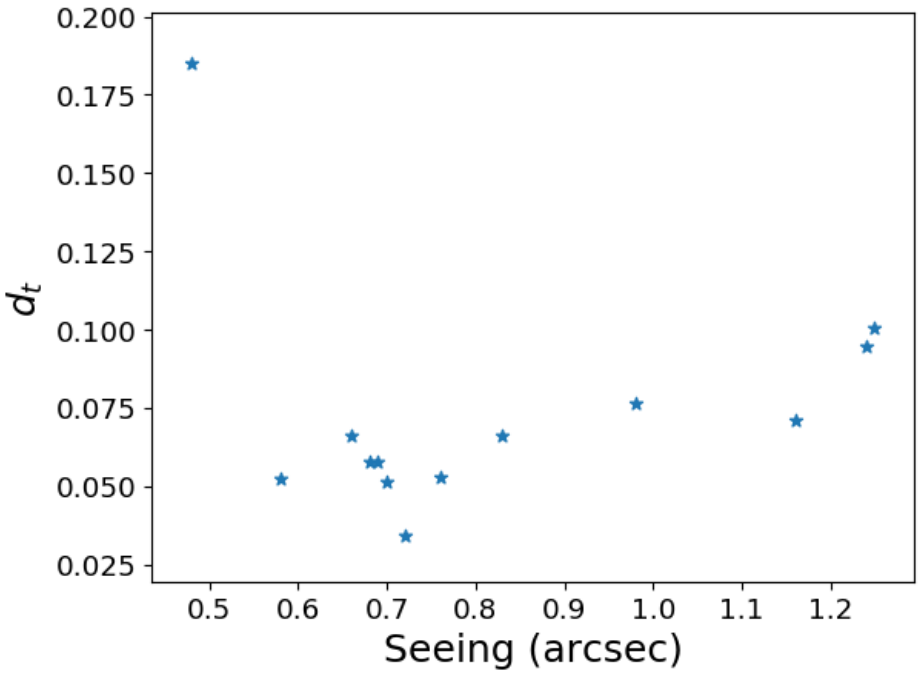

Figure 4.12: The relation between the lens search performance and the seeing in each single epoch from the HSC transient survey. d_t is defined as the minimum distance between (TPR, FPR) = (100%, 0%) and the ROC curve of the bright lensed quasars ($m_{3\mathrm{rd}} < 22.0$ mag) with wide separation ($\theta_{\mathrm{LP}} > 1.5''$) for each epoch t. The smaller d_t is, the better the lens search performance is. The 13 star symbols indicate the d_t values for the 13 epochs, plotted against their corresponding seeing. Our lens search algorithm performs well when the single epoch has seeing ~0.7″. The low lens search performance in the epoch with extraordinary seeing (< 0.5″) is due to the significant artifacts in the difference image from the sharp image.

($m_{3\mathrm{rd}} < 22.0$ mag and $\theta_{\mathrm{LP}} > 1.5''$) at a high TPR (90.1%) and a low FPR (2.3%).

– With a preselection on number of blobs, our lens search algorithm could achieve an even higher TPR (97.6%) without a significant change in FPR (2.6%) for the bright lensed quasars with wide separation. The preselection is more sensitive to the lensed quasars with wide separation.

– Although our lens search algorithm mainly uses difference images from multiple epochs, it also works with only one single epoch. The lens search performance in one single epoch depends on the seeing. When the seeing is around 0.7 arcsec, we have the best lens search performance, (TPR, FPR) = (97.6%, 2.4%) for the bright lensed quasars with wide separation. If the seeing

is substantially better or worse than 0.7 arcsec, our lens search performance become poorer.

Our lens search algorithm will be even more powerful when combined with other lens search techniques. While our lens search algorithm achieves a high TPR and a low FPR, the number of the input "variables" (e.g. the HSC variables in this work) are typically huge, and thus the absolute number of false-positive lens candidates are also large even with FPR of $1 - 2\%$, making further confirmation inaccessible. Although the lens search techniques in previous works use static approaches without any information from quasar variability, their exploration in catalogues and image configuration of lensed quasar are helpful for making our lens search algorithm more efficient. As will be shown in chapter 5, we use CHITAH (Chan et al., 2015), a lens search method based on image configuration, as an advanced selection after our time-variability-based method. We will apply the variability-based lens search algorithm developed in this chapter to the real observational variable objects in the HSC transient survey in chapter 5,

Chapter 5

STRONGLY LENSED CANDIDATES FROM THE HSC TRANSIENT SURVEY

In this chapter, we conduct a lensed quasar search within the HSC transient survey by applying the time-variability-based lens search method in chapter 4, which is built on the the concept of Kochanek et al. (2006a). The final candidates of lensed quasars here undergo a three-step process: (1) time-variability-based selection (chapter 4) according to their spatial extent in the difference images of the HSC transient survey, (2) classification as potential lenses by CHITAH (Chan et al., 2015), a lens search algorithm examining the image configuration through lens modelling, (3) visual inspection. The materials of this chapter will be submitted to a journal for publication.

The organization of this chapter is as follows. In section 5.1, we introduce the data from the HSC transient survey used in this chapter. We describe our lens selection method in section 5.2. Section 5.3 shows the lens selection results, followed by a summary in section 5.4.

5.1 Data

As described in chapter 3, the HSC transient survey has observed the COSMOS field as part of the HSC-SSP from November 2016 to June 2017, covering 1.77 $\deg^2$ in the Ultra-Deep layer with a pixel size of 0.168″. The median depths per epoch are 26.4, 26.3, 26.0, 25.6, and 24.6 mag in *g*-, *r*-, *i*-, *z*-, and *y* bands, respectively. For the difference imaging, the HSC transient survey uses the methods in Alard and Lupton (1998) and Alard (2000).

Before we proceed to the lens search with the difference images, we first select "HSC variables" from the HSC transient survey. A "HSC variable" is defined by chapter 4 as an object that is detected on the difference images at least twice in the HSC transient survey - the detections could be from two different epochs or two different bands. Following chapter 4, we focus on the HSC variables that have photometry in *i*-band, as the simulation and lens search algorithm have been developed with *i*-band in chapter 4. The number of HSC variables with *i*-band photometry is 101,353.

5.2 Selection method

We select lensed quasars with three steps. We first perform the time-variability-based selection among 101,353 HSC variables (section 5.1) with their *i*-band difference images, which is described in section 5.2.1. After the variability-based selection, we run CHITAH (Chan et al., 2015), a lens search method based on the image configuration that is described in section 5.2.2. In the end, we visually inspect the remaining HSC variables and grade them according to the grading system described in section 5.2.3. The HSC variables with highest scores are our final lensed quasar candidates. We focus only on four-image (quad) lensed quasars in this chapter.

5.2.1 Time-variability-based selection

The time-variability-based lens search method in chapter 4 quantifies the spatial extendedness of HSC variables on the *i*-band difference images, and select the HSC variables with large spatial extendedness as lensed quasar candidates. We briefly review the procedures in the following:

1. Create the "3σ-mask" for each HSC variable m in each epoch t by defining

$$I^m_{\mathrm{mask},t}(i,j) = \begin{cases} 1, & \text{if } |I^m_t(i,j)| > 3\sigma^m_t(i,j) \\ 0, & \text{otherwise} \end{cases} \tag{5.1}$$

   where $i = 1, ..., N_x$ and $j = 1, ..., N_y$ are the pixel indices in the difference image cutout $I^m_t(i,j)$ of dimensions $N_x \times N_y$,[1] $\sigma^m_t(i,j)$ are the estimated 1-σ uncertainties in the difference image cutout, and $I^m_{\mathrm{mask},t}(i,j)$ are the pixel values in the 3σ-mask.

2. Define the "effective region", $I^m_{\mathrm{eff},t}(i,j)$, and the area of effective region, $A^m_{\mathrm{eff},t}$, for each HSC variable m in each epoch t by

$$I^m_{\mathrm{eff},t}(i,j) = \begin{cases} 1, & \text{if } \sum_{i'=i-1}^{i+1} \sum_{j'=j-1}^{j+1} I^m_{\mathrm{mask},t}(i',j') > 2 \\ 0, & \text{otherwise} \end{cases} \tag{5.2}$$

   and

$$A^m_{\mathrm{eff},t} = \sum_{i=1}^{N_x} \sum_{j=1}^{N_y} I^m_{\mathrm{eff},t}(i,j). \tag{5.3}$$

[1] In this work, we use cutouts at $10'' \times 10''$ ($N_x = N_y = 59$) in the time-variability-based selection.

Observation date	Seeing (arcsec)
2016-11-25	0.83
2016-11-29	1.16
2016-12-25	1.25
2017-01-02	0.68
2017-01-23	0.70
2017-01-30	0.76
2017-02-02	0.48
2017-02-25	0.72
2017-03-04	0.69
2017-03-23	0.66
2017-03-30	0.98
2017-04-26	1.24
2017-04-27	0.58

Table 5.1: The HSC transient survey observation dates and seeing in *i*-band.

where $A^m_{\mathrm{eff},t}$ is equivalent to the number of pixels with pixel values equal to one in the effective region ($I^m_{\mathrm{eff},t} = 1$).

After we measure the spatial extendedness based on $A^m_{\mathrm{eff},t}$ for the 101,353 HSC variables with their *i*-band images in all the 13 epochs (table 5.1), we set p_{thrs}% and N_{thrs} to select lensed quasar candidates. For a given epoch t, we calculate $A_{\mathrm{eff},t}(p_{\mathrm{thrs}}\%)$, the value below which p_{thrs}% of the HSC variables have the area of effective region, $A^m_{\mathrm{eff},t}$, smaller than $A_{\mathrm{eff},t}(p_{\mathrm{thrs}}\%)$. In other words, $A_{\mathrm{eff},t}(p_{\mathrm{thrs}}\%)$ is the percentile of the effective region area that there are p_{thrs}% of the HSC variables with $A^m_{\mathrm{eff},t} < A_{\mathrm{eff},t}(p_{\mathrm{thrs}}\%)$. For the case that a HSC variable m' is not observed in an epoch t', we assign $A^{m'}_{\mathrm{eff},t'} = 0$, and we do not include it when we compute $A_{\mathrm{eff},t}(p_{\mathrm{thrs}}\%)$. The HSC variables with values of $A^m_{\mathrm{eff},t}$ larger than $A_{\mathrm{eff},t}(p_{\mathrm{thrs}}\%)$ for more than N_{thrs} epochs are identified as lensed quasar candidates.

As the first application of the lens search method in chapter 4, we employ very loose constraints, $p_{\mathrm{thrs}}\% = 50\%$ and $N_{\mathrm{thrs}} = 0$, to select lensed quasar candidates. Among the 101,353 HSC variables, there are 83,657 HSC variables identified as lensed quasar candidates by the time-variability-based selection under $(p_{\mathrm{thrs}}\%, N_{\mathrm{thrs}}) = (50\%, 0)$.

5.2.2 CHITAH

Among the 83,657 lensed quasar candidates selected in section 5.2.1, we run CHITAH on their stacked images from the HSC survey (*g*-, *r*-, *i*-, *z*-, and *y*-bands) to reduce the number of lensed quasar candidates. Briefly, CHITAH works as follows:

1. Pick two image cutouts, one from bluer bands (*g*/*r*) and one from redder bands (*z*/*y*) which have sharper point-spread functions (PSFs).
2. Match PSFs in the two selected bands.
3. Disentangle the lens light and the lensed images according to colour information.
4. Identify the lens centre and the lensed image positions, masking out the region within 0.5″ from the lens centre in the lensed arc image to prevent misidentifying the lensed image positions near the lens centre due to the imperfect lens light separation.
5. Model the configuration of the lensed images with a singular isothermal ellipsoid (SIE) model (Kormann et al., 1994) for the lens.

The outputs of the model are the best-fitting SIE parameters: the Einstein radius ($\theta_{\rm Ein}$), the axis ratio (q), the position angle (PA), and the lens centre. The convergence κ of the SIE model is given by

$$\kappa(\theta_1, \theta_2) = \frac{\theta_{\rm Ein}}{2\sqrt{\theta_1^2 + \theta_2^2/q^2}}, \tag{5.4}$$

where (θ_1, θ_2) is the coordinate of the lens relative to the lens centre along the semi-major and semi-minor axes of the elliptical mass distribution. We determine the SIE parameters by minimising the $\chi^2_{\rm src}$ on the source plane, which is defined as

$$\chi^2_{\rm src} = \sum_n \frac{|\mathbf{r}_n - \mathbf{r}_{\rm model}|^2}{\sigma^2_{\rm image}/\mu_n}, \tag{5.5}$$

where $\mathbf{r}_n$ is the respective source position mapped from the position of lensed image n by the SIE lens model, μ_n is the magnification of lensed image n from the SIE lens model, $\sigma_{\rm image}$ is chosen to be the HSC pixel size (0.168″) as an estimate of

the uncertainty, and $\mathbf{r}_{\rm model}$ is the modelled source position that is evaluated by a weighted mean of $\mathbf{r}_n$ (Oguri, 2010),

$$\mathbf{r}_{\rm model} = \frac{\sum\limits_n \sqrt{\mu_n}\mathbf{r}_n}{\sum\limits_n \sqrt{\mu_n}}. \tag{5.6}$$

Here the index n runs from one to four for quads. We also use the lens centre from the light profile as a prior to constrain the centre of the SIE model. Therefore, we define

$$\chi^2_{\rm c} = \frac{|\mathbf{x}_{\rm model} - \mathbf{x}_{\rm c}|^2}{\sigma^2_{\rm c}}, \tag{5.7}$$

where $\mathbf{x}_{\rm c}$ is the lens centre from the light profile, and $\mathbf{x}_{\rm model}$ is the lens centre from the SIE model. We choose $\sigma_{\rm c}$ to be the same as $\sigma_{\rm image}$. We further take into account the residuals of the fit to the lensed quasar image from Chitah. The difference between the lensed image $Q(i, j)$ and the predicted image $Q^{\rm P}(i, j)$ is defined as

$$\chi^2_{\rm res} = \sum_{i,j} \frac{\left[Q(i, j) - Q^{\rm P}(i, j)\right]^2}{var(i, j)}, \tag{5.8}$$

where $i = 1, ..., N_x$ and $j = 1, ..., N_y$ are the pixel indices in the image cutout of dimensions $N_x \times N_y$,[2] and $var(i, j)$ is the pixel uncertainty in $Q(i, j)$. We note that $Q^{\rm P}$ is obtained from the PSF fitting instead of the lens modelling. Therefore, the fluxes of lensed image are not affected by the flux anomalies.

The criteria for the classification of lensed quasar candidates are

$$\chi^2_{\rm src} + \chi^2_{\rm c} < 2\theta_{\rm Ein} \tag{5.9}$$

and

$$\chi^2_{\rm res} < 100, \tag{5.10}$$

where $\theta_{\rm Ein}$ is measured in arcsec. The former criterion (equation 5.9) allows Chitah to detect lensed quasar candidates that cover a wide range of $\theta_{\rm Ein}$, since (1) typically $\chi^2_{\rm src}$ scales with $\theta_{\rm Ein}$ and (2) the tests on the mock lenses in Chan et al. (2015) show that $\chi^2_{\rm src} \leq 4$ yields a low false-positive rate ($< 3\%$). The latter criterion (equation 5.10) allows us to further eliminate false positives. The lensed quasar candidates are selected within $0.3'' < \theta_{\rm Ein} < 4''$. After running Chitah, we reduce the number of the lensed quasar candidates from 83,657 to 2,130.

[2] Chitah uses cutouts at $7'' \times 7''$.

5.2.3 Visual inspection

We visually inspect the remaining 2,130 lensed quasar candidates. DCYC[3] and JHHC[4] first categorise them individually into two groups:

- Group I: objects that are clearly non-lenses,
- Group II: the other objects.

There are 65 lensed quasar candidates categorised in Group II by DCYC or JHHC. For each of these 65 lensed quasar candidates, DCYC, JHHC, and SHS[5] independently assign an integer from 0 to 3 with the following grading scheme:

- 3: definite lens,
- 2: probable lens,
- 1: likely lens,
- 0: not a lens.

Typical aspects taken into consideration in grading are the color difference between the possible lensed images and the possible lens galaxy, and the positions of the possible lensed images. This grading scheme is the same as the one on the SuGOHI lens sample from the HSC survey (e.g., Sonnenfeld et al., 2018; Chan et al., 2020; Jaelani et al., 2020). We then take the average score among the three graders for each lensed quasar candidate, and the candidates with average scores larger than 1.5 would be our final lensed quasar candidates. The seven final lensed quasar candidates are listed in table 5.2. Table 5.2 also includes one lensed galaxy candidate, which we find by serendipity.

5.3 Results and discussion

We take a further look at the HSC variables that get picked out by our approach. We describe the final candidates in section 5.3.1. In section 5.3.2, we discuss the objects selected as candidates by both the variability selection and CHITAH but rejected by

[3]Dani C.-Y. Chao
[4]James H.-H. Chan
[5]Sherry H. Suyu

Name	RA (deg)	DEC (deg)	Average score	Comment
HSCJ095921+020638	149.84071	2.11068	3.0	Anguita et al. (2009)
HSCJ100050+013251	150.20947	1.54775	2.3	No HST image
HSCJ095921+025700	149.84037	2.95013	2.0	No HST image
HSCJ100307+020241	150.78256	2.04484	1.6	No HST image
HSCJ095943+022046	149.93252	2.34623	1.6	
HSCJ095744+023835	149.43571	2.64332	1.6	
HSCJ100050+031825	150.21200	3.30706	1.6	No HST image
HSCJ100129+024427	150.37457	2.74093	2.0	Lensed galaxy candidate by serendipitous discovery.

Table 5.2: Name, RA, DEC, and average score from visual inspection of the candidates with average scores higher than 1.5. HSCJ095921+020638 is the only known quadruply lensed quasar in the COSMOS field, and HSCJ100129+024427 is more likely a candidate of lensed galaxy. Only four of these objects have the HST F814W images (figure 5.2).

our visual inspection. The discussion about the objects that meet the variability selection criteria but get rejected by CHITAH is in section 5.3.3.We compare our lens candidates to previously identified candidates from other searches in section 5.3.4.

5.3.1 Final candidates

Figure 5.1 shows the eight final candidates, seven lensed quasar candidates and one lensed galaxy candidates. In figure 5.1, the first column are their *gri*-composited images with a cutout size at $10''\times 10''$, and the yellow boxes are the regions where we run CHITAH ($7''\times 7''$). The second column shows their difference images at the epoch that they meet the variability selection criteria, and the third column is the corresponding effective regions. The fourth and the fifth columns are their lens galaxies and lensed features predicted by CHITAH.

The highest scored candidate, HSCJ095921+020638, is a known lensed quasar (Anguita et al., 2009). The recovery of HSCJ095921+020638 indicates the feasibility of our time-variability-based lens searching method. HSCJ095921+025700 is picked out by the variability selection due to the loose criteria ($p_{\rm thrs}\% = 50\%$ and $N_{\rm thrs} = 0$). Under these loose criteria, a HSC variable could be selected out as long as it has non-zero effective region in one of certain epochs, even if the effective region comes from the accumulation of noise peaks. Although the loose criteria are sensitive to noise peaks, they are still feasible for the COSMOS field we examine in this work. Moreover, the loose criteria allow us to have a more complete sample that includes lensed quasars with faint brightness or small separation.

Our time-variability-based search method picked out HSCJ100129+024427 in an earlier version of our code by mistake (and luck!). HSCJ100129+024427 has zero effective region area across all the 13 epochs, and the final variability selection actually does not pick it out. Given its lens-like appearance, we keep this system for further investigation: CHITAH identifies the lensing feature of HSCJ100129+024427, followed by an average score of probable lens from the visual inspection. Therefore, HSCJ100129+024427 is more likely a candidate of lensed galaxy, instead of a candidate of lensed quasar.

We also show Hubble Space Telescope (HST) F814W images of HSCJ095921+020638, HSCJ100129+024427, HSCJ095943+022046, and HSCJ100050+031825 in figure 5.2. From the HST images, we could clearly see the four multiple images in HSCJ095921+020638 (top-left panel in figure 5.2), and three possible lensed images in HSCJ100129+024427 (top-right panel in figure 5.2). On the other hand, the lensed features of HSCJ095943+022046 and HSCJ100050+031825 are hard to see, and these two objects are more possible to be spiral galaxy or galaxy with dust lane.

5.3.2 CHITAH false-positives

Figure 5.3 are examples of the objects that get selected out by both the time-variability-based selection and CHITAH, but rejected in the visual inspection by DCYC, JHHC, and SHS. Those objects are called CHITAH false-positives in this work. Similar to figure 5.1, the columns in figure 5.3 are *gri*-composited images, difference images, the effective regions, CHITAH-predicted lens galaxies, and CHITAH-predicted lensed features, respectively.

Both in only one epoch, HSCJ100129+020620 and HSCJ100244+015514 have effective regions larger than $A_{\mathrm{eff},t}(p_{\mathrm{thrs}}\% = 50\%)$, and their effective regions are only 1-2 pixels at those epochs (2016-12-25 and 2017-03-30, respectively). Moreover, the effective region of HSCJ100129+020620 more likely comes from noise peaks. Such misidentification of objects like HSCJ100129+020620 and HSCJ100244+015514 could be avoided by applying stricter criteria for the time-variability-based selection (larger values for $p_{\mathrm{thrs}}\%$ or N_{thrs}), though we might lose the candidates of faint or small-separation lensed quasars by doing so.

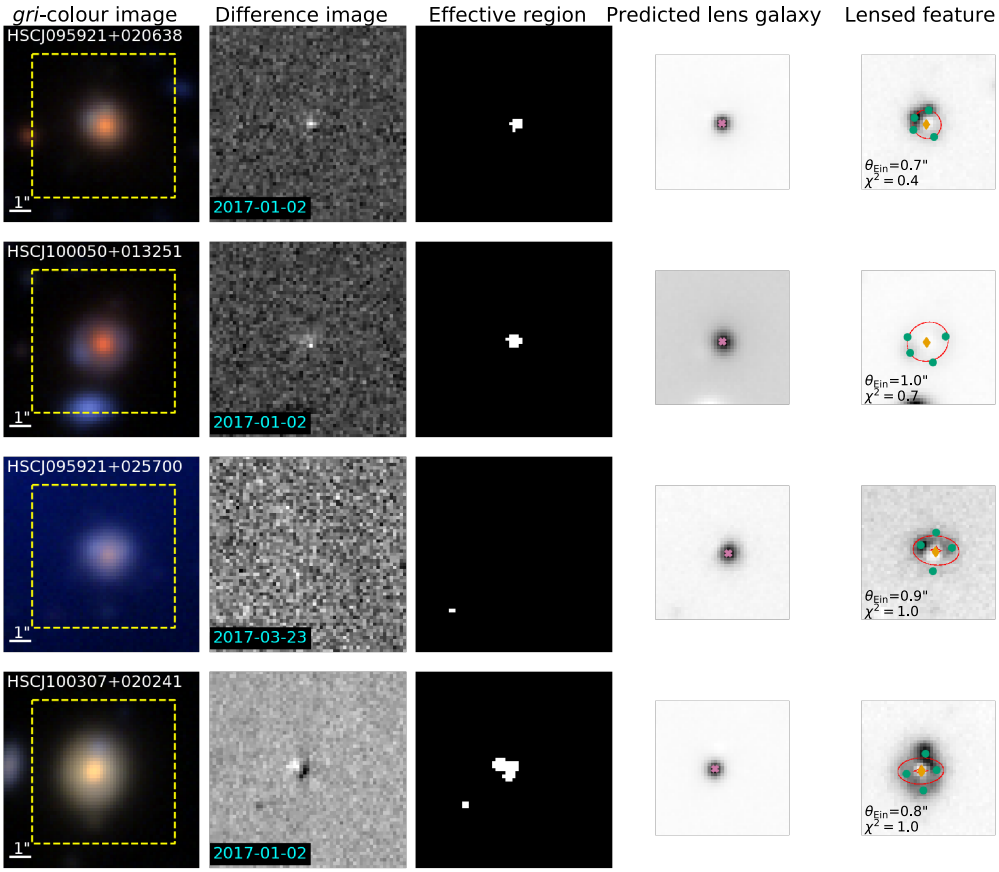

Figure 5.1: Final candidates, the variable objects identified as lensed quasars by both the time-variability-based method and CHITAH with average scores higher than 1.5 from the visual inspection. The first column shows the *gri* image of each final candidate. The second column shows their difference images in the epoch that they meet the time variability selection criteria, and the third column is their corresponding effective region, a quantification of the object's spatial extendedness in the difference image. The fourth column shows the lens galaxy predicted by CHITAH with the lens center marked as magenta cross. The fifth column is their predicted lensed feature by CHITAH with their best-fit SIE model. In the fifth column, the positions of the fitted lensed images are in green dots, the predicted source position is labeled as the yellow diamond, and the red curves are the critical and caustics curves of their best-fit SIE model. The time-variability-based selection uses cutouts of $10'' \times 10''$ (first three columns), and CHITAH uses cutouts of $7'' \times 7''$, which is the yellow dash box in the first column. HSCJ095921+020638 is the only known quadruply lensed quasar in the COSMOS field, and the recovery of HSCJ095921+020638 shows the feasibility of the time-variability-based lens search method. The constraints we apply in the variability selection are so loose that a variable object could be selected as a candidate as long as it has non-zero effective region in certain epochs, even though the effective region area might occasionally come from the accumulation of noise peaks, such as in HSCJ095921+025700.

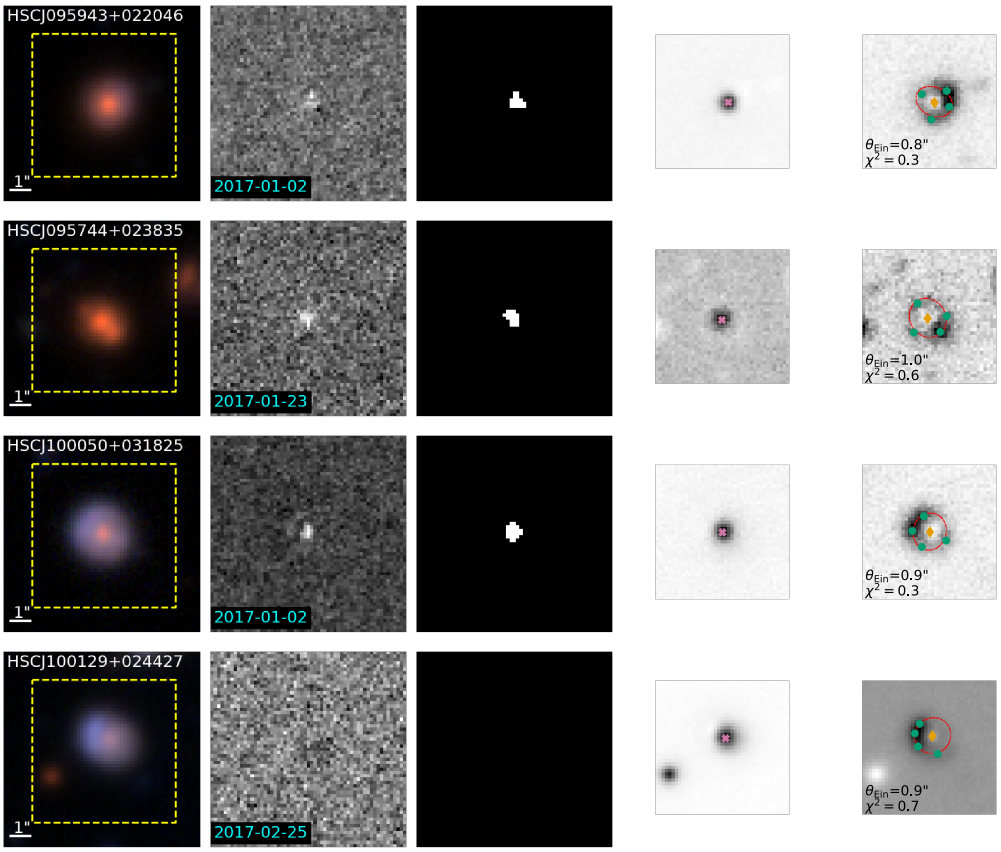

Figure 5.1 (Continued): HSCJ100129+024427 is a serendipitous discovery, as it has zero effective region area across all the 13 epochs, which shows that it is more likely a candidate of lensed galaxy. CHITAH identifies the lensing feature of HSCJ100129+024427, and our visual inspection grade suggests it as a probable lens (average score: 2.0).

Comparing to the final candidates and to the other CHITAH false-positives, HSCJ100226+005858 exhibits a different color in the *gri*-composited image, and it has a rather round and compact shape. In fact, HSCJ100226+005858 is classified as a star in the internal HSC transient catalog (Yasuda et al., 2019). HSCJ100226+005858 is probably a variable star or a star that is too bright for the transient pipeline to subtract the light perfectly, since it has substantial amounts of the effective regions across almost all the eight epochs that it has been observed in *i*-band (see section 5.3.3 for detail).

The nearly monotone color indicates that HSCJ100332+013852 is unlikely a lensed object. From the *gri*-composited image, HSCJ100332+013852 is likely a merger of two or more galaxies. Such merger process might trigger AGN activity that results in effective regions passing our selection criteria.

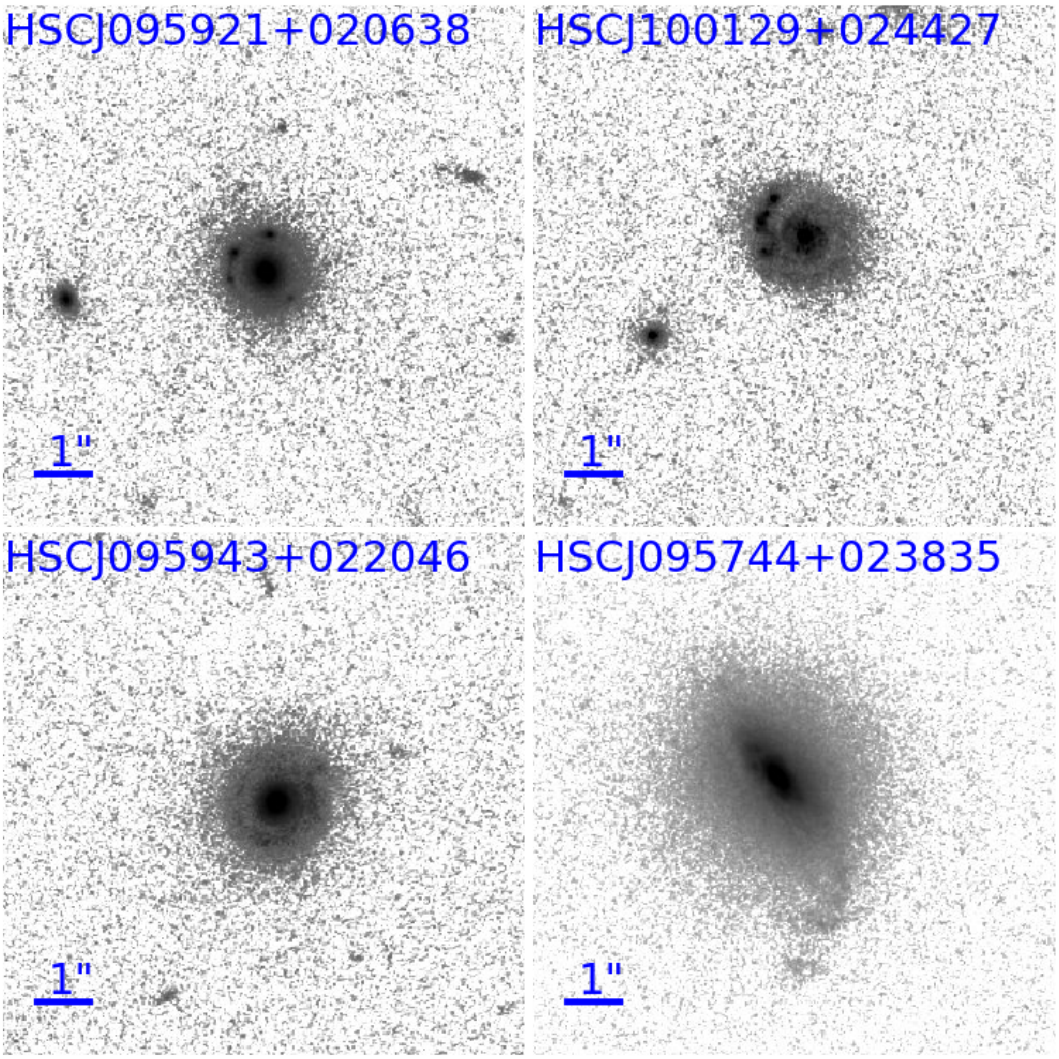

Figure 5.2: The HST F814W images of four final candidates. HSCJ095921+020638 (top-left) is the only known quadruply lensed quasar in the COSMOS field, and we could see the four lensed images around the lens galaxy. In HSCJ100129+024427 (top-right), three possible lensed images are around the possible lens galaxy, while they could also be the nearby objects, instead of lensed images. HSCJ095943+022046 and HSCJ095744+023835 (bottom panels) are more possibly dusty galaxy or spiral galaxy, as the lensed features are hardly visible.

HSCJ100319+021447 shows a possible tidal feature around the top-right, and the possible tidal event could be the reason for the variable brightness. Moreover, CHITAH identifies the blue trait around this possible tidal feature as the lensed images in HSCJ100319+021447, hence the misidentification of HSCJ100319+021447.

HSCJ095904+014812 is classified as a supernova in the internal HSC transient catalog, and it exploded during the survey period in table 5.1, resulting in the substantial effective region areas. Furthermore, the blue features in HSCJ095904+014812 are likely star-forming regions of a spiral galaxy, and these blue features cause the misidentification from CHITAH. HSCJ095949+014141 is also classified as a supernova in the internal HSC transient catalog. While HSCJ095949+014141 appears as binary, CHITAH misidentifies it as a lens because of the color gradient in the bottom-right object (so part of the object is mistaken as lensed features) or imperfect PSF matching.

5.3.3 Variability false-positives

Here we examine the objects selected by the time-variability-based selection but rejected by CHITAH, and we call these objects variability false-positives in this work. Many of variability false-positives have extremely large effective region areas across all the epochs, which are due to artificial effects, as the examples shown in figure 5.4. Such misidentification like figure 5.4 could be prevented by assigning an upper limit on the effective region area. We could discard a HSC variable from the lens candidate selection if its effective region area exceeds the upper limit in one of the epochs, since the abnormally large number of the effective region area suggests that heavy artificial effects happen around the HSC variable and that the detection of the HSC variable is not reliable.

Many point-like variability false-positives have effective region areas that are even larger than most of our final candidates and the visual false-positives, which means that we could not properly remove these variability false-positives from the lens candidate selection by applying stricter constraints on $p_{\mathrm{thrs}}\%$ and N_{thrs} without losing the promising lensed quasar candidates. We show some examples of these point-like variability false-positives in figure 5.5. As shown in fig-

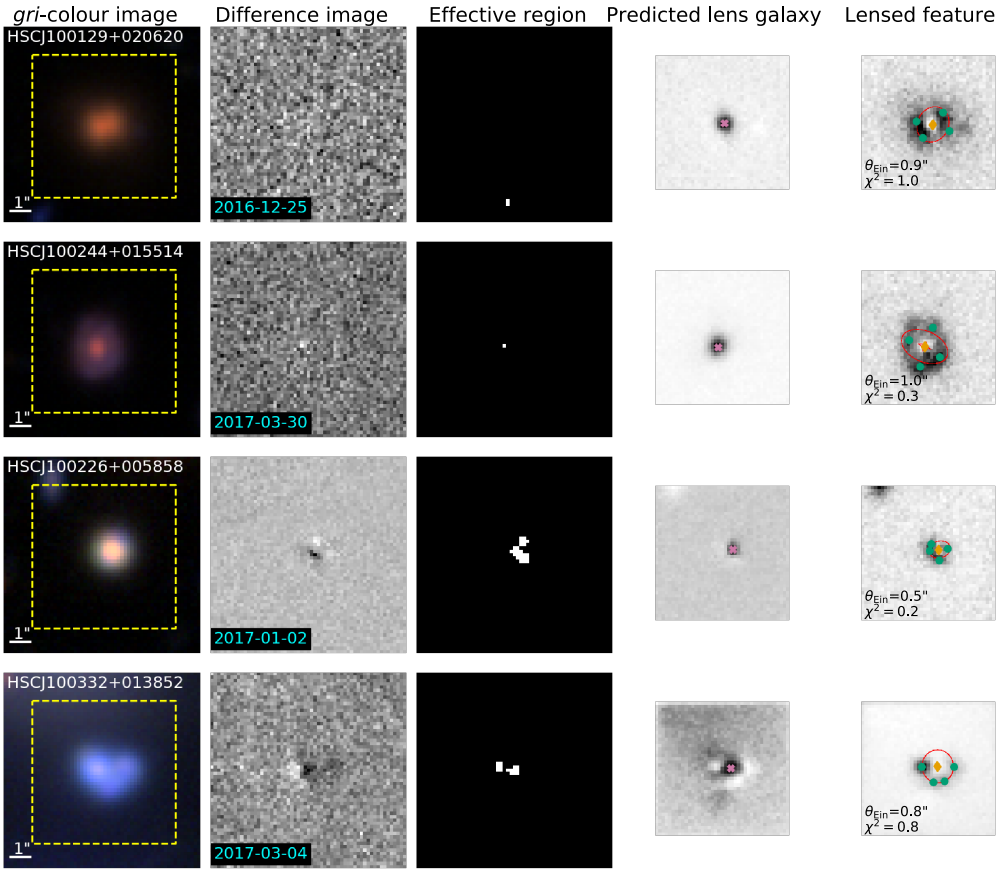

Figure 5.3: Examples of CHITAH false-positives, the variable objects identified as lensed quasars by both the time-variability-based method and CHITAH, but rejected by the visual inspection. Similar to figure 5.1, the first column is the *gri* images, the second column is the difference images in the epoch they meet the variability selection criteria, the third column is the corresponding effective region, the fourth column is the predicted galaxies from CHITAH, and the fifth column is the lensed feature predicted by CHITAH with the best-fit SIE model. In addition to the objects barely qualified the variability selection by the noise peaks, other common cases of CHITAH false-positives are very bright objects, objects with tidal features, mergers that trigger AGN activities, and spiral galaxies with supernova exploded during survey period. For more details about CHITAH false-positives, one could refer to section 5.3.2.

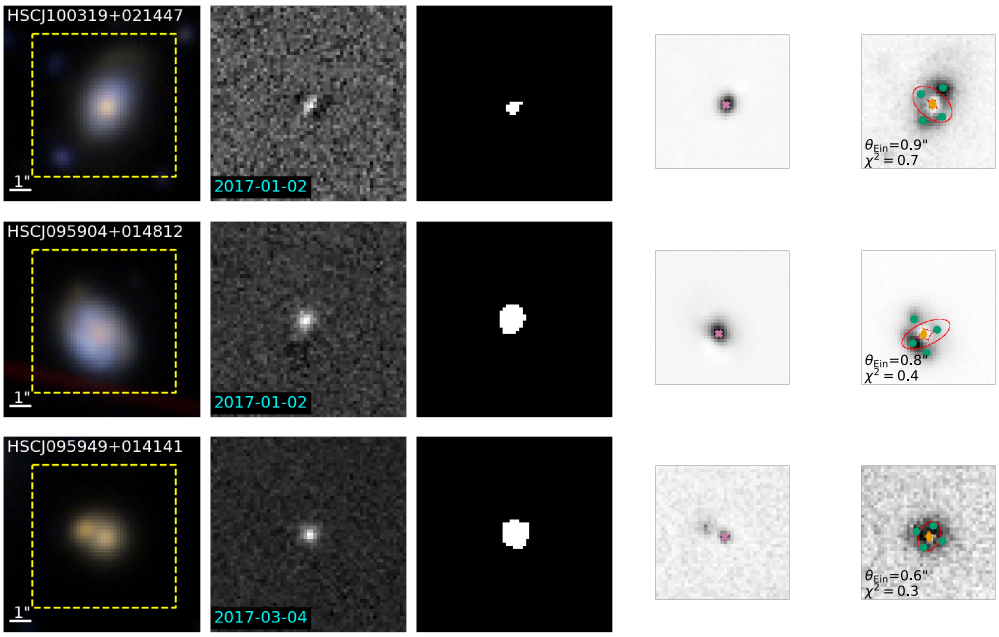

Figure 5.3 (Continued)

ure 5.5, HSCJ095725+021832, HSCJ100042+022311, and HSCJ095821+020532 have "Taiji-like" dipole patterns - black on top(bottom) and white on bottom(top), or black on left(right) and white on right(left), in their difference images. The Taiji-like patterns are possibly caused by the objects' brightnesses. From the simulation work in chapter 4, we found that an object starts to have the Taiji-like dipole residual in the difference images when it is brighter than $\lesssim$ 21.5 mag, regardless whether the object is variable. The possible reason is that the transient pipeline no longer performs the image subtraction perfectly and it could not subtract the light correctly when an object is too bright ($\lesssim$21.5 mag). The brighter the object is, the more obvious the Taiji-like pattern is in the difference image. The Taiji-like residuals contribute larger effective region areas, and the time-variability-based selection would therefore misidentify these point-like objects as lensed quasar candidates.

In addition to those objects with Taiji-like residuals, some of the variability false-positives could also be variable stars or unlensed quasars, like HSCJ100159+025933 and HSCJ100041+030113. They are classified as star and quasar in the internal HSC transient catalog, respectively. Although not listed in the internal HSC transient catalog, HSCJ100055+030138 is possibly a variable star or an unlensed quasar as well. We inspect the difference images of 13 epochs, the corresponding effective regions, and the colour-composited images of HSCJ100055+030138 and find that

its effective region areas might come from substantial brightness change, instead of noise peaks or improper image subtraction. Ideally, lensed quasars have larger effective region areas due to their multiple-image features, and strict thresholds on the effective region areas for the variability selection should largely decrease the number of those point-like false-positives, such as variable stars or unlensed quasars, without aggressively losing the lensed quasar candidates. However, in this work, our final candidates of lensed quasars generally have smaller effective regions than the CHITAH false-positives and the variability false-positives. Although the loose constraints on the time-variability-based selection in this work yield huge number of non-lensed objects, they seem to be necessary for securing the lensed quasar candidates. Therefore, CHITAH is important as the second step in this lens search starting from the time variability, since it discards the point-like objects with large effective regions and efficiently decreases the number of lensed quasar candidates without missing the promising ones.

5.3.4 Discussions

We look into literature to check if any of our final candidates has been found as a lens system. Except HSCJ095921+020638, none of the other final candidates has been found as a lens. Among the final candidates, HSCJ100050+013251, HSCJ100307+020241, HSCJ095943+022046, and HSCJ095744+023835 are listed in the galaxy catalog of Capak et al. (2007), and our serendipitous discovery, HSCJ100129+024427, is listed as a bright galaxy in the catalog of Lilly et al. (2009).

The recovery of the known lensed quasar, HSCJ095921+020638, and the discovery of the other final candidates could represent the completeness of our lens search, since we estimate the quad(s) lying in the Ultra-Deep layer of the COSMOS field within the HSC transient survey (i ~26.0 mag) at about 1 ± 1, based on the lensing rates in OM10 and the correction in Spiniello et al. (2018). We further find that the strictest criterion for HSCJ095921+020638 to qualify the time-variability-based selection is $(p_{\rm thrs}\%, N_{\rm thrs}) = (50\%, 6)$. With $(p_{\rm thrs}\%, N_{\rm thrs}) = (50\%, 6)$, the time-variability-based selection would identify 32,127 out of the 101,353 HSC variables as lensed quasar candidates, and 936 out of these 32,127 objects would further be identified as lensed quasar candidates by CHITAH. In the end, under the same visual inspection, only four objects in table 5.2 will remain as final candidates (HSCJ095921+020638, HSCJ095943+022046, HSCJ095744+023835, and

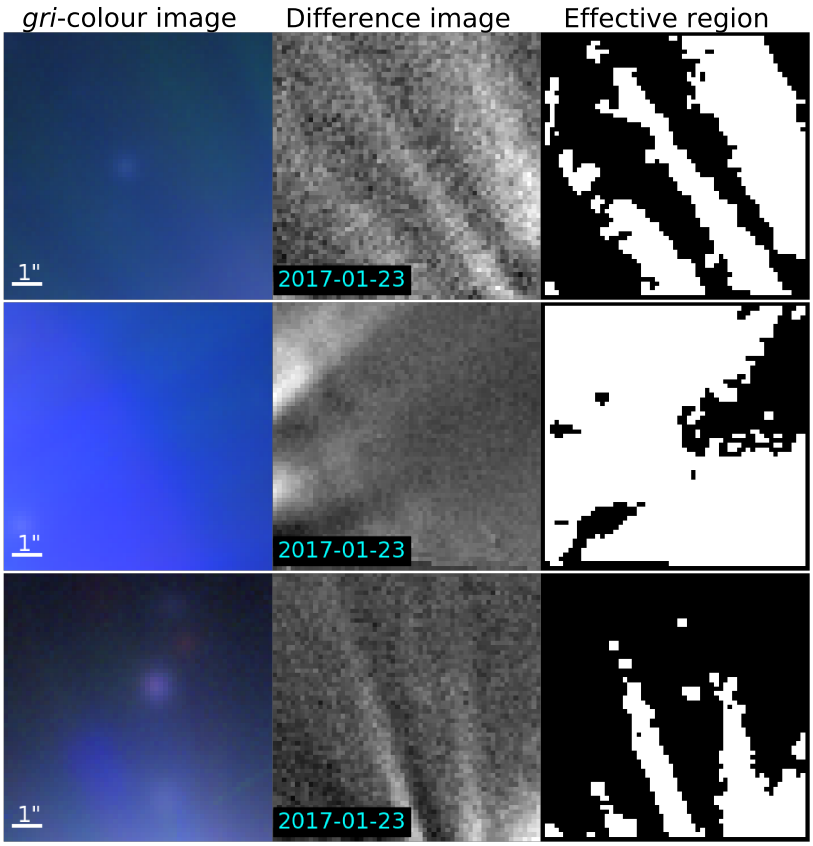

Figure 5.4: The artificial effects that get selected out by the time-variability-based selection due to the extremely large effective regions. The extremely large effective regions are resulted from artificial effects, and such misidentification could be avoided by imposing an upper limit on the effective region area in the variability selection.

HSCJ100050+031825), if we apply $(p_{\rm thrs}\%, N_{\rm thrs}) = (50\%, 6)$ in the time-variability-based selection. We note that COSMOS field is small and HSCJ095921+020638 is faint, so the loose constraints applied in this work to recover HSCJ095921+020638 might not be mandatory for a more general lensed quasar search in a larger field, as chapter 4 demonstrates that we could find bright lensed quasars with wide separation at true-positive rate of 90.1% and false-positive rate of 2.3% with $(p_{\rm thrs}\%, N_{\rm thrs}) = (95\%, 9)$. In future applications of this method to larger cadenced image surveys, the selection criteria are adjustable to balance between purity and completeness.

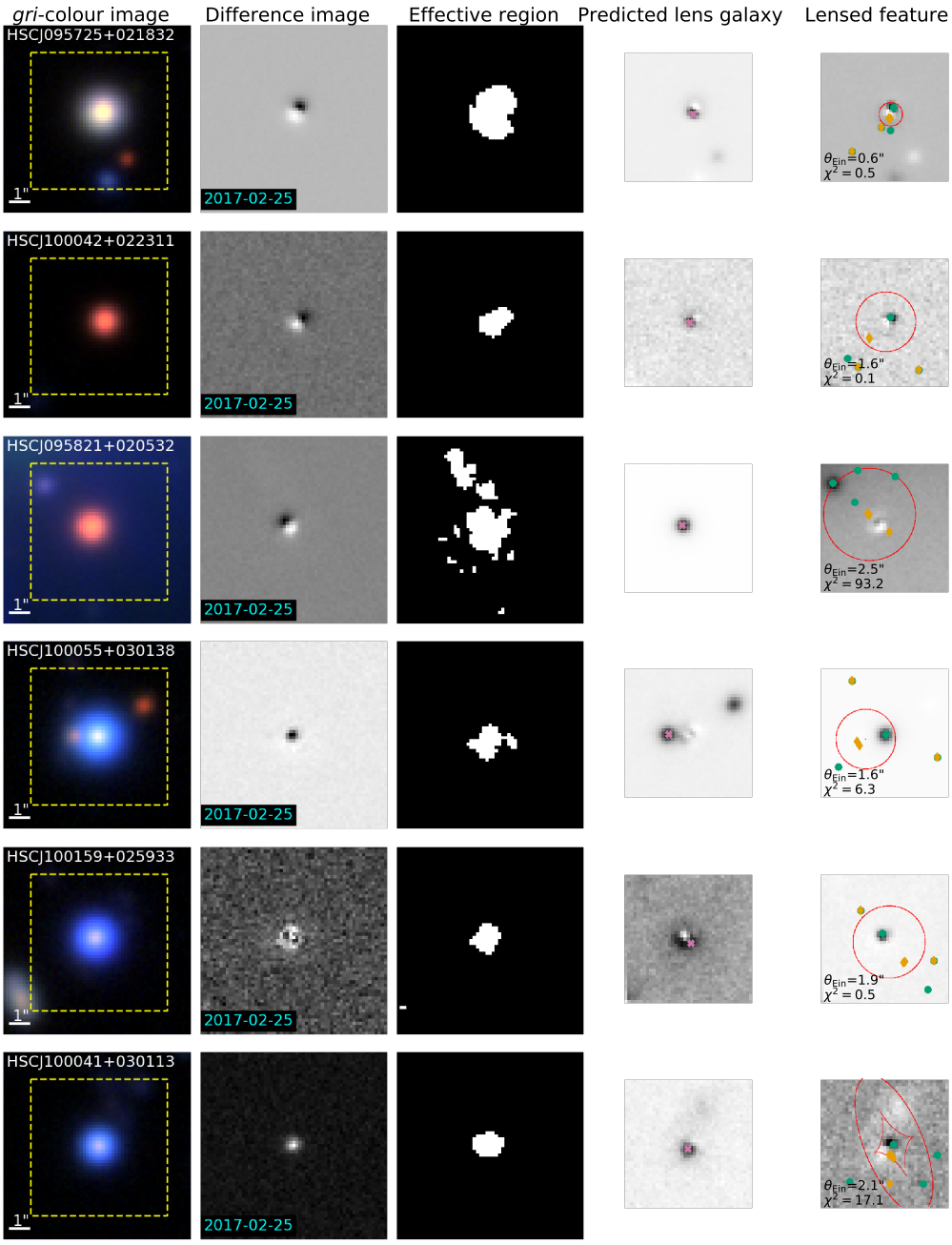

Figure 5.5: Examples of variability false-positives, the variable objects identified as lensed quasars by the time-variability-based method, but rejected by CHITAH. Similar to figure 5.1 and figure 5.3, the first column is the *gri* images, the second column is the difference images in the epoch they meet the variability selection criteria, the third column is the corresponding effective region, the fourth column is the predicted galaxies from CHITAH, and the fifth column is the predicted lensed features by CHITAH with the best-fit SIE models. Other than those extremely bright objects that results in the incorrect image subtraction, variable stars and unlensed quasars are also common cases of variability false-positives. As the time-variability-based method itself is not efficient in removing these variability false-positives from the lens selection, CHITAH is useful to discard these point-like variability false-positives and thus important as an advanced step after the variability selection (see section 5.3.3 for more detail).

5.4 Summary

In this chapter, we presents the first application of the lensed quasar search method developed in chapter 4. We apply this time-variability-based method to the HSC transient survey. We first use *i*-band difference images from the HSC transient survey to select out objects with this time-variability-based method, based on their spatial extendedness in the difference image. We run CHITAH, a lens search algorithm based on the image configuration, on the objects selected by the difference image. In the end, we visually inspect the objects that are both selected by the time-variability-based method and CHITAH and grade them. We summarize this variability-based lens search as follows:

1. Among the 101,353 HSC variables, the time-variability-based method conservatively selects 83,657 HSC variables as potential lensed quasar candidates with loose criteria. Among the 83,657 HSC variables, CHITAH further identifies 2,130 as lensed quasar candidates. The visual inspection picks out seven from the 2,130 lensed quasar candidates as final candidates. In addition to the seven final candidates, we serendipitously find one lensed galaxy candidate.

2. As a first application, we use the time-variability-based method from chapter 4 in a conservative manner, so we could check the false-positive patterns it yield and also not to lose possible lensed quasars. Although this variability-based method is helpful in selecting potential lensed quasar candidates by picking out objects with larger spatial extendedness in the difference image, this work shows that our final candidates generally have spatial extendedness smaller than the false-positives, indicating that tightened criteria in the variability selection might not be an ideal means to improve the lens search efficiency in COSMOS.

3. Since using the time-variability-based method alone might not be efficient, CHITAH is important as a further examination to remove the false-positives from the variability selection through object configurations, especially for discarding those point-like false-positives.

4. For future lensed quasar searches in larger sky areas, we could use stricter criteria for the time-variability-based method to reduce the false-positive

rates. The only known lensed quasar in the field we examine in this work, HSCJ095921+020638, is a special case of faint lensed quasars, and the loose constraints on the time-variability-based method exploited in this work to recover HSCJ095921+020638 are not indispensable.

We have shown in this chapter that, the time-variability-based lens search method from chapter 4 is workable, and a combination of other lens search techniques as an advanced check like CHITAH will improve the lens search efficiency. The results in this chapter also encourage the application of the variability-based lens search method to other cadenced imaging surveys, such as the upcoming Rubin Observatory Legacy Survey of Space and Time (LSST). We will discuss the prospects of using this time-variability-based lens search method in chapter 6.

Chapter 6

CONCLUSION AND FUTURE PROSPECTS

In this thesis, we explore the time variability of lensed quasar through difference imaging. Our main goal is to develop a systematic method detecting lensed quasar with such time variability. To understand how the difference images reveal the time variability of lensed quasar, we first built a pipeline to simulate the time-varied lensed images. From the simulation, we found that the mock lensed quasars tend to have larger spatial extendedness in the difference images than the non-lensed variable sources. Therefore, we developed the lensed quasar search algorithm using the difference images to quantify the objects' spatial extendedness and pick out objects with large spatial extendedness (chapter 4).

Practically, we applied this time-variability-based lens search method to the HSC transient survey. We recovered the only known lensed quasar in the survey field, and found other lens candidates, including a lensed galaxy candidate discovered by serendipity. However, in the application to the real variable objects from the HSC transient survey, it is not definite that the lensed quasar candidates have larger spatial extendedness in the difference images than the non-lensed variable sources, as there are many factors other than the lensed feature, such as object brightness, affecting the spatial extendedness in the difference images. Therefore, a combination of our time-variability-based lens search method with other lens search techniques, such as CHITAH (Chan et al., 2015) in this thesis, will enhance the lens search efficiency (chapter 5). Another possible way to improve the lens search efficiency is to exploit the variabilities in the other bands, as we have only used *i*-band in this thesis. The extension of the time-variability-based lens search method to other bands is left to a future work.

6.1 Application to the LSST

The feasibility of the time-variability-based lens search method implies its application to other cadenced survey, such as the LSST. The LSST is expected to have a image quality as similar as the HSC transient surveys, but with a much larger sky coverage. Although the LSST pixel size ($0.2''$) is slightly larger than the HSC

transient survey (0.17″), the effective region is expected to still be distinguishable between potential lensed quasar candidates and non-lensed variable sources, as long as we adopt large $p_{\rm thrs}\%$ ($p_{\rm thrs}\% > 92.5\%$). We can use the simulation pipeline built in chapter 4 with the LSST image quality and cadence strategy, to generate LSST-like mock lenses, for the investigation of this time-variability-based lens search in the LSST. In principal, with the methods demonstrated in chapter 5, we expect to skilfully discover thousands of lensed quasars in the LSST.

6.2 Neural network for lensed quasar search using the difference images

Since lens systems have specific image patterns, using neural networks trained on the mock lens images is powerful in searching for lens systems (e.g., Canameras et al., 2020; Huang et al., 2020; Cheng et al., 2020). Most of the present image-based convolution neural networks (CNNs) established for lens searches are dedicated to lensed galaxies. While the difference images show only the variable sources in principal, a CNN trained on the difference images of the mock lensed quasars and non-lensed variable sources is a possible tool to find lensed quasars.

CNNs recognize the image specifics by learning the coefficients of convolutional kernels at assigned size. For a CNN that identifies lensed quasars by using difference images, the learning process in principal is to derive a model for classifying variable objects in the training set of lensed quasars and non-lensed variable objects based on their input difference images. Sample sizes of the training sets at a few 10^4 to a few 10^5 difference images should be sufficient for this two-class classification (lensed quasars and non-lensed variable objects) on the galaxy-scale image cutouts (e.g., Jacobs et al., 2017; Jacobs et al., 2019). Actually, we are already able to largely produce the difference images of mock lensed quasars with the simulation pipeline in chapter 4 for the CNN training sets.

Realistic difference images of mock lensed quasars and the choices of non-lensed variable objects are crucial for CNN classification performance (e.g., Lanusse et al., 2018). The mock difference images in chapter 4 might not be realistic enough for CNN, as we did not include the Poisson noises resulted from the brightness we inject into the visits/exposures. Before we start to generate the large number of difference images for CNN training, we should investigate how such Poisson noises propagate

from the warped visits to the deep difference images, and add possible Poisson noises when we inject the mock lensed quasars into the warped visits. While the mock lensed quasars train the CNN classification to pick, the non-lensed variable objects work as negatives that train the CNN classification "not to pick". Around 50% of the negatives should be the variable objects that are easily to be misidentifed as lensed quasars in the difference images, so the CNN will learn that those negatives are contaminants. These contaminants are not exactly the same as the CHITAH false-positives in chapter 5, since many CHITAH false-positives are misidentified through the effective region areas and the *gri*-composite images, not exactly through the difference images themselves. For example, it is very possible that HSCJ100129+020620 and HSCJ100244+015514 in figure 5.3 are easy for the CNN to identify as non-lensed variable objects, as they show nearly nothing in the difference images. Both HSCJ100129+020620 and HSCJ100244+015514 are not the kind of negatives that the CNN will easily misidentify as lensed quasars. The contaminants in the difference images that the CNN will misidentify as lensed quasars are possibly quasar binaries, mergers triggering AGN activities (e.g., HSCJ100332+013852 in figure 5.3), face-on spiral galaxies with supernovae (e.g., HSCJ095904+014812 in figure 5.3), objects brighter than 21.5 mag (see detail in section 5.3.3), or etc.. In order to develop a CNN for lensed quasar search based on the difference images, we need to first investigate the contaminants that are easily misidentified as lensed quasars in the difference images. Objects in figure 5.4 or objects like HSCJ100129+020620 and HSCJ100244+015514 are not very useful in training the CNN classification, as the CNN learns little from them.

Although we can use the 13-epoch difference images based on the cadence strategy of the HSC transient survey as 13 inputs to train a CNN or to train 13 CNNs with one input for each[1], the most efficient way to establish a lensed quasar search CNN with the materials we develop in this thesis is to train a CNN with the difference images at a certain epoch, as an ideal lens search algorithm for cadenced survey is to discover lensed candidates right away at the present epoch. After the investigation of technical essentials such as CNN architecture, and the examination for the possible Poisson noises and difference image contaminants mentioned above, generally we can use the mock lenses produced by the general simulation pipeline in chapter 4 and the real observational variable objects from section 5.1 to train a lensed quasar search CNN for the epoch with median seeing, in which we have the best lens

[1]The different seeings are encoded in the difference images as hidden inputs.

search performance with only one single-epoch (section 4.4.3). We anticipate the combination of deep learning and difference imaging to be an efficient and powerful approach to find lensed quasars in the era of cadenced wide-field imaging surveys.

Appendix A

EXTRA EXAMINATION FOR THE ALGORITHM

This chapter provides supplementary materials of chapter 4. In section A.1, we examine the sensitivity of the lens search algorithm developed in chapter 4, showing that our lens search sensitivity is dependent on the lensed quasar separation rather than the lensed quasar time delay. In section A.2, we show the lens search sensitivity to the unresolved total brightness.

A.1 Sensible separation or sensible time delay

We examine whether our lens search sensitivity has dependence on the lensed quasar time delay by checking the longest time delay, $\Delta t_{\rm max}$, in each lensed quasar. Figure A.1 shows the distribution of $\Delta t_{\rm max}$ in each $\theta_{\rm LP}$ bin. The top panel in figure A.1 shows the mean value of $\Delta t_{\rm max}$ with 1σ-standard-deviation as the error bar from the lensed quasars in each $\theta_{\rm LP}$ bin. From the top panel in figure A.1, we could see that both the group of non-selected lensed quasars and the group of selected lensed quasars by our lens search method ($p_{\rm thrs}\% = 95\%$, $N_{\rm thrs} = 9$) have similar distribution of $\Delta t_{\rm max}$ as all the lensed quasars, indicating that the lens search sensitivity has no preference on the lensed quasar time delay. On the other hand, the middle panel in figure A.1 shows again that the number of selected lensed quasars decreases as the $\theta_{\rm LP}$ decreases, while the number of non-selected lensed quasars increases as the $\theta_{\rm LP}$ decreases. Therefore, the lensed quasar separation is sensible of our lens search algorithm, whereas the lensed quasar time delay is not.

A.2 Sensitivity to total (unresolved) brightness

For a more realistic study, we investigate the lens search sensitivity to the lensed quasars total brightness, $m_{\rm total}$ (i-band). Figure A.2 shows the sensitivity to $m_{\rm total}$, when applying the lens search method based only on spatial extent at $(p_{\rm thrs}\%, N_{\rm thrs}) = (95\%, 9)$ (Section 4.3.1 and Section 4.4.1). As shown in figure A.2, regardless of the separation, our lens search algorithm could capture all the lensed quasars with $m_{\rm total} < 19.0$ mag. We further examine the sensitivity for the lensed quasars with $m_{\rm total} > 19.0$ mag in figure A.3. Figure A.3 shows that our lens search algorithm could still identify more than 70% of the lensed quasars with 19.0 mag $< m_{\rm total} <$

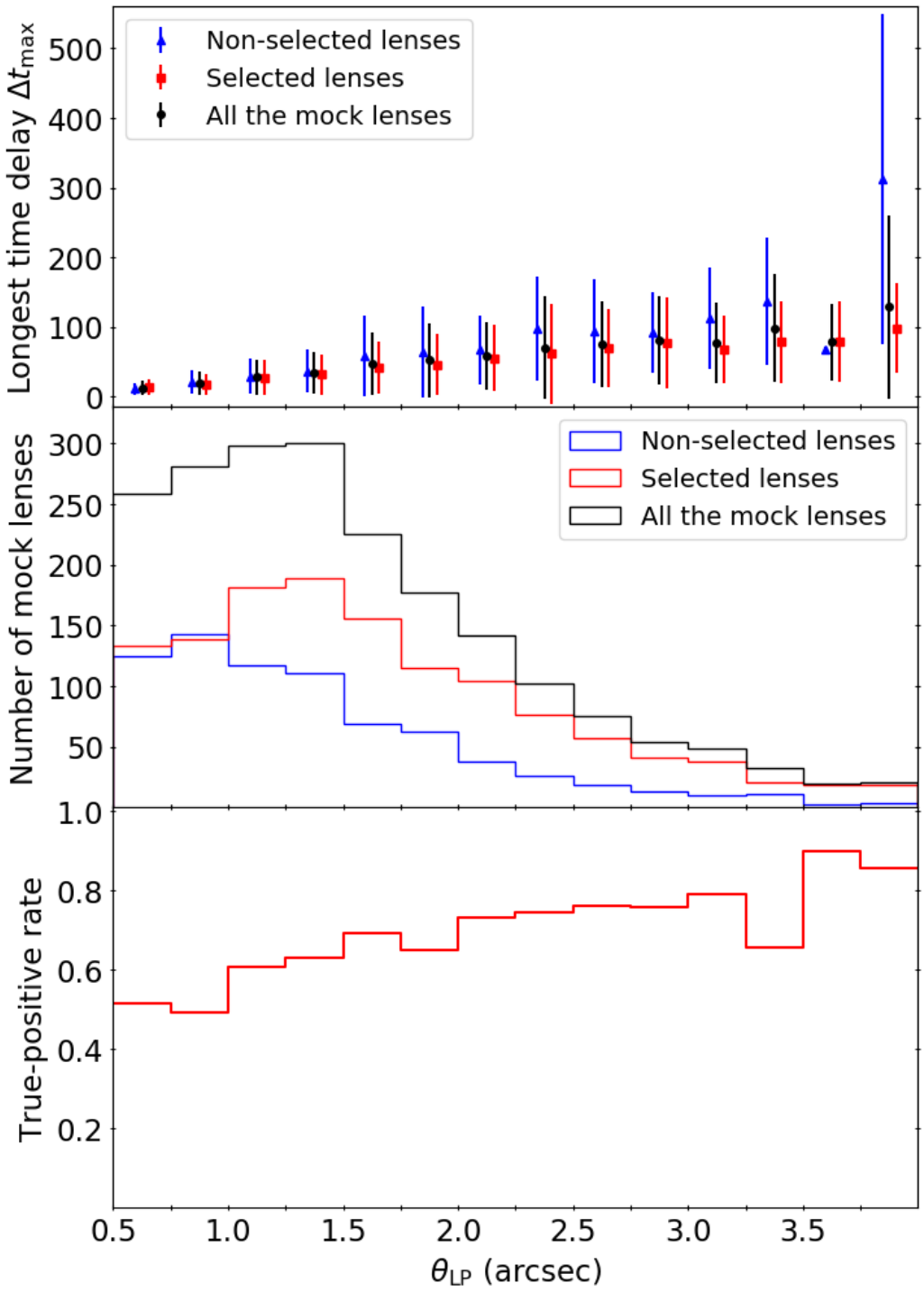

Figure A.1: Distribution of the longest time delay $\Delta t_{\rm max}$ for the non-selected lensed quasars and the selected lensed quasars. The top panel shows the mean values of $\Delta t_{\rm max}$ with 1 standard deviation as the error bars from the lensed quasars in each $\theta_{\rm LP}$ bin. The middle panel shows the number of non-selected lensed quasars, the number of selected lensed quasars, the number of total mock lenses in each $\theta_{\rm LP}$ bin. The bottom panel shows the true-positive rate in each $\theta_{\rm LP}$ bin. The sensitivity of our lens search algorithm mainly comes from the separation ($\theta_{\rm LP}$), not the time delay ($\Delta t_{\rm max}$).

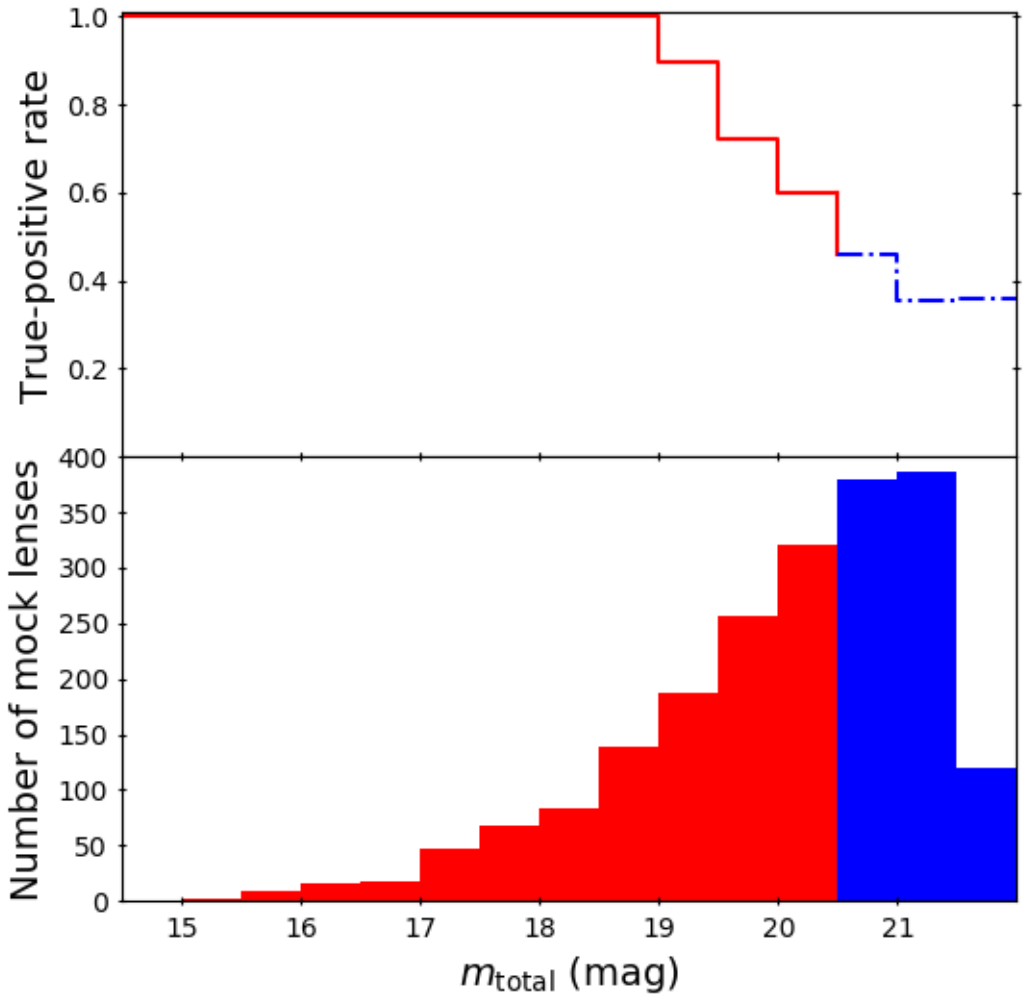

Figure A.2: Sensitivity to the lensed quasar total brightness m_{total} of the lens search method based only on spatial extent, when $p_{\mathrm{thrs}}\% = 95\%$ and $N_{\mathrm{thrs}} = 9$. Our lens search algorithm could capture all the lensed quasars with m_{total} 19.0 mag.

20.5 mag when $\theta_{\mathrm{LP}} > 1.5''$ (the largest separation among the pairs in one lens system), while the lens search performance is relatively poor for the lensed quasars with $m_{\mathrm{total}} > 19.5$ mag when $\theta_{\mathrm{LP}} \leq 1.5''$.

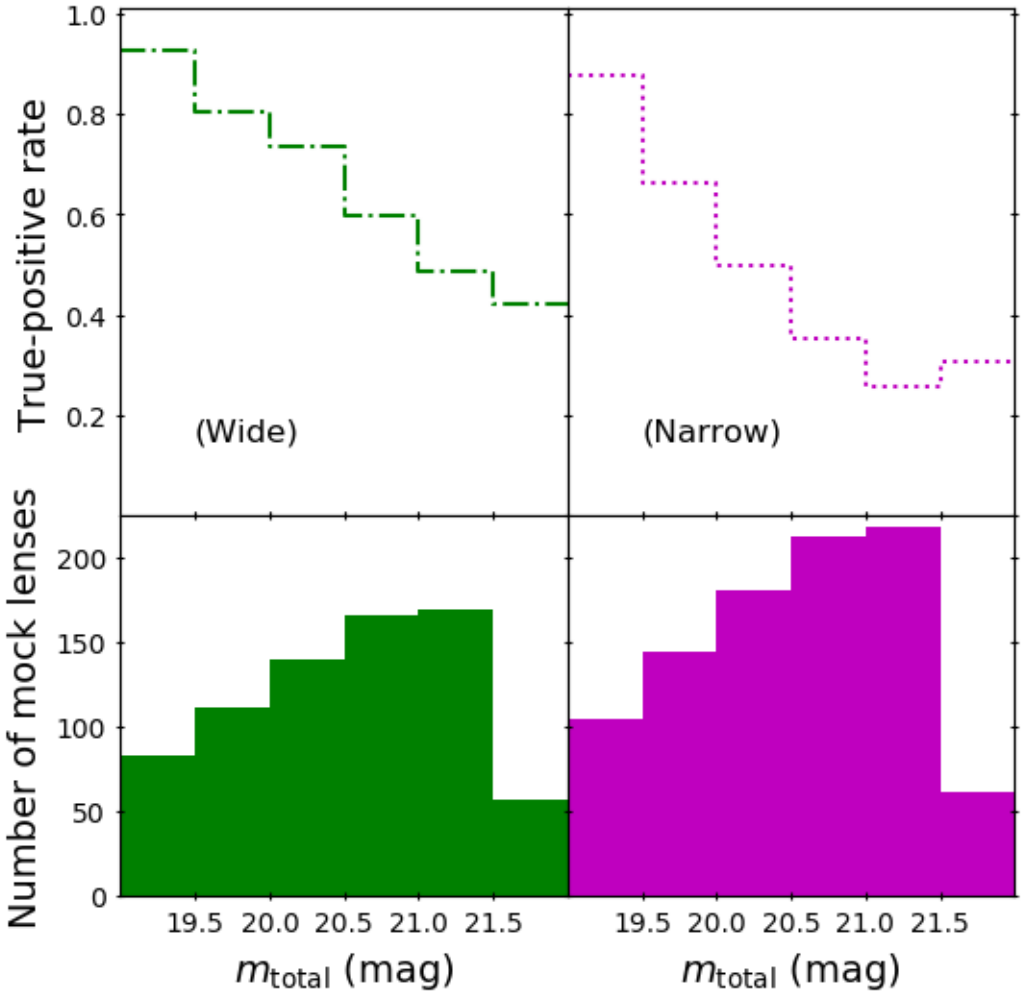

Figure A.3: Sensitivity to the lensed quasar total brightness m_{total} for the lensed quasars fainter than 19.0 mag. Wide: the group of lensed quasars with the largest separation among the pairs $\theta_{\mathrm{LP}} > 1.5''$. Narrow: the group of lensed quasars with $0.5'' < \theta_{\mathrm{LP}} \leq 1.5''$.

BIBLIOGRAPHY

Abolfathi, Bela et al. (Apr. 2018). "The Fourteenth Data Release of the Sloan Digital Sky Survey: First Spectroscopic Data from the Extended Baryon Oscillation Spectroscopic Survey and from the Second Phase of the Apache Point Observatory Galactic Evolution Experiment". In: *The Astrophysical Journal Supplement Series* 235, 42, p. 42. DOI: 10.3847/1538-4365/aa9e8a. arXiv: 1707.09322 [astro-ph.GA].

Agnello, A. et al. (Apr. 2015a). "Data mining for gravitationally lensed quasars". In: *MNRAS* 448, pp. 1446–1462. DOI: 10.1093/mnras/stv037. arXiv: 1410.4565.

Agnello, A. et al. (Dec. 2015b). "Discovery of two gravitationally lensed quasars in the Dark Energy Survey". In: *MNRAS* 454.2, pp. 1260–1265. DOI: 10.1093/mnras/stv2171. arXiv: 1508.01203 [astro-ph.GA].

Agnello, Adriano (Oct. 2017). "Quasar lenses and galactic streams: outlier selection and Gaia multiplet detection". In: *MNRAS* 471.2, pp. 2013–2021. DOI: 10.1093/mnras/stx1650. arXiv: 1705.08900 [astro-ph.GA].

Aihara, H. et al. (Jan. 2018). "The Hyper Suprime-Cam SSP Survey: Overview and survey design". In: *PASJ* 70, S4, S4. DOI: 10.1093/pasj/psx066. arXiv: 1704.05858 [astro-ph.IM].

Alard, C. (June 2000). "Image subtraction using a space-varying kernel". In: *A&AS* 144, pp. 363–370. DOI: 10.1051/aas:2000214.

Alard, C. and R. H. Lupton (Aug. 1998). "A Method for Optimal Image Subtraction". In: *ApJ* 503, pp. 325–331. DOI: 10.1086/305984. eprint: astro-ph/9712287.

Anguita, T. et al. (Nov. 2009). "COSMOS 5921+0638: characterization and analysis of a new strong gravitationally lensed AGN". In: *A&A* 507.1, pp. 35–46. DOI: 10.1051/0004-6361/200912091. arXiv: 0907.4145 [astro-ph.CO].

Bahcall, J. N. et al. (Mar. 1992). "The Snapshot Survey: A Search for Gravitationally Lensed Quasars with the Hubble Space Telescope". In: *ApJ* 387, p. 56. DOI: 10.1086/171060.

Bate, N. F. et al. (Apr. 2011). "A Microlensing Measurement of Dark Matter Fractions in Three Lensing Galaxies". In: *ApJ* 731.1, 71, p. 71. DOI: 10.1088/0004-637X/731/1/71. arXiv: 1103.0353 [astro-ph.CO].

Bennert, Vardha Nicola et al. (Jan. 2010). "Cosmic Evolution of Black Holes and Spheroids. IV. The M_{BH}-L_{sph} Relation". In: *ApJ* 708.2, pp. 1507–1527. DOI: 10.1088/0004-637X/708/2/1507. arXiv: 0911.4107 [astro-ph.CO].

Bennett, C. L. et al. (Oct. 2013). "Nine-year Wilkinson Microwave Anisotropy Probe (WMAP) Observations: Final Maps and Results". In: *ApJS* 208.2, 20, p. 20. DOI: 10.1088/0067-0049/208/2/20. arXiv: 1212.5225 [astro-ph.CO].

Blackburne, Jeffrey A. et al. (Mar. 2011). "Sizes and Temperature Profiles of Quasar Accretion Disks from Chromatic Microlensing". In: *ApJ* 729.1, 34, p. 34. DOI: 10.1088/0004-637X/729/1/34. arXiv: 1007.1665 [astro-ph.CO].

Blanton, Michael R. and John Moustakas (Sept. 2009). "Physical Properties and Environments of Nearby Galaxies". In: *ARA&A* 47.1, pp. 159–210. DOI: 10.1146/annurev-astro-082708-101734. arXiv: 0908.3017 [astro-ph.GA].

Bonvin, V. et al. (Mar. 2017). "H0LiCOW - V. New COSMOGRAIL time delays of HE 0435-1223: H_0 to 3.8 per cent precision from strong lensing in a flat ΛCDM model". In: *MNRAS* 465.4, pp. 4914–4930. DOI: 10.1093/mnras/stw3006. arXiv: 1607.01790 [astro-ph.CO].

Bosch, J. et al. (Jan. 2018). "The Hyper Suprime-Cam software pipeline". In: *PASJ* 70, S5, S5. DOI: 10.1093/pasj/psx080. arXiv: 1705.06766 [astro-ph.IM].

Brewer, Brendon J. and Geraint F. Lewis (Feb. 2006). "Strong Gravitational Lens Inversion: A Bayesian Approach". In: *ApJ* 637.2, pp. 608–619. DOI: 10.1086/498409. arXiv: astro-ph/0509863 [astro-ph].

Browne, I. W. A. et al. (May 2003). "The Cosmic Lens All-Sky Survey - II. Gravitational lens candidate selection and follow-up". In: *MNRAS* 341, pp. 13–32. DOI: 10.1046/j.1365-8711.2003.06257.x. eprint: astro-ph/0211069.

Burke, W. L. (Feb. 1981). "Multiple Gravitational Imaging by Distributed Masses". In: *ApJ* 244, p. L1. DOI: 10.1086/183466.

Burud, I. et al. (Jan. 2002a). "An optical time-delay for the lensed BAL quasar HE 2149-2745". In: *A&A* 383, pp. 71–81. DOI: 10.1051/0004-6361:20011731. arXiv: astro-ph/0112225 [astro-ph].

Burud, I. et al. (Aug. 2002b). "Time delay and lens redshift for the doubly imaged BAL quasar SBS 1520+530". In: *A&A* 391, pp. 481–486. DOI: 10.1051/0004-6361:20020856. arXiv: astro-ph/0206084 [astro-ph].

Canameras, R. et al. (Apr. 2020). "HOLISMOKES – II. Identifying galaxy-scale strong gravitational lenses in Pan-STARRS using convolutional neural networks". In: *arXiv e-prints*, arXiv:2004.13048, arXiv:2004.13048. arXiv: 2004.13048 [astro-ph.GA].

Capak, P. et al. (Sept. 2007). "The First Release COSMOS Optical and Near-IR Data and Catalog". In: *ApJS* 172.1, pp. 99–116. DOI: 10.1086/519081. arXiv: 0704.2430 [astro-ph].

Chambers, K. C. et al. (Dec. 2016). "The Pan-STARRS1 Surveys". In: *arXiv e-prints*. arXiv: 1612.05560 [astro-ph.IM].

Chan, J. H. H. et al. (July 2015). "Chitah: Strong-gravitational-lens Hunter in Imaging Surveys". In: *ApJ* 807, 138, p. 138. DOI: 10.1088/0004-637X/807/2/138. arXiv: 1411.5398.

Chan, James H. H. et al. (Apr. 2020). "Survey of Gravitationally lensed Objects in HSC Imaging (SuGOHI). IV. Lensed quasar search in the HSC survey". In: *A&A* 636, A87, A87. DOI: 10.1051/0004-6361/201937030. arXiv: 1911.02587 [astro-ph.GA].

Chao, Dani C. -Y. et al. (Aug. 2020). "Lensed quasar search via time variability with the HSC transient survey". In: *A&A* 640, A88, A88. DOI: 10.1051/0004-6361/201936806. arXiv: 1910.01140 [astro-ph.GA].

Chen, Geoff C. -F. et al. (Dec. 2019). "A SHARP view of H0LiCOW: H_0 from three time-delay gravitational lens systems with adaptive optics imaging". In: *MNRAS* 490.2, pp. 1743–1773. DOI: 10.1093/mnras/stz2547. arXiv: 1907.02533 [astro-ph.CO].

Cheng, Ting-Yun et al. (Apr. 2020). "Identifying strong lenses with unsupervised machine learning using convolutional autoencoder". In: *MNRAS* 494.3, pp. 3750–3765. DOI: 10.1093/mnras/staa1015. arXiv: 1911.04320 [astro-ph.IM].

Courbin, Frederic et al. (2002). "Quasar Lensing". In: *Gravitational Lensing: An Astrophysical Tool*. Ed. by F. Courbin and D. Minniti. Vol. 608, p. 1.

Dai, Xinyu and Christopher S. Kochanek (June 2005). "Chandra Observations of the Gravitational Lenses B1600+434 and B1608+656". In: *ApJ* 625.2, pp. 633–642. DOI: 10.1086/429485. arXiv: astro-ph/0502007 [astro-ph].

Dalal, N. and C. S. Kochanek (June 2002). "Direct Detection of Cold Dark Matter Substructure". In: *ApJ* 572, pp. 25–33. DOI: 10.1086/340303. eprint: astro-ph/0111456.

Dawson, Kyle S. et al. (Jan. 2013). "The Baryon Oscillation Spectroscopic Survey of SDSS-III". In: *AJ* 145.1, 10, p. 10. DOI: 10.1088/0004-6256/145/1/10. arXiv: 1208.0022 [astro-ph.CO].

Ding, X. et al. (Nov. 2017). "H0LiCOW VII: cosmic evolution of the correlation between black hole mass and host galaxy luminosity". In: *MNRAS* 472, pp. 90–103. DOI: 10.1093/mnras/stx1972. arXiv: 1703.02041.

Dobler, Gregory et al. (May 2007). "Microlensing of central images in strong gravitational lens systems". In: *MNRAS* 377.3, pp. 977–986. DOI: 10.1111/j.1365-2966.2007.11695.x. arXiv: astro-ph/0507522 [astro-ph].

Dye, S. and S. J. Warren (Apr. 2005). "Decomposition of the Visible and Dark Matter in the Einstein Ring 0047-2808 by Semilinear Inversion". In: *ApJ* 623.1, pp. 31–41. DOI: 10.1086/428340. arXiv: astro-ph/0411452 [astro-ph].

Eigenbrod, A. et al. (June 2005). "COSMOGRAIL: The COSmological MOnitoring of GRAvItational Lenses. I. How to sample the light curves of gravitationally lensed quasars to measure accurate time delays". In: *A&A* 436.1, pp. 25–35. DOI: 10.1051/0004-6361:20042422. arXiv: astro-ph/0503019 [astro-ph].

Fan, X. et al. (Jan. 2019). “The Discovery of a Gravitationally Lensed Quasar at z = 6.51”. In: *ApJ* 870, L11, p. L11. DOI: 10.3847/2041-8213/aaeffe. arXiv: 1810.11924.

Fassnacht, C. D. et al. (May 2006a). “Mass along the Line of Sight to the Gravitational Lens B1608+656: Galaxy Groups and Implications for H_0”. In: *ApJ* 642.1, pp. 30–38. DOI: 10.1086/500927. arXiv: astro-ph/0510728 [astro-ph].

Fassnacht, C. D. et al. (Nov. 2006b). “Three Gravitational Lenses for the Price of One: Enhanced Strong Lensing through Galaxy Clustering”. In: *ApJ* 651.2, pp. 667–675. DOI: 10.1086/507623. arXiv: astro-ph/0603445 [astro-ph].

Furusawa, Hisanori et al. (Jan. 2018). “The on-site quality-assurance system for Hyper Suprime-Cam: OSQAH”. In: *PASJ* 70, S3, S3. DOI: 10.1093/pasj/psx079.

Gaia Collaboration et al. (Nov. 2016). “The Gaia mission”. In: *A&A* 595, A1, A1. DOI: 10.1051/0004-6361/201629272. arXiv: 1609.04153 [astro-ph.IM].

Gilman, Daniel et al. (Jan. 2019). “Probing dark matter structure down to $10\hat{7}$ solar masses: flux ratio statistics in gravitational lenses with line of sight halos”. In: *arXiv e-prints*, arXiv:1901.11031, arXiv:1901.11031. arXiv: 1901.11031 [astro-ph.CO].

Gravitational Lensing: Strong, Weak and Micro (Jan. 2006). arXiv: astro-ph/0407232 [astro-ph].

Haarsma, D. B. et al. (Jan. 1999). “The Radio Wavelength Time Delay of Gravitational Lens 0957+561”. In: *ApJ* 510.1, pp. 64–70. DOI: 10.1086/306584. arXiv: astro-ph/9807115 [astro-ph].

Hartley, P. et al. (May 2019). “Strong lensing reveals jets in a sub-microJy radio-quiet quasar”. In: *MNRAS* 485.3, pp. 3009–3023. DOI: 10.1093/mnras/stz510. arXiv: 1901.05791 [astro-ph.GA].

Hewitt, J. N. et al. (Sept. 1992). “A Gravitational Lens Candidate With an Unusually Red Optical Counterpart”. In: *AJ* 104, p. 968. DOI: 10.1086/116290.

Hjorth, Jens et al. (June 2002). “The Time Delay of the Quadruple Quasar RX J0911.4+0551”. In: *ApJ* 572.1, pp. L11–L14. DOI: 10.1086/341603. arXiv: astro-ph/0205124 [astro-ph].

Huang, X. et al. (2020). “Discovering New Strong Gravitational Lenses in the DESI Legacy Imaging Surveys”. In: eprint: Arxiv:2005.04730v1. URL: http://arxiv.org/abs/2005.04730.

Huchra, J. et al. (May 1985). “2237+0305 : a new and unusual gravitational lens.” In: *AJ* 90, pp. 691–696. DOI: 10.1086/113777.

Inada, N. et al. (Feb. 2008). “The Sloan Digital Sky Survey Quasar Lens Search. II. Statistical Lens Sample from the Third Data Release”. In: *AJ* 135, pp. 496–511. DOI: 10.1088/0004-6256/135/2/496. arXiv: 0708.0828.

Inada, N. et al. (Aug. 2010). "The Sloan Digital Sky Survey Quasar Lens Search. IV. Statistical Lens Sample from the Fifth Data Release". In: *AJ* 140, pp. 403–415. DOI: 10.1088/0004-6256/140/2/403. arXiv: 1005.5570 [astro-ph.CO].

Inada, N. et al. (May 2012). "The Sloan Digital Sky Survey Quasar Lens Search. V. Final Catalog from the Seventh Data Release". In: *AJ* 143, 119, p. 119. DOI: 10.1088/0004-6256/143/5/119. arXiv: 1203.1087.

Inada, Naohisa et al. (Aug. 2003). "SDSS J092455.87+021924.9: An Interesting Gravitationally Lensed Quasar from the Sloan Digital Sky Survey". In: *AJ* 126.2, pp. 666–674. DOI: 10.1086/375906. arXiv: astro-ph/0304377 [astro-ph].

Irwin, M. J. et al. (Dec. 1989). "Photometric Variations in the Q2237+0305 System: First Detection of a Microlensing Event". In: *AJ* 98, p. 1989. DOI: 10.1086/115272.

Ivezić, Željko et al. (Mar. 2019). "LSST: From Science Drivers to Reference Design and Anticipated Data Products". In: *ApJ* 873.2, 111, p. 111. DOI: 10.3847/1538-4357/ab042c. arXiv: 0805.2366 [astro-ph].

Jacobs, C. et al. (Oct. 2017). "Finding strong lenses in CFHTLS using convolutional neural networks". In: *MNRAS* 471.1, pp. 167–181. DOI: 10.1093/mnras/stx1492. arXiv: 1704.02744 [astro-ph.IM].

Jacobs, C. et al. (July 2019). "An Extended Catalog of Galaxy-Galaxy Strong Gravitational Lenses Discovered in DES Using Convolutional Neural Networks". In: *ApJS* 243.1, 17, p. 17. DOI: 10.3847/1538-4365/ab26b6. arXiv: 1905.10522 [astro-ph.GA].

Jaelani, Anton T. et al. (Apr. 2020). "Survey of Gravitationally-lensed Objects in HSC Imaging (SuGOHI). V. Group-to-cluster scale lens search from the HSC-SSP Survey". In: *MNRAS*. DOI: 10.1093/mnras/staa1062. arXiv: 2002.01611 [astro-ph.GA].

Jiménez-Vicente, J. et al. (Feb. 2015). "Dark Matter Mass Fraction in Lens Galaxies: New Estimates from Microlensing". In: *ApJ* 799.2, 149, p. 149. DOI: 10.1088/0004-637X/799/2/149. arXiv: 1407.3955 [astro-ph.GA].

Kawanomoto, Satoshi et al. (Aug. 2018). "Hyper Suprime-Cam: Filters". In: *PASJ* 70.4, 66, p. 66. DOI: 10.1093/pasj/psy056.

Keeton, C. R. et al. (June 1997). "Shear and Ellipticity in Gravitational Lenses". In: *ApJ* 482.2, pp. 604–620. DOI: 10.1086/304172. arXiv: astro-ph/9610163 [astro-ph].

Keeton, C. R. et al. (Oct. 2000). "The Host Galaxy of the Lensed Quasar Q0957+561". In: *ApJ* 542.1, pp. 74–93. DOI: 10.1086/309517. arXiv: astro-ph/0001500 [astro-ph].

Kelly, B. C. et al. (June 2009). "Are the Variations in Quasar Optical Flux Driven by Thermal Fluctuations?" In: *ApJ* 698, pp. 895–910. DOI: 10.1088/0004-637X/698/1/895. arXiv: 0903.5315 [astro-ph.CO].

Kelly, B. C. et al. (June 2014). "Flexible and Scalable Methods for Quantifying Stochastic Variability in the Era of Massive Time-domain Astronomical Data Sets". In: *ApJ* 788, 33, p. 33. DOI: 10.1088/0004-637X/788/1/33. arXiv: 1402.5978 [astro-ph.IM].

Kochanek, C. S. (Apr. 2004). "Quantitative Interpretation of Quasar Microlensing Light Curves". In: *ApJ* 605.1, pp. 58–77. DOI: 10.1086/382180. arXiv: astro-ph/0307422 [astro-ph].

Kochanek, C. S. et al. (Feb. 2006a). "A Simple Method to Find All Lensed Quasars". In: *ApJ* 637, pp. L73–L76. DOI: 10.1086/500559. eprint: astro-ph/0512031.

Kochanek, C. S. et al. (Mar. 2006b). "The Time Delays of Gravitational Lens HE 0435-1223: An Early-Type Galaxy with a Rising Rotation Curve". In: *ApJ* 640.1, pp. 47–61. DOI: 10.1086/499766. arXiv: astro-ph/0508070 [astro-ph].

Kochanek, Christopher S. (June 1991). "The Implications of Lenses for Galaxy Structure". In: *ApJ* 373, p. 354. DOI: 10.1086/170057.

Komiyama, Yutaka et al. (Jan. 2018). "Hyper Suprime-Cam: Camera dewar design". In: *PASJ* 70, S2, S2. DOI: 10.1093/pasj/psx069.

Koopmans, L. V. E. et al. (Dec. 2003). "The Hubble Constant from the Gravitational Lens B1608+656". In: *ApJ* 599.1, pp. 70–85. DOI: 10.1086/379226. arXiv: astro-ph/0306216 [astro-ph].

Kormann, R. et al. (Apr. 1994). "Isothermal elliptical gravitational lens models". In: *A&A* 284, pp. 285–299.

Kundić, Tomislav et al. (June 1997). "A Robust Determination of the Time Delay in 0957+561A, B and a Measurement of the Global Value of Hubble's Constant". In: *ApJ* 482.1, pp. 75–82. DOI: 10.1086/304147. arXiv: astro-ph/9610162 [astro-ph].

Lacki, Brian C. et al. (June 2009). "Difference Imaging of Lensed Quasar Candidates in the Sloan Digital Sky Survey Supernova Survey Region". In: *ApJ* 698.1, pp. 428–438. DOI: 10.1088/0004-637X/698/1/428. arXiv: 0801.3432 [astro-ph].

Langston, G. I. et al. (May 1989). "MG 1654+1346: an Einstein Ring Image of a Quasar Radio Lobe". In: *AJ* 97, p. 1283. DOI: 10.1086/115071.

Lanusse, François et al. (Jan. 2018). "CMU DeepLens: deep learning for automatic image-based galaxy-galaxy strong lens finding". In: *MNRAS* 473.3, pp. 3895–3906. DOI: 10.1093/mnras/stx1665. arXiv: 1703.02642 [astro-ph.IM].

Lehár, J. et al. (June 2000). "Hubble Space Telescope Observations of 10 Two-Image Gravitational Lenses". In: *ApJ* 536.2, pp. 584–605. DOI: 10.1086/308963. arXiv: astro-ph/9909072 [astro-ph].

Lemon, C. A. et al. (Dec. 2017). "Gravitationally lensed quasars in Gaia: I. Resolving small-separation lenses". In: *MNRAS* 472, pp. 5023–5032. DOI: 10.1093/mnras/stx2094. arXiv: 1709.08976.

Lemon, C. A. et al. (Oct. 2018). "Gravitationally lensed quasars in Gaia - II. Discovery of 24 lensed quasars". In: *MNRAS* 479, pp. 5060–5074. DOI: 10.1093/mnras/sty911. arXiv: 1803.07601.

Lidman, C. et al. (Apr. 1999). "The Redshift of the Gravitationally Lensed Radio Source PKS 1830-211". In: *ApJ* 514.2, pp. L57–L60. DOI: 10.1086/311949. arXiv: astro-ph/9902317 [astro-ph].

Lidman, C. et al. (Dec. 2000). "Exploring the gravitationally lensed system HE 1104-1805: VLT spectroscopy of the lens at z=0.729". In: *A&A* 364, pp. L62–L65. arXiv: astro-ph/0010403 [astro-ph].

Lilly, Simon J. et al. (Oct. 2009). "The zCOSMOS 10k-Bright Spectroscopic Sample". In: *ApJS* 184.2, pp. 218–229. DOI: 10.1088/0067-0049/184/2/218.

Magain, P. et al. (July 1988). "Discovery of a quadruply lensed quasar: the 'clover leaf H1413 + 117". In: *Nature* 334.6180, pp. 325–327. DOI: 10.1038/334325a0.

Magain, P. et al. (Feb. 1998). "Deconvolution with Correct Sampling". In: *ApJ* 494.1, pp. 472–477. DOI: 10.1086/305187. arXiv: astro-ph/9704059 [astro-ph].

Mao, S. and P. Schneider (Apr. 1998). "Evidence for substructure in lens galaxies?" In: *MNRAS* 295, p. 587. DOI: 10.1046/j.1365-8711.1998.01319.x. eprint: astro-ph/9707187.

Maoz, D. et al. (July 1992). "Gravitational Lensing of Quasars as Seen by the Hubble Space Telescope Snapshot Survey". In: *ApJ* 394, p. 51. DOI: 10.1086/171558.

– (Jan. 1993a). "The Hubble Space Telescope Snapshot Survey. III. Further Observations in Search of Gravitationally Lensed Quasars". In: *ApJ* 402, p. 69. DOI: 10.1086/172113.

Maoz, D. et al. (May 1993b). "The Hubble Space Telescope Snapshot Survey. IV. A Summary of the Search for Gravitationally Lensed Quasars". In: *ApJ* 409, p. 28. DOI: 10.1086/172639.

Marshall, P. J. et al. (Jan. 2016). "SPACE WARPS - I. Crowdsourcing the discovery of gravitational lenses". In: *MNRAS* 455, pp. 1171–1190. DOI: 10.1093/mnras/stv2009. arXiv: 1504.06148 [astro-ph.IM].

McGreer, Ian D. et al. (May 2013). "The z = 5 Quasar Luminosity Function from SDSS Stripe 82". In: *ApJ* 768.2, 105, p. 105. DOI: 10.1088/0004-637X/768/2/105. arXiv: 1212.4493 [astro-ph.CO].

McMahon, R. G. et al. (Dec. 2013). "First Scientific Results from the VISTA Hemisphere Survey (VHS)". In: *The Messenger* 154, pp. 35–37.

Metcalf, R. B. and P. Madau (Dec. 2001). "Compound Gravitational Lensing as a Probe of Dark Matter Substructure within Galaxy Halos". In: *ApJ* 563, pp. 9–20. DOI: 10.1086/323695. eprint: astro-ph/0108224.

Mineshige, Shin and Atsunori Yonehara (Aug. 1999). "Gravitational Microlens Mapping of a Quasar Accretion Disk". In: *PASJ* 51, pp. 497–504. DOI: 10.1093/pasj/51.4.497.

Miyazaki, Satoshi et al. (Jan. 2018). "Hyper Suprime-Cam: System design and verification of image quality". In: *PASJ* 70, S1, S1. DOI: 10.1093/pasj/psx063.

More, A. et al. (Jan. 2016a). "SPACE WARPS- II. New gravitational lens candidates from the CFHTLS discovered through citizen science". In: *MNRAS* 455, pp. 1191–1210. DOI: 10.1093/mnras/stv1965. arXiv: 1504.05587.

More, Anupreeta et al. (Feb. 2016b). "The SDSS-III BOSS quasar lens survey: discovery of 13 gravitationally lensed quasars". In: *MNRAS* 456.2, pp. 1595–1606. DOI: 10.1093/mnras/stv2813. arXiv: 1509.07917 [astro-ph.GA].

Morgan, Christopher W. et al. (Aug. 2006). "Microlensing of the Lensed Quasar SDSS 0924+0219". In: *ApJ* 647.2, pp. 874–885. DOI: 10.1086/505569. arXiv: astro-ph/0601523 [astro-ph].

Morgan, Christopher W. et al. (Dec. 2018). "Accretion Disk Size Measurement and Time Delays in the Lensed Quasar WFI 2033-4723". In: *ApJ* 869.2, 106, p. 106. DOI: 10.3847/1538-4357/aaed3e. arXiv: 1812.05639 [astro-ph.GA].

Morgan, Nicholas D. et al. (Oct. 1999). "CTQ 414: A New Gravitational Lens". In: *AJ* 118.4, pp. 1444–1449. DOI: 10.1086/301056. arXiv: astro-ph/9906173 [astro-ph].

Myers, S. T. et al. (May 2003). "The Cosmic Lens All-Sky Survey - I. Source selection and observations". In: *MNRAS* 341, pp. 1–12. DOI: 10.1046/j.1365-8711.2003.06256.x. eprint: astro-ph/0211073.

Nierenberg, A. M. et al. (Aug. 2014). "Detection of substructure with adaptive optics integral field spectroscopy of the gravitational lens B1422+231". In: *MNRAS* 442, pp. 2434–2445. DOI: 10.1093/mnras/stu862. arXiv: 1402.1496.

Oguri, M. (Aug. 2010). "The Mass Distribution of SDSS J1004+4112 Revisited". In: *PASJ* 62, pp. 1017–1024. DOI: 10.1093/pasj/62.4.1017. arXiv: 1005.3103.

Oguri, M. and P. J. Marshall (July 2010). "Gravitationally lensed quasars and supernovae in future wide-field optical imaging surveys". In: *MNRAS* 405, pp. 2579–2593. DOI: 10.1111/j.1365-2966.2010.16639.x. arXiv: 1001.2037.

Oguri, M. et al. (Sept. 2006). "The Sloan Digital Sky Survey Quasar Lens Search. I. Candidate Selection Algorithm". In: *AJ* 132, pp. 999–1013. DOI: 10.1086/506019. eprint: astro-ph/0605571.

Oguri, M. et al. (May 2012). "The Sloan Digital Sky Survey Quasar Lens Search. VI. Constraints on Dark Energy and the Evolution of Massive Galaxies". In: *AJ* 143, 120, p. 120. DOI: 10.1088/0004-6256/143/5/120. arXiv: 1203.1088.

Oguri, Masamune (May 2007). "Gravitational Lens Time Delays: A Statistical Assessment of Lens Model Dependences and Implications for the Global Hubble Constant". In: *ApJ* 660.1, pp. 1–15. DOI: 10.1086/513093. arXiv: astro-ph/0609694 [astro-ph].

Oscoz, Alejandro et al. (Apr. 1997). "Time Delay of QSO 0957+561 and Cosmological Implications". In: *ApJ* 479.2, pp. L89–L92. DOI: 10.1086/310599.

Ostrovski, F. et al. (Mar. 2017). "VDES J2325-5229 a z = 2.7 gravitationally lensed quasar discovered using morphology-independent supervised machine learning". In: *MNRAS* 465, pp. 4325–4334. DOI: 10.1093/mnras/stw2958. arXiv: 1607.01391.

Ostrovski, F. et al. (Jan. 2018). "The discovery of a five-image lensed quasar at z = 3.34 using PanSTARRS1 and Gaia". In: *MNRAS* 473, pp. L116–L120. DOI: 10.1093/mnrasl/slx173. arXiv: 1709.08975.

Park, Daeseong et al. (Feb. 2015). "Cosmic Evolution of Black Holes and Spheroids. V. The Relation between Black Hole Mass and Host Galaxy Luminosity for a Sample of 79 Active Galaxies". In: *ApJ* 799.2, 164, p. 164. DOI: 10.1088/0004-637X/799/2/164. arXiv: 1411.6334 [astro-ph.GA].

Peng, C. Y. et al. (Oct. 2006a). "Probing the Coevolution of Supermassive Black Holes and Galaxies Using Gravitationally Lensed Quasar Hosts". In: *ApJ* 649, pp. 616–634. DOI: 10.1086/506266. eprint: astro-ph/0603248.

Peng, Chien Y. et al. (Oct. 2006b). "Probing the Coevolution of Supermassive Black Holes and Galaxies Using Gravitationally Lensed Quasar Hosts". In: *ApJ* 649.2, pp. 616–634. DOI: 10.1086/506266. arXiv: astro-ph/0603248 [astro-ph].

Planck Collaboration et al. (July 2018). "Planck 2018 results. VI. Cosmological parameters". In: *arXiv e-prints*, arXiv:1807.06209, arXiv:1807.06209. arXiv: 1807.06209 [astro-ph.CO].

Refsdal, S. (Jan. 1964). "On the possibility of determining Hubble's parameter and the masses of galaxies from the gravitational lens effect". In: *MNRAS* 128, p. 307. DOI: 10.1093/mnras/128.4.307.

Roberts, David H. et al. (July 1991). "The Hubble constant from VLA measurement of the time delay in the double quasar 0957+561". In: *Nature* 352.6330, pp. 43–45. DOI: 10.1038/352043a0.

Rusu, C. E. et al. (Mar. 2018). "A Search for Gravitationally Lensed Quasars and Quasar Pairs in Pan-STARRS1: Spectroscopy and Sources of Shear in the Diamond 2M1134−2103". In: *arXiv e-prints*. arXiv: 1803.07175.

Sakai, Shoko et al. (June 2004). "The Effect of Metallicity on Cepheid-based Distances". In: *ApJ* 608.1, pp. 42–61. DOI: 10.1086/386540. arXiv: astro-ph/0402499 [astro-ph].

Sánchez, E. and Des Collaboration (Nov. 2010). "The Dark Energy Survey". In: *Journal of Physics Conference Series*. Vol. 259. Journal of Physics Conference Series, p. 012080. DOI: 10.1088/1742-6596/259/1/012080.

Sandage, A. et al. (Sept. 2004). "New period-luminosity and period-color relations of classical Cepheids. II. Cepheids in LMC". In: *A&A* 424, pp. 43–71. DOI: 10.1051/0004-6361:20040222. arXiv: astro-ph/0402424 [astro-ph].

Sanitt, N. (Nov. 1971). "Quasi-stellar Objects and Gravitational Lenses". In: *Nature* 234.5326, pp. 199–203. DOI: 10.1038/234199a0.

Schild, Rudolph E. (Dec. 1990). "The Time Delay in the Twin QSO Q0957+561". In: *AJ* 100, p. 1771. DOI: 10.1086/115634.

Schmidt, M. (Mar. 1963). "3C 273 : A Star-Like Object with Large Red-Shift". In: *Nature* 197.4872, p. 1040. DOI: 10.1038/1971040a0.

Schneider, P. (Feb. 1985). "A new formulation of gravitational lens theory, time-delay, and Fermat's principle". In: *A&A* 143.2, pp. 413–420.

Shajib, A. J. et al. (Mar. 2020). "STRIDES: A 3.9 per cent measurement of the Hubble constant from the strong lens system DES J0408-5354". In: *MNRAS*. DOI: 10.1093/mnras/staa828. arXiv: 1910.06306 [astro-ph.CO].

Sluse, D. et al. (July 2003). "A quadruply imaged quasar with an optical Einstein ring candidate: 1RXS J113155.4-123155". In: *A&A* 406, pp. L43–L46. DOI: 10.1051/0004-6361:20030904. arXiv: astro-ph/0307345 [astro-ph].

Sonnenfeld, Alessandro et al. (Jan. 2018). "Survey of Gravitationally-lensed Objects in HSC Imaging (SuGOHI). I. Automatic search for galaxy-scale strong lenses". In: *PASJ* 70, S29, S29. DOI: 10.1093/pasj/psx062. arXiv: 1704.01585 [astro-ph.GA].

Sonnenfeld, Alessandro et al. (Apr. 2020). "Survey of Gravitationally-lensed Objects in HSC Imaging (SuGOHI). VI. Crowdsourced lens finding with Space Warps". In: *arXiv e-prints*, arXiv:2004.00634, arXiv:2004.00634. arXiv: 2004.00634 [astro-ph.IM].

Spiniello, C. et al. (Oct. 2018). "KiDS-SQuaD: The KiDS Strongly lensed Quasar Detection project". In: *MNRAS* 480, pp. 1163–1173. DOI: 10.1093/mnras/sty1923. arXiv: 1805.12436.

Stacey, H. R. et al. (June 2018). "Gravitational lensing reveals extreme dust-obscured star formation in quasar host galaxies". In: *MNRAS* 476.4, pp. 5075–5114. DOI: 10.1093/mnras/sty458. arXiv: 1705.10530 [astro-ph.GA].

Stockton, A. (Dec. 1980). "The lens galaxy of the twin QSO 0957+561". In: *ApJ* 242, pp. L141–L144. DOI: 10.1086/183419.

Subasavage, John P. et al. (July 2010). "SMARTS revealed". In: *Proc. SPIE*. Vol. 7737. Society of Photo-Optical Instrumentation Engineers (SPIE) Conference Series, p. 77371C. DOI: 10.1117/12.859145.

Subrahmanyan, R. et al. (Sept. 1990). "1830-211 / gravitationally lensed images of a flat-spectrum radio core ?" In: *MNRAS* 246, p. 263.

Surdej, J. et al. (Oct. 1987). "A new case of gravitational lensing". In: *Nature* 329.6141, pp. 695–696. DOI: 10.1038/329695a0.

Suyu, S. H. et al. (Sept. 2006). "A Bayesian analysis of regularized source inversions in gravitational lensing". In: *MNRAS* 371.2, pp. 983–998. DOI: 10.1111/j.1365-2966.2006.10733.x. arXiv: astro-ph/0601493 [astro-ph].

Suyu, S. H. et al. (Jan. 2009). "Dissecting the Gravitational Lens B1608+656. I. Lens Potential Reconstruction". In: *ApJ* 691.1, pp. 277–298. DOI: 10.1088/0004-637X/691/1/277. arXiv: 0804.2827 [astro-ph].

Suyu, S. H. et al. (Mar. 2010). "Dissecting the Gravitational lens B1608+656. II. Precision Measurements of the Hubble Constant, Spatial Curvature, and the Dark Energy Equation of State". In: *ApJ* 711.1, pp. 201–221. DOI: 10.1088/0004-637X/711/1/201. arXiv: 0910.2773 [astro-ph.CO].

Suyu, S. H. et al. (Apr. 2013). "Two Accurate Time-delay Distances from Strong Lensing: Implications for Cosmology". In: *ApJ* 766.2, 70, p. 70. DOI: 10.1088/0004-637X/766/2/70. arXiv: 1208.6010 [astro-ph.CO].

Tammann, G. A. et al. (June 2003). "New Period-Luminosity and Period-Color relations of classical Cepheids: I. Cepheids in the Galaxy". In: *A&A* 404, pp. 423–448. DOI: 10.1051/0004-6361:20030354. arXiv: astro-ph/0303378 [astro-ph].

Tie, S. S. and C. S. Kochanek (Jan. 2018a). "Microlensing makes lensed quasar time delays significantly time variable". In: *MNRAS* 473.1, pp. 80–90. DOI: 10.1093/mnras/stx2348. arXiv: 1707.01908 [astro-ph.GA].

– (Jan. 2018b). "Quasar microlensing models with constraints on the Quasar light curves". In: *MNRAS* 473.1, pp. 616–620. DOI: 10.1093/mnras/stx2380. arXiv: 1707.02982 [astro-ph.IM].

Vanderriest, C. et al. (May 1989). "The value of the time delay delta T (A,B) for the 'double' quasar 0957+561 from optical photometric monitoring." In: *A&A* 215, pp. 1–13.

Walsh, D. et al. (May 1979). "0957+561 A, B: twin quasistellar objects or gravitational lens?" In: *Nature* 279, pp. 381–384. DOI: 10.1038/279381a0.

Wambsganss, J. et al. (Aug. 1990). "Interpretation of the Microlensing Event in QSO 2237+0305". In: *ApJ* 358, p. L33. DOI: 10.1086/185773.

Weymann, Ray J. et al. (June 1980). "The triple QSO PG1115 + 08: another probable gravitational lens". In: *Nature* 285.5767, pp. 641–643. DOI: 10.1038/285641a0.

Witt, Hans J. and Shude Mao (Oct. 1997). "Probing the structure of lensing galaxies with quadruple lenses: the effect of 'external' shear". In: *MNRAS* 291.1, pp. 211–218. DOI: 10.1093/mnras/291.1.211. arXiv: astro-ph/9702021 [astro-ph].

Wong, Kenneth C. et al. (July 2019). "H0LiCOW XIII. A 2.4% measurement of H_0 from lensed quasars: 5.3σ tension between early and late-Universe probes". In: *arXiv e-prints*, arXiv:1907.04869, arXiv:1907.04869. arXiv: 1907.04869 [astro-ph.CO].

Wright, Edward L. et al. (Dec. 2010). "The Wide-field Infrared Survey Explorer (WISE): Mission Description and Initial On-orbit Performance". In: *AJ* 140.6, pp. 1868–1881. DOI: 10.1088/0004-6256/140/6/1868. arXiv: 1008.0031 [astro-ph.IM].

Wyithe, J. S. B. et al. (June 2000). "Limits on the microlens mass function of Q2237+0305". In: *MNRAS* 315.1, pp. 51–61. DOI: 10.1046/j.1365-8711.2000.03360.x. arXiv: astro-ph/9904359 [astro-ph].

Yasuda, N. et al. (Apr. 2019). "The Hyper Suprime-Cam SSP Transient Survey in COSMOS: Overview". In: *arXiv e-prints*. arXiv: 1904.09697.

Yonehara, Atsunori et al. (July 1998). "An X-Ray Microlensing Test of AU-Scale Accretion Disk Structure in Q2237+0305". In: *ApJ* 501.1, pp. L41–L44. DOI: 10.1086/311431. arXiv: astro-ph/9804251 [astro-ph].

York, D. G. et al. (Sept. 2000). "The Sloan Digital Sky Survey: Technical Summary". In: *AJ* 120, pp. 1579–1587. DOI: 10.1086/301513. eprint: astro-ph/0006396.

Young, P. et al. (Oct. 1980). "The double quasar Q0957+561 A, B: a gravitational lens image formed by a galaxy at z=0.39." In: *ApJ* 241, pp. 507–520. DOI: 10.1086/158365.